UNIVERSITY OF CALIFORNIA

Los Angeles

Designing Molecules for Quantum Technology

A dissertation submitted in partial satisfaction
of the requirements for the degree
Doctor of Philosophy in Chemistry

by

Claire Dickerson

2024

ABSTRACT OF THE DISSERTATION

Designing Molecules
for Quantum Technology

by

Claire Dickerson
Doctor of Philosophy in Chemistry
University of California, Los Angeles, 2024
Professor Anastassia N. Alexandrova, Chair

Electronic excitations, induced by lasers, that decay directly to the initial electronic ground state are called optical cycling transitions. These transitions are used in quantum information and precision measurement for state initialization and readout. One way to prepare initial quantum states is by directly laser-cooling the molecule. In this work, we theoretically predicted molecules, beyond a few atoms in size, which could be laser-cooled, opening the field to increasingly larger polyatomic molecules. The extra degrees of freedom in polyatomic molecules allow novel features for quantum information, simulation, photon entanglement and provide a testbed for studying ultracold chemistry or fundamental physics. We developed design rules, from chemical principles, to tune ultranarrow electronic transitions of large molecules, from small organic to large inorganic complexes. Along the way, various theoretical methods were used or developed, from DFT to *ab initio* multireference methods to model Hamiltonians, which predicted relevant transitions or lifetimes in these molecules to match experiment.

The dissertation of Claire Dickerson is approved.

Wesley C. Campbell

Justin R. Caram

Daniel Neuhauser

Anastassia N. Alexandrova, Committee Chair

University of California, Los Angeles

2024

To my sister, parents and grandmother

TABLE OF CONTENTS

LIST OF FIGURES

LIST OF TABLES

ACKNOWLEDGMENTS

I am deeply thankful for all the friends and research mentors from the Alexandrova and Neuhauser research groups (espsecially Prof. Alexandrova, who encouraged me to pursue whatever research directions I found interesting), within collaborations (especially the MFOCC group) and on my committee. Working with so many thoughtful, kind and humble people across research areas and institutions was a privilege. I will always be grateful for everyone I met and everything I learned during my time at UCLA.

Thank you to the friends and mentors in the LA community, who don't know quantum mechanics and don't care. Having a support system outside of graduate school provided a much-needed perspective and made LA feel like home. And despite my move to California, thank you to the Buffalo Bills for making the postseason these past few years.

Most importantly, thank you to my family who, despite the distance, has always been up for a phone call. Calls made to pass the time, inevitably while walking to Ralph's, sparked some of my favorite conversations. Thank you for reminding me to not sweat the small stuff (and it's all small stuff). I love you.

Chapter 2 is adapted with permission from:

Q. Sun, C.E. Dickerson, J. Dai, I. Pope, L. Cheng, D. Neuhauser, A.N. Alexandrova, D. Mitra and T. Zelevinsky, Probing the Limits of Optical Cycling in a Predissociative Diatomic Molecule, Phys. Rev. Res., **5**, 043070 (2023) © 2023 American Physical Society.

Chapter 3 is adapted with permission from:

C.E. Dickerson, H. Guo, A.J. Shin, B.L. Augenbraun, J.R. Caram, W.C. Campbell and A.N. Alexandrova, Franck-Condon Tuning of Optical Cycling Centers by Organic Functionalization, Phys. Rev. Lett., **126**, 123002 (2021) © 2021 American Physical Society.

G. Zhu, D. Mitra, B.L. Augenbraun, C.E. Dickerson, M.J. Frim, G. Lao, Z.D. Lasner,

A.N. Alexandrova, W.C. Campbell, J.R. Caram, J.M. Doyle and E.R. Hudson, Functionalizing Aromatic Compounds with Optical Cycling Centres, Nat. Chem., **14**, 995–999 (2022)

G. Zhu, G. Lao, C.E. Dickerson, J.R. Caram, W.C. Campbell, A.N. Alexandrova and E.R. Hudson, Extending the Large Molecule Limit: The Role of Fermi Resonance in Developing a Quantum Functional Group, J. Phys. Chem. Lett., **15** (2), 590-597 (2024) © 2024 American Chemical Society.

Chapter 4 is adapted with permission from:

C.E. Dickerson, H. Guo, G. Zhu, E.R. Hudson, J.R. Caram, W.C. Campbell and A.N. Alexandrova, Optical Cycling Functionalization of Arenes, J. Phys. Chem. Lett., **12** (16), 3989–3995 (2021) © 2024 American Chemical Society.

C.E. Dickerson, C. Chang, H. Guo and A.N. Alexandrova, Fully Saturated Hydrocarbons as Hosts of Optical Cycling Centers, J. Phys. Chem. A., **126** (51), 9644–9650 (2022) © 2024 American Chemical Society.

Chapter 5 is adapted with permission from:

H. Guo, C.E. Dickerson, A.J. Shin, C. Zhao, T.L. Atallah, J.R. Caram, W.C. Campbell and A.N. Alexandrova, Surface Chemical Trapping of Optical Cycling Centers, Phys. Chem. Chem. Phys., **23**, 211-218 (2021)

C.E. Dickerson, A.N. Alexandrova, P. Narang and J.P. Philbin, Single-Molecule Superradiance for Optical Cycling, arXiv:2310.01534 (2023)

Chapter 6 is adapted with permission from:

A.J. Shin*, C. Zhao*, Y. Shen*, C.E. Dickerson*, B.Y. Li, D. Bím, T.L. Atallah, P.H. Oyala, L.K. Alson, A.N. Alexandrova, P.L. Diaconescu, W.C. Campbell and J.R. Caram, Toward Liquid Cell Quantum Sensing: Ytterbium Complexes with Ultra-Narrow Absorption, chemrxiv-2022-vg4jr (2022)

VITA

2019-2021 M.S. in Chemistry, University of California, Los Angeles

2014-2018 B.S. in Chemistry, University of Rochester

PUBLICATIONS

G. Zhu, G. Lao, C.E. Dickerson, J.R. Caram, W.C. Campbell, A.N. Alexandrova and E.R. Hudson, J. Phys. Chem. Lett., **15** (2), 590-597 (2024)

Q. Sun, C.E. Dickerson, J. Dai, I. Pope, L. Cheng, D. Neuhauser, A.N. Alexandrova, D. Mitra and T. Zelevinsky, Phys. Rev. Res., **5**, 043070 (2023)

C.E. Dickerson, A.N. Alexandrova, P. Narang and J.P. Philbin, arXiv:2310.01534 (2023), submitted.

B.Y. Li, C.E. Dickerson, A.J. Shin, C. Zhao, Y. Shen, Y. He, P.L. Diaconescu, A.N. Alexandrova and J.R. Caram, chemrxiv-2023-v1nqv (2023), submitted.

R. Lavroff, J. Munarriz, C.E. Dickerson, F. Munoz and A.N. Alexandrova, Proc. Natl. Acad. Sci. (2023), just accepted.

C.E. Dickerson, C. Chang, H. Guo and A.N. Alexandrova, J. Phys. Chem. A., **126** (51), 9644–9650 (2022)

A.J. Shin*, C. Zhao*, Y. Shen*, C.E. Dickerson*, B.Y. Li, D. Bím, T.L. Atallah, P.H. Oyala, L.K. Alson, A.N. Alexandrova, P.L. Diaconescu, W.C. Campbell and J.R. Caram, chemrxiv-2022-vg4jr (2022), submitted.

G. Lao, G. Zhu, C.E. Dickerson, B.L. Augenbraun, A.N. Alexandrova, J.R. Caram, E.R. Hudson and Wesley C. Campbell, J. Phys. Chem. Lett., **13** (47), 11029–11035 (2022)

G. Zhu, D. Mitra, B.L. Augenbraun, C.E. Dickerson, M.J. Frim, G. Lao, Z.D. Lasner, A.N. Alexandrova, W.C. Campbell, J.R. Caram, J.M. Doyle and E.R. Hudson, Nat. Chem., **14**, 995–999 (2022)

Z. Zhang, B. Zandkarimi, J. Munarriz, C.E. Dickerson and A.N. Alexandrova, Chem. Cat. Chem., **14** (15), e202200345 (2022)

R.J. MacDonell, C.E. Dickerson, C.J.T. Birch, A. Kumar, C.L. Edmunds, M.J. Biercuk, C. Hempel and I. Kassal, Chem. Sci., **12**, 9794-9805 (2021)

C.E. Dickerson, H. Guo, G. Zhu, E.R. Hudson, J.R. Caram, W.C. Campbell and A.N. Alexandrova, J. Phys. Chem. Lett., **12** (16), 3989–3995 (2021)

C.E. Dickerson*, H. Guo*, A.J. Shin, B.L. Augenbraun, J.R. Caram, W.C. Campbell and A.N. Alexandrova, Phys. Rev. Lett., **126**, 123002 (2021)

H. Guo, C.E. Dickerson, A.J. Shin, C. Zhao, T.L. Atallah, J.R. Caram, W.C. Campbell and A.N. Alexandrova, Phys. Chem. Chem. Phys., **23**, 211-218 (2021)

D.S. Levine, M.A. Watson, L.D. Jacobson, C.E. Dickerson, H.S. Yu and A.D. Bochevarov, J. Comput. Aided Mol. Des., **35**, 417–431 (2021)

C.E. Dickerson, P.P. Bera and T.J. Lee, J. Phys. Chem. A, **122** (45), 8898–8904 (2018)

CHAPTER 1

Introduction

In this work, we theoretically predict ultracold (< 1mK) molecules which are tailor-made for utilities in fundamental physics and quantum information science. We develop specific design principles and leverage degrees of freedom unique to molecules, such as vibrations or dipolar coupling, to meet specific quantum engineering goals. Cooling molecules to the ultracold regime enables ultimate coherent quantum control of a system despite its chemical complexity. For example, one can prepare and control a single quantum state despite many degrees of freedom, an impossible task at higher temperatures. This new regime enables high-resolution spectroscopy, tests of fundamental laws of nature and precise control of chemical reactions, or new reaction coordinates, such as low-energy quantum tunneling paths that dominate at lower temperatures [1].

In AMO physics, working in the ultracold regime is not new. For decades, physicists developed complex tools to trap and cool atoms which they use today for precise atomic clocks, quantum simulation/computation and testing physics beyond the standard model [2–5]. However, cold atoms have some limitations, such as inherent noise in optical confinement, whereas molecules have predictable scalability (*e.g.* a C-C bond will always be ~ 1.54 $\mathring{A}$). Molecular complexity offers more degrees of freedom and tunable handles, such as dipole-dipole interactions, long-lived states/coherence times and rich internal structure. People have proposed ways to use this complexity to their advantage, such as developing novel quantum error correction schemes, where specific molecular rotational states are robust against noise [6]. Recently, the AMO physics community has had great success in trapping ultracold

diatomic molecules, such as SrF and CaF [7, 8], to realize these applications.

Polyatomic molecules, however, have very different internal structures than diatomics. Often, they have natural parity doublets, which can be polarized at low electric fields, giving rise to states insensitive to the magnetic field and switchable dipole interactions, a great resource for high precision measurement or long-lived quantum gates [9, 10]. Access to ultracold vibrational modes in polyatomics allows switchable dipolar or vibrational couplings for more advanced quantum simulations, such as simulating quantum magnetism [11]. Additionally, stretching and bending vibrational modes can be used as probes for ultralight dark matter [12]. In space, quantum effects dominate and low-energy physics exists as a loss channel, even for chemically nonreactive molecules. Understanding and controlling these collisions, in which molecules form extremely long-lived complexes ("sticky collisions") could answer important questions in star-forming/prebiotic regions, such as universe formation, or provide novel ways to create chemical products [13].

One method to get molecules to the ultracold regime is through direct laser cooling, which involves repeatedly scattering optical photons off of a molecular beam (Fig. 1.1) [14]. Some small, polyatomic molecules have recently been directly laser-cooled [15–17]. By red-detuning a laser, and with repeated absorption and emission of the photon, the molecules emit recoil momentum in all directions via spontaneous emission; no average momentum is gained and the molecular beam is slowed down, or "cooled". For this repeated momentum kick to slow down the molecule, since a photon's momentum is tiny compared to an atom, one needs $\sim 10,000$ photon scatters. In other words, one needs a closed, two-level system which can repeatedly cycle population without loss to other decay channels. This closed-loop is known as an optical cycling center (OCC). Once an OCC is laser-cooled, population can be coherently shuttled (maintaining quantum numbers) via a narrowband laser. One can then prepare superpositions of these systems to generate quantum gates, or develop entanglement schemes for two-qubit quantum gates. The research herein focuses on theoretically predicting and expanding the OCC framework in large molecules.

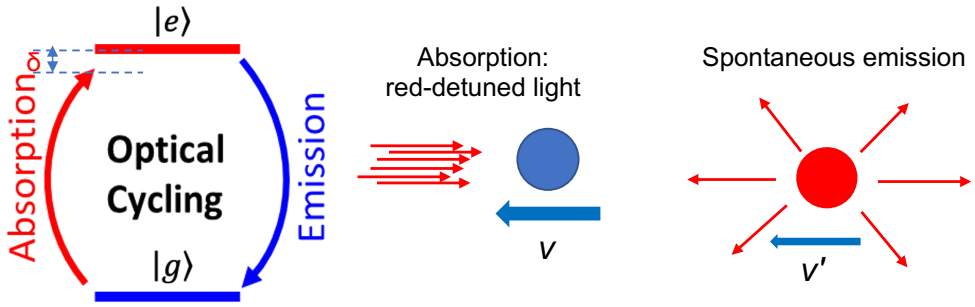

Figure 1.1: Schematic of an optical cycling center (OCC), where a molecular beam is slowed with direct laser cooling.

To quantify how "closed-loop" a system is, to be capable of optical cycling, one needs to predict decay channels. Typically, transition intensities of small molecules can be readily solved by fully computing the square of the transition moment integral. In diatomics, this involves rotational states, which luckily have constraints via rotational selection rules ($\Delta J = \pm 1$). Thus, only one or two repump lasers are needed to consistently shuttle population back to the rotational state of interest.

However, in polyatomic molecules, there are also vibrational contributions to the line intensity, for our purposes simplified as Franck-Condon factors (FCFs), which can be compared as a first approximation to the experimental vibrational branching ratios (VBRs) and help us predict the distribution of intensity among vibrational transitions:

$$q_{\nu' \to \nu''} = \left| \int \Psi^*_{\nu'} \Psi_{\nu''} d\tau_n \right|^2 \tag{1.1}$$

$$\text{Note: } \sum_{\nu'} q_{\nu' \to \nu''} = \sum_{\nu''} q_{\nu' \to \nu''} = 1$$

Where appropriate, we incorporate higher-order effects into the wavefunctions, use model Hamiltonians or solve exact quantum dynamics to accurately predict all transitions and potential loss channels that could affect laser-cooling efficiency.

For direct laser cooling, we attempt to design molecules where a single transition has $q_{\nu' \to \nu''} \approx 1$, so that many photon scatters can occur in our closed-loop without large population decay to other vibrational states. When a transition has the property that $q \approx 1$

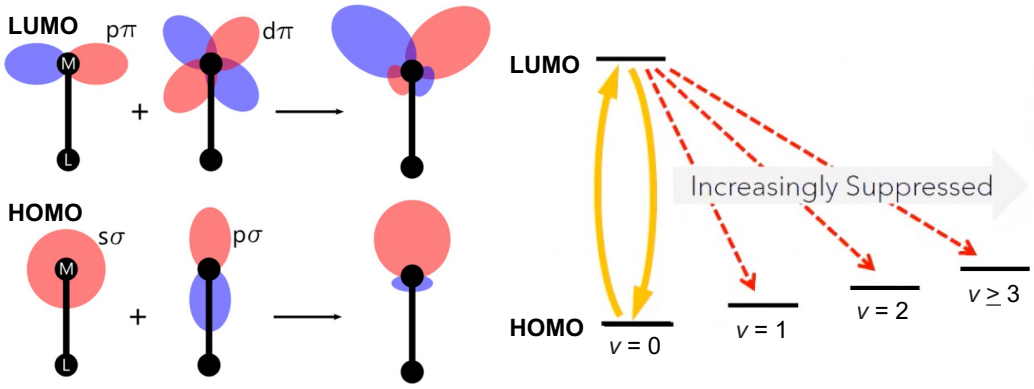

Figure 1.2: Metal-oxygen-ligand (MOR) framework for directly laser cooling molecules [15]. The orbitals involved in the transition are highly localized on the metal center to decouple from vibrations.

for $v' = v''$, we call this transition "diagonal" because the FCFs in the matrix approximate a diagonal matrix. The transition most close to 1 is often referred to as the fundamental transition or "diagonal" and all other transitions as "off-diagonal".

To increase the diagonality of the FCF, vibrational eigenstates between transitions should be increasingly similar (their wavefunction overlap is maximized), thus more similar molecular geometries between the ground and excited states. This is accomplished by creating electronic transitions that are increasingly "decoupled" from their environment, suppressing off-diagonal decays (Fig. 1.2). One decoupling strategy is to localize the electron density spatially for the electronic transition of interest. To accomplish this, we adopt a metal-oxygen-ligand framework (MOR), where the electron is localized on the alkaline-earth metal and acts atom-like.

In **Chapter 2**, we theoretically predict all possible decay paths in a small molecule, and show how it can be directly laser cooled. Additionally, we design novel mechanisms to generate ultracold fragments interesting to astrophysics, such as ultracold hydrogen. In **Chapter 3**, we expand the laser cooling framework and our theoretical methods to predict candidates beyond diatomic molecules to polyatomic molecules, such as calcium phenoxides.

We demonstrate we can design molecular optical-cycling centers that use the same number of lasers as smaller molecules despite the increase in vibrational modes. We continue this established M-O-R framework and demonstrate the ligand can be expanded to larger arenes and fully saturated hydrocarbons, presented in **Chapter 4**. This demonstration of larger organic scaffolds extends naturally to placing OCCs on solid-state surfaces and investigating novel effects with multiple OCCs, which we discuss in **Chapter 5**. Lastly, these design principles were explored in other phases of matter, such as aqueous solution, for quantum sensing applications. We investigate inorganic lanthanide complexes with ultranarrow linewidths, discussed in **Chapter 6**. Throughout this work, we hope to demonstrate that simple chemical principles can be utilized for rapid advancement in this field with driven, intentional molecular complexity.

CHAPTER 2

Probing the Limits of Optical Cycling in a Predissociative Diatomic

2.1 Introduction to Molecular Laser-Cooling

Rapid and repeated photon scattering is not only an efficient method of removing entropy from an atom or a molecule via photon recoils [18], but it also enables high-fidelity single quantum state preparation and measurement needed for quantum information protocols [19, 20]. Optical cycling between the ground state and a low-lying electronic excited state, pioneered with SrF [21] and CaF [22, 23], has led to recent progress with laser-cooled molecules such as tweezer arrays of CaF [8], a three-dimensional lattice of YO [24], magneto-optical trapping (MOT) of CaOH [17] and one-dimensional Sisyphus cooling of $CaOCH_3$ [25].

The primary challenge of direct laser cooling is the large photon budget necessary for bringing a cryogenically precooled molecular beam to within the MOT capture velocity [26, 27]. For example, typical molecular beams emanating from a cryogenic buffer gas beam (CBGB) source travel at mean forward velocities of ~ 200 m/s [28]. The recoil velocity per photon is ~ 2 cm/s, hence $> 10^4$ photon scatters are needed to bring the molecular beam to a standstill. The photons must be scattered faster than 10^6 s^{-1} to accomplish slowing within a ~ 1 m distance. Satisfying these criteria can be challenging for molecules with complex internal structures. Indeed, alternative slowing schemes such as travelling wave Stark deceleration [29], electro-optic Sisyphus effect [30], centrifuge deceleration [31] and Zeeman-Sisyphus slowing [32] have been demonstrated. These alternative schemes leverage

state-dependent electric and magnetic field dependencies to remove entropy with minimal photon scatters. However, quantum-state resolved detection still requires optical cycling.

Although calcium monohydride (CaH) was among the earliest candidates proposed for laser cooling [33], experimental progress was made only recently [34]. One of the reasons is the unique electronic structure of CaH compared to alkaline-earth monohalides [35]. In CaH, the lowest-energy excited state $A^2\Pi_{1/2}$ ($v' = 0$) lies 556 cm^{-1} above the Ca(^1S)+H(^2S) dissociation threshold of the ground $X^2\Sigma^+$ manifold (Fig. 2.1(a)), so a molecule in the excited state could decay into the continuum via a radiationless transition. This phenomenon, known as predissociation [36, 37], is traditionally studied by observing spectral line shapes and widths inconsistent with radiative decay. A predissociated molecule cannot be repumped into optical cycling because of the significant physical separation and relative velocity of the fragments. Hence the predissociation probability (P_{pd}) sets a limit on the number of photons one can scatter with laser cooling.

Despite the fact that the $A^2\Pi$ state in CaH lies above the ground state threshold energy, predissociation from $A^2\Pi$ to the $X^2\Sigma^+$ continuum is nominally forbidden due to the von Neumann-Wigner non-crossing rule [38]. For diatomic molecules, states with different symmetries cross while those with the same symmetries form avoided crossings [39, 40] (*i.e.*, the molecular Hamiltonian does not couple states with different symmetries). The second-lowest excited $B^2\Sigma^+$ state is allowed to predissociate. However, effects such as spin-orbit coupling can lead to mixing of $A^2\Pi$ and $B^2\Sigma^+$ states resulting in a small but finite P_{pd} for $A^2\Pi$. Both A and B states are important for efficient optical cycling.

In this work, we present theoretical analysis and measurements of predissociation probability for the $B^2\Sigma^+$ state of CaH. We perform *ab initio* calculations of the potential energy surfaces for CaH and confirm their accuracy by comparing the Franck-Condon factors (FCFs) for the primary $A^2\Pi_{1/2} \rightarrow X^2\Sigma^+$ and $B^2\Sigma^+ \rightarrow X^2\Sigma^+$ decays to our previous measurements. We calculate a nonradiative decay rate and obtain an estimate of P_{pd} by comparing it to the radiative decay rate. Next, we present a novel experimental protocol to measure an upper

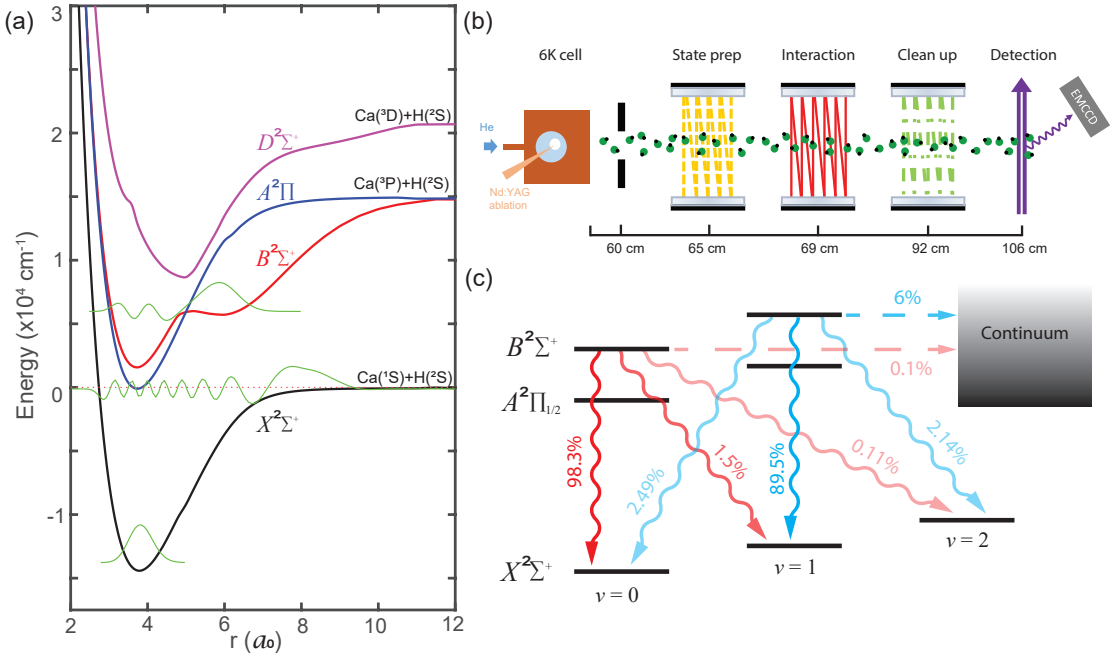

Figure 2.1: CaH molecular properties relevant to this work. (a) Potential energy surfaces (PES) for the 4 lowest electronic states: $X^2\Sigma^+$, $A^2\Pi$, $B^2\Sigma^+$ and $D^2\Sigma^+$. Spin-orbit interaction is omitted. The x-axis is the internuclear separation r in Bohr radii (a_0) and the y-axis is energy in cm^{-1} (1 cm^{-1} $\approx$ 30 GHz). The energy origin is chosen as the Ca(^1S)+H(^2S) continuum threshold ($v_{\rm th}$). Superimposed are the wavefunctions (bottom to top) for the $X(v'' = 0)$ absolute ground state, $X(v'' = 15)$ least-bound state and $B(v' = 4)$ excited state. (b) Experimental layout used in this work. A buffer-gas cooled molecular beam emanates from the cryogenic cell and encounters 4 spatially separated regions: state preparation (S), interaction (I), cleanup (C) and detection (D). Each region includes multipassed lasers described in the text. The diagram is not aligned to scale. (c) Relevant vibrational branching ratios (squiggly arrows) calculated for the $B^2\Sigma^+$ state. The hyperfine structure of the excited states is unresolved. Measured predissociation probabilities for $B(v' = 0)$ and $B(v' = 1)$ are denoted by dashed lines.

bound of $P_{\rm pd}$. We find that $P_{\rm pd} \approx 1 \times 10^{-3}$ for the vibrational ground state ($v' = 0$) and $\approx 6 \times 10^{-2}$ for the first vibrationally excited state ($v' = 1$) of the $B^2\Sigma^+$ manifold. We deduce that the vibrational ground state of the $A^2\Pi_{1/2}$ manifold predissociates with a $\sim 5 \times 10^{-7}$ probability due to spin-orbit mixing with the B state. The measured values of $P_{\rm pd}$ imply a

$\sim 50\%$ predissociative molecule loss after scattering 10^4 photons, suggesting that a MOT of CaH is feasible. We further extract the dipole matrix elements for all transitions connecting the ground $X^2\Sigma^+$ (v'') states to the excited $B^2\Sigma^+$ (v') states. This allows us to predict a viable stimulated Raman adiabatic passage (STIRAP) pathway to controllably dissociate the CaH molecules and subsequently trap the resulting ultracold hydrogen atoms, which is a prospective goal for molecular laser cooling and cold chemistry research [41].

2.2 Methods

2.2.1 Computational Methods

The starting point for our calculations is the construction of the potential energy surface (PES) for CaH. All calculations are performed using the Molpro program [42–44]. We adopt a basis set and active space as in Ref. [45], where we use cc-pwCVQZ [46] for the Ca atom and aug-cc-pVQZ [47] for the H atom. Calculations are performed in C_{2v} symmetry, which is the nearest Abelian point group to $C_{\infty v}$. Orbitals are generated with a restricted Hartree-Fock formalism (RHF), then further optimized in a state-averaged complete active space self-consistent field (SA-CASSCF) [48] calculation involving three active electrons and nine active orbitals. For the Σ^+ states, four states are averaged at equal weights in the SA-CASSCF calculation, with (5,2,2,0) closed and (9,4,4,1) occupied orbitals.

For the $A^2\Pi$ state, since only Abelian group symmetries are available, a two-state SA-CASSCF calculation with the same active space is performed in C_{2v} symmetry involving symmetries 2 and 3 of equal weight to represent the $C_{\infty v}$ A state. These wavefunctions are then used in a multireference configuration interaction calculation with Davidson corrections for higher excitations (MRCI+Q) [49–51]. Here, (3,1,1,0) orbitals make up the core, (5,2,2,0) are closed and (9,4,4,1) are occupied. Electron correlation involving double and single excitations are allowed. The spin-orbit interaction is incorporated at the MRCI level using the Breit-Pauli Hamiltonian [52].

Next, we generate the vibrational wavefunctions to calculate the Frank-Condon factors (FCFs) for the CaH transitions of interest. The following three-state Hamiltonian (for the $X^2\Sigma^+$, $B^2\Sigma^+$ and $D^2\Sigma^+$ electronic states) is diagonalized to obtain wavefunctions, Franck-Condon factors (listed in Table 2.1 and compared to experimental vibrational branching ratios) and predissociation estimates:

$$\sum_j^3 H_j = \sum_I \frac{(\hat{p}^I + A_{ij}^I(r))^2}{2\mu}\phi_j(r) + V_j(r)\phi_j(r). \tag{2.1}$$

The first term is the kinetic energy operator, in which $\hat{p}$ is the standard momentum operator, expressed on a grid via the Colbert-Miller derivative [53]. We represent the momentum operator in position space so that we can incorporate the nonadiabatic coupling term directly [54]. This term is computed in the position representation, $A_{ij}(r) = \langle \Psi_i | \hat{p} \Psi_j \rangle$.

Transition	Vibrational Quanta (v'')	FCF Calculated ($f_{0v''}$)	FCF Measured ($f_{0v''}$)
$A \rightarrow X$	0	0.9788	0.9572(43)
	1	0.0205	0.0386(32)
	2	6.8×10^{-4}	$4.2(3.2)\times10^{-3}$
	3	4.1×10^{-5}	-
$B \rightarrow X$	0	0.9789	0.9807(13)
	1	0.0192	0.0173(13)
	2	1.8×10^{-3}	$2.0(0.3)\times10^{-3}$
	3	1.4×10^{-4}	-

Table 2.1: The calculated FCFs for CaH, compared to experimental FCFs [34]. The experimental FCFs are derived from measured vibrational branching ratios (VBRs). Note that the active space was optimized for the B state in this work.

We obtained $\langle \Psi i | \frac{\partial}{\partial r} \Psi_j \rangle$ from a $dr = 0.001 a_0$ potential energy surface scan via Molpro electronic structure calculations and interpolated this onto a spline to represent $A_{ij}(r)$ [55].

The reduced mass of CaH is μ. Finally, $V(r)$ is obtained from the $dr = 0.001a_0$ scan via the MRCI+Q Davidson energies and interpolated onto a spline before being incorporated into the Hamiltonian.

Predissociation probability estimates were computed using an optical absorbing potential which previously predicted scattering cross sections close to experiment [56–58]. At $r_0 = 8$ a.u., an optical potential of the form $-iV(r - r_0)^2/w^2$ was added only to the $X^2\Sigma^+$ state's $V(r)$ at the PES asymptote with each grid-point to simulate the continuum and create a flux equation. Results were insensitive to absorber placement as long as it is placed along the potential energy surface's asymptote and has a width larger than the typical de Broglie wavelength [58]. Specifically, the optical absorbing potential must have a width w and depth V which guarantees complete wavepacket absorption and ensures the potential is smooth so that hardly any reflection takes place before the wavepacket enters the potential [59]. The absorber width was chosen to be $w = 8\ a_0$, much larger than the typical de Broglie wavelength of $\sim 0.2\ a_0$. We chose a depth as the typical energy of the wavepacket, or 0.2 a.u. (4.4×10^4 cm^{-1}). The Hamiltonian was then diagonalized to obtain eigenvalues and eigenvectors. Our calculations converged with a grid-spacing (dr) of 0.007 a_0 and a box size of 16.5 a_0. The optical potential created a channeled flux equation which imposed a boundary condition on the wavefunction and eigenvalues gained an imaginary component.

This component, such as the imaginary eigenvalue of $B(v' = 0)$, is directly related to the nonadiabatic coupling between that vibrational wavefunction and the X continuum (where we placed the absorber) as the nonradiative transition rate A_{NR}. We estimated the predissociation probability as the ratio of the calculated nonradiative (A_{NR}) and radiative (A_R) decay rates, $A_{\mathrm{NR}}/(A_{\mathrm{NR}} + A_R)$. Further details are discussed in the supplementary information of Ref. [60].

2.2.2 Experimental Methods

The experimental setup has been previously described [34]. Briefly, CaH is generated through ablation of a CaH_2 target by a pulsed Nd:YAG laser at a ~ 1 Hz rate. CaH is buffer-gas cooled by helium at 6 K and ejected from the cell aperture to form a beam. The molecules are predominately in the $X^2\Sigma^+$ ($v'' = 0$) state. The beam of CaH then enters a high-vacuum chamber which is divided into four regions: state preparation, interaction, cleanup and detection, as shown in Fig. 2.1(b). In the first three regions, the molecular beam intersects with transverse lasers that address $X \rightarrow A$ or $X \rightarrow B$ transitions. These lasers can be switched on and off by independent optical shutters. The laser beams are multipassed to increase the interaction time with the molecular beam. In the detection region, we apply a single-pass $X \rightarrow A$ or $X \rightarrow B$ light and use an iXon888 electron multiplying charge coupled device (EMCCD) camera and a Hamamatsu R13456 photomultiplier tube to collect the laser-induced fluorescence (LIF) signals for spatially and temporally resolved detection. Every molecule scatters ~ 20 photons in the detection region, which implies that we are not sensitive to the initial spin-rotation and hyperfine distribution. All addressed transitions are from the $X^2\Sigma^+$ ($N'' = 1$) state (N is the rotational quantum number) to $A^2\Pi_{1/2}$ ($J' = 1/2$) (J is the total angular momentum quantum number) or $B^2\Sigma^+$ ($N' = 0$) states in order to obtain rotational closure [33]. We use electro-optic modulators (EOMs) to generate sidebands on all lasers to cover all hyperfine states (HFS) as well as to address spin-rotation manifolds. The transitions used here were first measured experimentally with HFS resolution.

To concisely describe the lasers used in this study we adopt the notation $M^R_{v'-v''}$, which denotes the transitions addressed and the spatial positions of the lasers. M is A or B, representing the electronic state of the excited manifold. R is S, I, C, or D (state preparation, interaction, cleanup or detection region). In addition, the $F_{Mv'v''}$ notation describes the vibrational branching ratios (VBR) from either $A^2\Pi_{1/2}$ or $B^2\Sigma^+$ states (represented by M) to $X^2\Sigma^+$ states. For example, F_{B01} is VBR from $B^2\Sigma^+$ ($v' = 0$) to $X^2\Sigma^+$ ($v'' = 1$). We use similar notation, F_{B0a} and F_{B1a}, to represent predissociation probabilities from $B^2\Sigma^+$

$(v' = 0)$ and $(v' = 1)$ states.

2.3 Results and Discussion

2.3.1 $B^2\Sigma^+$ $(v' = 0)$ Predissociation Measurement Method

To measure the predissociation probability of the $B^2\Sigma^+$ $(v' = 0)$ state, we need to scatter many photons via $B^2\Sigma^+$ $(v' = 0)$ and detect population loss that cannot be explained by known effects, predominantly rovibrational losses. To characterize the loss we design several experimental stages, each stage corresponding to a unique configuration of lasers interacting with the molecular beam. We monitor the population of the $v'' = 0$ ground state in the detection region by detecting LIF signals from the B^D_{0-0} laser. For this measurement we employ six stages. By defining temporally stable parameters that describe the properties of our system, we can express the molecular population distribution at each stage.

For example, in the *Unperturbed* stage we detect $X(v'' = 0)$ population denoted by N. This is the calibration signal used as a reference. In the *Cleanup* stage we apply the B^C_{0-1} laser and the resulting $X(v'' = 0)$ population is $N + n_1 N\kappa F_{B00}/\mathcal{F}_{B0}$ where n_1 is the normalized natural population of $X(v'' = 1)$, κ is the cleanup laser efficiency and $\mathcal{F}_{B_0} \equiv F_{B0a} + \sum_{i\neq 1} F_{B0i}$ is the VBR normalization factor. This factor accounts for the discrete probability distribution of decay processes based on the VBRs and P_{pd}. By taking the ratio of the integrated signal of the $X(v'' = 0)$ population from *Cleanup* stage with signal from *Unperturbed* stage, we get the parameterized ratio $R_1 = 1 + n_1\kappa F_{B00}/\mathcal{F}_{B0}$. In addition to the *Unperturbed* and *Cleanup* stages, we have four more stages in this measurement, resulting in a total of five ratios and five parameters (including P_{pd}). The details of all the stages, such as the laser configurations and expressions for the normalized signal, are in Table 2.2. Thus we acquire five equations (measured ratios equal to the parameterized expressions) and five variables. We can solve the equations and express F_{B0a} via R_is. By precisely measuring R_i we can estimate the $B^2\Sigma^+$ $(v' = 0)$ predissociation probability.

Purpose	Upstream laser config.	Downstream normalized $X^2\Sigma^+$ $(v''=0)$ state population	Averaged signal ratio
Unperturbed	-	1	-
Cleanup	B^C_{0-1}	$1+n_1\kappa F_{B00}/\mathcal{F}_{B_0}$	1.05(2)
X-A Cycling	A^I_{0-0}	d_A	0.018(6)
X-A Cycling + Cleanup	$A^I_{0-0}+B^C_{0-1}$	$d_A+[(1-d_A)F_{A01}/\mathcal{F}_{A_0}+n_1]\kappa F_{B00}/\mathcal{F}_{B_0}$	0.94(2)
X-B Cycling	B^I_{0-0}	d_B	0.086(8)
X-B Cycling + Cleanup	$B^I_{0-0}+B^C_{0-1}$	$d_B+[(1-d_B)F_{B01}/\mathcal{F}_{B_1}+n_1]\kappa F_{B00}/\mathcal{F}_{B_0}$	0.87(2)

Table 2.2: Experimental stages for $B(v'=0)$ state predissociation measurement. In the second column, $M^R_{v'-v''}$ denotes the laser information. M is A or B, representing the electronic excited state. R is the region S, I, or C (see text). The third column contains the normalized ground-state populations using unknown variables and calculated VBRs. The five variables n_1, κ, F_{B0a}, d_A and d_B represent $X(v''=1)$ state natural population, cleanup efficiency of laser B^C_{1-0}, $B(v'=0)$ state predissociation probability, depletion efficiency of laser A^I_{0-0} and depletion efficiency of laser B^I_{0-0}. We denote the VBR normalization factors as $\mathcal{F}_{A_0}\equiv\sum_{i\neq 0}F_{A0i}$, $\mathcal{F}_{B_0}\equiv F_{B0a}+\sum_{i\neq 1}F_{B0i}$ and $\mathcal{F}_{B_1}\equiv F_{B0a}+\sum_{i\neq 0}F_{B0i}$.

2.3.2 $B^2\Sigma^+$ $(v'=1)$ Predissociation Measurement Method

For the $B(v'=1)$ state, predissociation is also measured within the framework of stages. We implement two different methods, each consisting of multiple laser configurations, to measure the same quantity. In method I we use six stages, always monitoring the $X(v''=0)$ population downstream using laser A^D_{0-0}. The aim is to populate $X(v''=1)$ via an off-diagonal pumping laser A^S_{1-0} and perform optical cycling between $X(v''=1)$ and $B(v'=1)$. We expect to see an increase of the $X(v''=0)$ population as a result of the cycling. We repump the molecules remaining in $X(v''=1)$ to $v''=0$. The recovered population might be less than expected due to vibrational loss. By ruling out other effects, we attribute the loss to $B(v'=1)$ predissociation. The details of the six stages are in Table 2.3.

Purpose	Upstream laser config.	Downstream normalized $X^2\Sigma^+$ ($v''=0$) state population	Averaged ratio
Unperturbed	-	1	-
State Prep	A^S_{1-0}	$1-a$	0.22(2)
Cleanup	A^C_{0-1}	$1+n_1\kappa F_{A00}/\mathcal{F}_{A_1}$	1.10(3)
State Prep + Cleanup	$A^S_{1-0}+A^C_{0-1}$	$1-a+(n_1+aF_{A11}/\mathcal{F}_{A_2})\kappa F_{A00}/\mathcal{F}_{A_1}$	1.01(3)
State Prep + X-B 1-1 Cycling	$A^S_{1-0}+B^I_{1-1}$	$1-a+(n_1+aF_{A11}/\mathcal{F}_{A_2})d_BF_{B10}/\mathcal{F}_{B_2}$	0.39(2)
State Prep + X-B 1-1 Cycling + Cleanup	$A^S_{1-0}+B^I_{1-1}$ + A^C_{0-1}	$1-a+(n_1+aF_{A11}/\mathcal{F}_{A_2})(d_BF_{B10}/\mathcal{F}_{B_2}$ $+(1-d_B)\kappa F_{A00}/\mathcal{F}_{A_1})$	0.40(2)

Table 2.3: Method I of $B^2\Sigma^+$ ($v'=1$) predissociation measurement. Notation is similar to Table 2.2. In the third column, the variables include a, n_1, κ, F_{B1a} and d_B, representing state preparation (from $X(v''=0)$ to $X(v''=1)$) efficiency, $X(v''=1)$ natural population, cleanup efficiency of laser A^C_{0-1}, $B(v'=1)$ predissociation probability and depletion efficiency of laser B^I_{1-1}. The VBR normalization factors are $\mathcal{F}_{A_1}\equiv\sum_{i\neq 1}F_{A0i}$, $\mathcal{F}_{A_2}\equiv\sum_{i\neq 0}F_{A1i}$ and $\mathcal{F}_{B_2}\equiv F_{B1a}+\sum_{i\neq 1}F_{B1i}$.

Method II differs in several ways. We monitor the $X(v''=1)$ population instead of $v''=0$, accounting for loss to both $v''=0$ and $v''=2$ with a sufficient signal-to-noise ratio (SNR) using laser B^D_{1-1}. The ten stages in this method lead to nine measured ratios. And the seven required parameters imply that there are more equations than variables. To find the optimal solution of this over-constrained system, we define a least-squares objective function and use the Levenberg-Marquardt algorithm to search for the local minimum in the parameter space with reasonable initial guesses.

2.3.3 Predissociation Measurement Analysis

The yield of our CBGB source exhibits some slow drift. In order to reduce errors due to molecule number fluctuations, we inserted a reference stage before and after every other

stage within a group when taking data. For example, in the $B(v' = 0)$ predissociation measurement, data was taken in the following order: *Unperturbed* $\rightarrow$ *Cleanup* $\rightarrow$ *Unperturbed* $\rightarrow$ *X-A Cycling* $\rightarrow$ *Unperturbed ... X-B Cycling + Cleanup* $\rightarrow$ *Unperturbed*. The reference stage for $B(v' = 1)$ method I is *Unperturbed*, while for method II it is *State Prep + Cleanup v0*. To calculate the ratios, we divide the signal by the average signal from the calibration shots before and after. The entire group of measurements is repeated multiple times. The averaged ratios can be found in Tables 2.2, 2.3 and 2.4. The values in parentheses denote the 2σ statistical errors. A graphical representation of the analysis process and histograms of all five ratios can be found in Fig. 2.2.

With the ratios measured, we use a bootstrap method [61–63] to derive the mean values and build the confidence intervals of the predissociation probabilities depicted in Fig. 2.3. This method is particularly useful as it does not require any assumptions about the data such as independence assumptions typically made for standard error calculations. We considered several other analysis methods, such as pairwise bootstrapping and regular error propagation and the outcomes were all in agreement with each other. Details of the bootstrap method are in the SI of Ref. [60].

After considering all systematic effects and analyzing statistical errors, we find the predissociation probability for the $B^2\Sigma^+$ $(v' = 0)$ state to be $0.00097^{+0.00059}_{-0.00057}$ and for the $B^2\Sigma^+$ $(v' = 1)$ state to be $0.056^{+0.044}_{-0.034}$. The reported value for $B(v' = 1)$ is the average of the two methods (method I yields $0.079^{+0.021}_{-0.017}$ and method II yields $0.033^{+0.013}_{-0.011}$) and the 95% confidence interval is the largest of the two methods combined. These values are consistent with the probabilities calculated in Fig. 2.3 within an order of magnitude. Other potential loss channels are discussed in the Appendix of [60]. In addition, to demonstrate the robustness of our measurements to small variations in FCFs, we perform a comparative analysis by utilizing the FCFs obtained in previous theoretical work on CaH [35, 64]. The results consistently produce nonzero predissociation probabilities and are within error bars of each other. The sharp monotonic increase in P_{pd} seen in Fig. 2.3 can be understood as a bound

Purpose	Upstream laser config.	Downstream normalized $X^2\Sigma^+$ ($v''=1$) state population	Average ratio
State Prep + Cleanup v0	$A^S_{1-0}+A^C_{1-0}$	$n_1+(a+\kappa_1-a\kappa_1)F_{A11}/\mathcal{F}_{A_2}$	-
Unperturbed	-	n_1	0.13(3)
State Prep	A^S_{1-0}	$n_1+aF_{A11}/\mathcal{F}_{A_2}\equiv\mathcal{Z}$	0.89(4)
Cleanup v0	A^C_{1-0}	$n_1+\kappa_1F_{A11}/\mathcal{F}_{A_2}$	0.93(4)
State Prep + X-A 1-1 Cycling	$A^S_{1-0}+A^I_{1-1}$	$\mathcal{Z}(1-d_A)$	0.03(3)
State Prep + X-A 1-1 Cycling + Cleanup v0	$A^S_{1-0}+A^I_{1-1}+A^C_{1-0}$	$\mathcal{Z}(1-d_A)+$ $(1-a+\mathcal{Z}d_AF_{A10}/\mathcal{F}_{A_3})\kappa_1F_{A11}/\mathcal{F}_{A_2}$	0.33(3)
State Prep + X-A 1-1 Cycling + Cleanup v2	$A^S_{1-0}+A^I_{1-1}+A^C_{1-2}$	$\mathcal{Z}(1-d_A)+$ $(aF_{A12}/\mathcal{F}_{A_2}+\mathcal{Z}d_AF_{A12}/\mathcal{F}_{A_3})\kappa_2F_{A11}/\mathcal{F}_{A_4}$	0.57(4)
State Prep + X-B 1-1 Cycling	$A^S_{1-0}+B^I_{1-1}$	$\mathcal{Z}(1-d_B)$	0.12(3)
State Prep + X-B 1-1 Cycling + Cleanup v0	$A^S_{1-0}+B^I_{1-1}+A^C_{1-0}$	$\mathcal{Z}(1-d_B)+$ $(1-a+\mathcal{Z}d_BF_{B10}/\mathcal{F}_{B_2})\kappa_1F_{A11}/\mathcal{F}_{A_2}$	0.35(3)
State Prep + X-B 1-1 Cycling + Cleanup v2	$A^S_{1-0}+B^I_{1-1}+A^C_{1-2}$	$\mathcal{Z}(1-d_B)+$ $(aF_{A12}/\mathcal{F}_{A_2}+\mathcal{Z}d_BF_{B12}/\mathcal{F}_{B_2})\kappa_2F_{A11}/\mathcal{F}_{A_4}$	0.42(3)

Table 2.4: Method II of $B^2\Sigma^+$ ($v'=1$) predissociation measurement. In the third column, the seven variables include a, n_1, κ_1, κ_2, F_{B1a}, d_A and d_B, representing state preparation (from $X(v''=0)$ to $X(v''=1)$) efficiency, $X(v''=1)$ natural population, cleanup efficiency of laser A^C_{1-0}, cleanup efficiency of laser A^C_{1-2}, $B(v'=1)$ predissociation probability, depletion efficiency of laser A^I_{1-1} and depletion efficiency of laser B^I_{1-1}. The VBR normalization factors are $\mathcal{F}_{A_2}\equiv\sum_{i\neq0}F_{A1i}$, $\mathcal{F}_{A_3}\equiv\sum_{i\neq1}F_{A1i}$, $\mathcal{F}_{A_4}\equiv\sum_{i\neq2}F_{A1i}$ and $\mathcal{F}_{B_2}\equiv F_{B1a}+\sum_{i\neq1}F_{B1i}$.

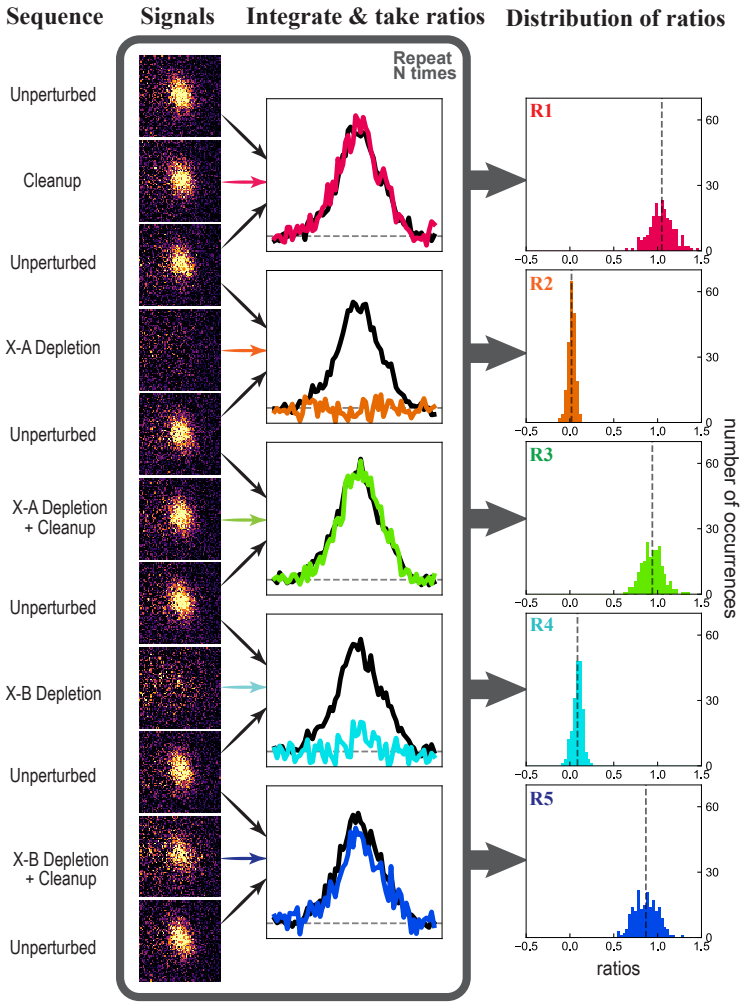

Figure 2.2: Illustration of the ratio extraction process for the B($v' = 0$) predissociation measurement. We run the stages sequentially with a n interlaced reference stage, and collect LIF with an EMCCD. We integrate the images along both axes to obtain the signals, which we then used to calculate ratios. By repeating the entire sequence N times, we collect N sets of five ratios. Here we first show examples of one-shot camera images. We then present the integrated signal along one axis, using colored traces for science stages and black for reference stages (horizontal lines are the baselines). Finally we show the histograms of the five ratios. Vertical dashed lines represent the means of the ratios.

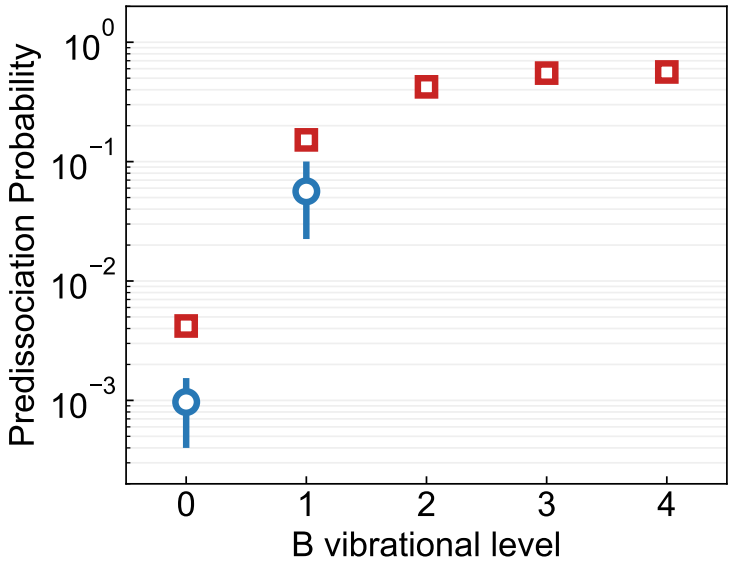

Figure 2.3: CaH predissociation. Red squares are theoretical results for nonradiative decay rates of different vibrational states of $B^2\Sigma^+$. Blue circles are experimental results, where error bars represent the 95% confidence interval.

molecule quantum tunneling through the $B^2\Sigma^+$ potential into the $X^2\Sigma^+$ continuum at the same energy. As the energy of the incident quantum state increases, so does the transmission probability, which is aided by stronger wavefunction overlaps.

2.3.4 $A^2\Pi_{1/2}$ Predissociation Estimate

The $A^2\Pi$ state in CaH does not undergo predissociation via the process described for the $B^2\Sigma^+$ state. However, spin-orbit coupling (SOC) can induce mixing between the A and B states, leading to non-vanishing predissociation of the $A^2\Pi_{1/2}$ spin-orbit state. For a linear molecule, the z-component of total angular momentum, J_z, is a good quantum number. Therefore the spin-orbit component $A^2\Pi_{1/2}$ can interact with $B^2\Sigma^+(J_z = 1/2)$ due to the same J_z value. A similar interaction exists between $A^2\Pi_{1/2}$ and $X^2\Sigma^+(J_z = 1/2)$ but the energy separation is much larger ($\sim$14,000 cm^{-1}) compared to that between the A and B states ($\sim$1,400 cm^{-1}). Higher vibrational states of the X manifold are closer in energy to

	$A^2\Pi_x$ $(v=0, m_s=1/2)$	$A^2\Pi_y$ $(v=0, m_s=1/2)$	$B^2\Sigma^+$ $(v=0, m_s=-1/2)$
$A^2\Pi_x$ $(v=0, m_s=1/2)$	0	-35.5i	21.5
$A^2\Pi_y$ $(v=0, m_s=1/2)$	35.5i	0	-21.5i
$B^2\Sigma^+$ $(v=0, m_s=-1/2)$	21.5	21.5i	1400

	$A^2\Pi_x$ $(v=1, m_s=1/2)$	$A^2\Pi_y$ $(v=1, m_s=1/2)$	$B^2\Sigma^+$ $(v=0, m_s=-1/2)$	$B^2\Sigma^+$ $(v=1, m_s=-1/2)$
$A^2\Pi_x$ $(v=1, m_s=1/2)$	0	-35.5i	21.5f	21.5
$A^2\Pi_y$ $(v=1, m_s=1/2)$	35.5i	0	-(21.5f)i	-21.5i
$B^2\Sigma^+$ $(v=0, m_s=-1/2)$	21.5f	(21.5f)i	64	0
$B^2\Sigma^+$ $(v=1, m_s=-1/2)$	21.5	21.5i	0	1310

Table 2.5: Spin-orbit matrices accounting for vibrational mixing of the A and B states. The Π_x and Π_y basis states split under SOC to produce $\Pi_{1/2}$ and $\Pi_{3/2}$ states. The top matrix is for $A^2\Pi$ $(v'=0)$ and $B^2\Sigma^+$ $(v'=0)$, while the bottom one is for $A^2\Pi$ $(v'=1)$, $B^2\Sigma^+$ $(v'=1)$ and $B^2\Sigma^+$ $(v'=0)$. The Franck-Condon factor f is introduced to account for the off-diagonal vibrational wavefunction overlap. The diagonal terms represent the energies of unperturbed states. All values are in cm^{-1}.

A but the effective coupling to the states relevant for laser cooling is weaker due to a poor vibrational wavefunction overlap.

We estimate the mixing between the $A(v'=0)$ and the $B(v'=0)$ states separated by 1400 cm^{-1}. The spin-orbit parameters were obtained with the Breit-Pauli Hamiltonian [52] at the MRCI level and are given in Table 2.5. Diagonalization of this Hamiltonian matrix leads to a 0.05% $B(v'=0)$ admixture into the $A(v'=0)$ state. Similarly, we can compute the mixing between $A(v'=1)$, $B(v'=0)$ and $B(v'=1)$. The coupling between $A(v'=1)$ and $B(v'=1)$ is expected to be similar to the case of $v'=0$ since the energy difference of 1310 cm^{-1} is similar to that in the case of $v'=0$. However, the $A(v'=1)$ and $B(v'=0)$ states are only 64 cm^{-1} apart, hence even a small FCF can lead to significant mixing. Note that the measured FCF for the $A(v'=0) \rightarrow X(v''=1)$ transition is 4% (Table 2.1) and that our calculated $A-B$ bond length difference is smaller than the $X-A$ bond length. We use $f=5\%$ as an upper limit for the $A(v'=1) \rightarrow B(v'=0)$ FCF. Diagonalization of the corresponding Hamiltonian matrix in Table 2.5 yields a 8.4% $B(v'=0)$ character for $A(v'=1)$. Combining these admixtures with the measured P_{pd} for $B(v'=0,1)$, we estimate that the $A(v'=0)$ state very weakly predissociates with a probability of $\sim 5\times10^{-7}$ and the $A(v'=1)$ state with a higher probability of $\sim 3\times10^{-5}$. The FCF used here is an upper-bound value and therefore the estimated probabilities serve as upper bounds.

2.3.5 Controlled Dissociation Pathway

As mentioned in Ch. 2.1, an enticing application of ultracold CaH and other molecules is controlled dissociation into fragments that are not directly laser-coolable, such as H. In order to trap the resulting H atoms, the IR maximum kinetic energy must be below typical optical trap depths. A magic-wavelength trap for H atoms at 513 nm has a depth of 1.2 kHz per 10 kW/cm^2 [65]. A practical dipole trap with an intensity of at most ∼100 kW/cm^2 would result in a maximum trap depth of only ~ 0.5 μK. Since the binding energy of B$(v'=0)$ corresponds to a temperature of $\sim 1,000$ K, the trapping of the fragments relies on the

ability to dissociate the molecules as close as possible to the threshold [41], such as via a stimulated two-photon process [66, 67].

Stimulated Raman adiabatic passage (STIRAP) is a technique that has been successfully employed to generate ground-state bialkali molecules starting from a weakly bound state [68, 69]. Although STIRAP has been predominantly demonstrated for adiabatic population transfers from weakly bound to deeply bound molecular states, the mechanism can be extended to unbound continuum states [70, 71]. A prerequisite for efficient transfer is the identification of an intermediate state that strongly couples to both initial and final states. Additionally, a desirable intermediate state would be connected via readily accessible laser wavelengths to the initial and final states.

Theory calculations give us access to branching ratios and line strengths for a multitude of vibrational levels, some of which have advantages for controlled dissociation. We calculate the dipole transition line strength $S_{v'v''}$, which is the square of the transition dipole moment ($|\langle v'|\,\mu\,|v''\rangle|^2$), for both $A^2\Pi_{1/2} \rightarrow X^2\Sigma^+$ and $B^2\Sigma^+ \rightarrow X^2\Sigma^+$ transitions (Figs. 2.4(a,b)). The PES' for the A and X states are similar in shape (Fig. 2.1(a)) which lead to highly diagonal transition strengths. However, the second minimum in the B state PES leads to strong off-diagonal coupling starting around $v' = 4$. This feature enables strong coupling of $B(v' = 4)$ to both $X(v'' = 0)$ and $X(v'' = 15)$ (Fig. 2.4(c)). Our calculations do not show a significant coupling between the $B(v' = 4)$ state and the vibrationally excited states of the A manifold. Here we calculate the coupling to the weakest bound state, rather than to the continuum, for two reasons. First, we expect the coupling to the lowest-energy continuum states and to the least-bound state to be similar since their energy difference is only ~ 500 cm^{-1}. Second, we expect the STIRAP process to be more efficient if all three states are bound states. Hence it is worthwhile to consider a transfer to $X(v'' = 15)$ followed by photodissociation [67] or Feshbach dissociation [72].

In Fig. 2.4(d) we plot the laser wavelengths required to connect $X(v'' = 0)$ as well as the ground-state continuum to the B manifold. We estimate that the "upleg" STIRAP

wavelength for $X(v''=0) \rightarrow B(v'=4)$ is 512.7 nm while the "downleg" wavelength for $B(v'=4) \rightarrow X(v''=v_{\mathrm{th}})$ is 1744.7 nm. Both of these wavelengths are accessible via current technology such as Raman fiber amplifiers and difference-frequency generation (DFG). Thus we expect high-power and narrow-linewidth laser sources to be within reach for STIRAP.

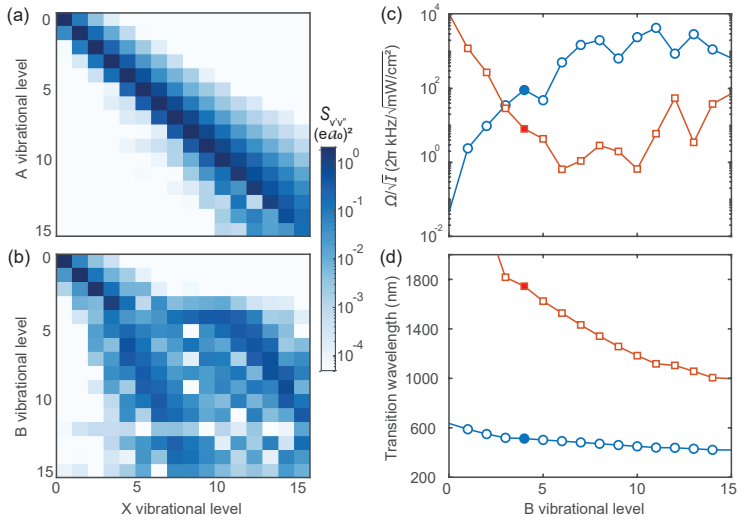

Figure 2.4: Suggested controlled dissociation pathway for CaH molecules. Line strengths ($S_{v'v''}$) in atomic units for dipole allowed transitions: (a) $X^2\Sigma^+$ (v'') $\rightarrow A^2\Pi_{1/2}$ (v') and (b) $X^2\Sigma^+$ (v'') $\rightarrow B^2\Sigma^+$ (v'). The A state potential is more harmonic as is reflected by the diagonal $S_{v'v''}$. The B state, however, significantly deviates from the diagonal starting around $v'=4$ because of the second potential minimum at $\sim 6\ a_0$ (Fig. 2.1(a)). Note that $B(v'=4)$ has comparable line strengths between $X(v''=0)$ and $X(v''=15)$. (c) Intensity-normalized Rabi rate ($\Omega/\sqrt{I} = \sqrt{S_{v'v''}}/\hbar$) for dipole transitions $X(v''=0) \rightarrow B(v')$ (red squares) and $B(v') \rightarrow X(v=15)$ (blue circles). Around $v'=4$ (shaded points), the Rabi rates are comparable. (d) Wavelengths in nanometers for optical transitions $X(v''=0) \rightarrow B(v')$ (blue circles) and $B(v') \rightarrow X(\text{continuum})$ (red squares). The theoretical energy differences were adjusted by a common offset of 240 cm^{-1} to match experimental data for $X(v''=0) \rightarrow B(v'=0,1,2)$ transitions [73]. The wavelengths corresponding to $v'=4$ (shaded points) are 512.7 nm and 1744.7 nm.

2.4 Conclusions

Predissociation is a challenge for laser cooling of new molecular species. We have theoretically and experimentally studied it for laser-cooling CaH as well as in the context of controlled ultracold dissociation. We find that the lowest-excited electronic state $A^2\Pi_{1/2}$ ($v' = 0$), which is the workhorse for optical cycling, only weakly predissociates ($P_{\rm pd} \approx 10^{-6}$) via spin-orbit coupling. The next excited manifold $B^2\Sigma^+$, crucial for repumping vibrational dark states, has much stronger predissociation by virtue of having the same symmetry as $X^2\Sigma^+$. We measure $P_{\rm pd}$ for $B(v' = 0)$ and $B(v' = 1)$ states and obtain $\sim 10^{-3}$ and $\sim 6 \times 10^{-2}$, respectively. This sharp increase is substantiated by theoretical calculations and we expect $P_{\rm pd} \to 1$ for $v' \gtrsim 4$. The results are summarized in Table 2.6.

State	Vibrational quantum (v'')	Radiative lifetime (ns)	Radiative decay rate (A_R, sec^{-1})	Nonradiative decay rate ($A_{\rm NR}$, sec^{-1})	Predissociation (PD) probability	Experimental PD probability
B	0	52.0	1.924×10^7	8.040×10^4	0.0042	$0.00097^{+0.00059}_{-0.00057}$
	1	54.3	1.842×10^7	3.304×10^6	0.1521	$0.056^{+0.044}_{-0.034}$
	2	58.9	1.698×10^7	1.245×10^7	0.4230	-
	3	78.2	1.278×10^7	1.571×10^7	0.5514	-
	4	59.2	1.688×10^7	2.181×10^7	0.5637	-
	5	83.9	1.193×10^7	5.482×10^7	0.8213	-
	6	84.4	1.185×10^7	5.960×10^7	0.8342	-
A	0	34.3	2.913×10^7	-	-	5×10^{-7}
	1	34.5	2.902×10^7	-	-	3×10^{-5}

Table 2.6: Theoretical and experimental values of predissociation probability for $B^2\Sigma^+$ and $A^2\Pi_{1/2}$. Both radiative (A_R) and non-radiative ($A_{\rm NR}$) decay rates are calculated. The radiative lifetime is $\tau \equiv 1/A_R$. Predissociation $P_{\rm pd}$ probability is defined as the ratio of the nonradiative decay rate to the total decay rate ($A_R + A_{\rm NR}$). Measurements of $P_{\rm pd}$ are only provided for the $B^2\Sigma^+$ ($v' = 0$) and ($v' = 1$) states. For the latter, we report the mean of two different measurement methods described in Section 2.3.2. The values given for the $A^2\Pi_{1/2}$ ($v' = 0$) and ($v' = 1$) states are estimated by calculating the spin-orbit mixing between A and B.

To obtain high photon scattering rates, one must repump the $A(v' = 0) \rightarrow X(v'' = 1)$ vibrational loss channel via the $B(v' = 0)$ state. Due to predissociation, we find that the optimal laser-cooling scheme requires avoiding the $B(v' \geq 1)$ states in favor of using the A manifold. On average, every cycling molecule will scatter ~ 20 photons $(1/(1 - F_{A00}))$ before being lost to $X(v'' = 1)$. Each of these molecules only needs to scatter one photon via $B(v' = 0)$ to return to cycling, but it will predissociate with a 0.1% probability. Hence we estimate that $\sim 50\%$ of molecules will be lost to predissociation after scattering the requisite $\sim 10^4$ photons.

Lastly, we propose to take advantage of the high predissociation probability for $B(v' = 4)$ state to engineer a two-photon STIRAP pathway for transferring the molecular population from the ground $X(v'' = 0)$ state to the low-energy continuum $X(v'' = v_{\mathrm{th}})$. We find that $B(v' = 4)$ couples strongly to both these X states via optical transitions at wavelengths within accessible laser technologies.

CHAPTER 3

Developing Molecular Optical Cycling Centers (OCCs)

3.1 Tuning Franck-Condon Factors with Electronic Substitution

3.1.1 Introduction

The use of isolated, complex systems in pure quantum states for computation, measurement and sensing relies on the ability to determine the quantum state of the system. This applies not only to state measurement, but also state preparation (and cooling), where initialization of the system to a pure quantum state is necessary to achieve quantum advantage [74].

For state preparation and measurement (SPAM), spontaneously emitted photons following excitation are often employed as carriers of information (entropy) since they can be transported efficiently between systems that differ widely in temperature, mass and size – characteristics that comprise the gap between the isolated quantum system and its effectively classical environment. However, the finite probability for detecting these photons (whose emission direction is usually randomized) means the cycle of excitation followed by spontaneous emission must be repeated many times (termed *optical cycling*) to achieve single-shot quantum state readout of single emitters. Gas phase atoms driven by narrow-band lasers can facilitate this process through selection rules governing how their quantum numbers change during spontaneous emission and have for many years been used in laser cooling, trapping and SPAM [75–78].

Molecules, on the other hand, have internal vibrational degrees of freedom that are typically not be constrained by angular momentum selection rules and electronically excited

molecules can decay to vibrationally excited levels of the ground electronic state. This vibrational branching has largely precluded laser-cooling of molecules and their use in quantum information, despite their highly desirable features [10, 79–86]. For precision measurement, the statistical sensitivity of molecule-based approaches (such as the ACME eEDM search [87, 88]) is limited by the fact that, due to vibrational branching to dark states, only a small fraction of the molecules in the experiment are detected during readout.

However, recently, a few molecules have been experimentally shown to have sufficiently closed optical cycling transitions to allow laser cooling [16, 22, 89–91]. These molecules are characterized by vibrational branching ratios that strongly favor decay to a small number of ground-state vibrational levels, meaning only a handful of lasers are required to achieve optical cycling. Almost all of these molecules consist of an alkaline-earth metal atom (M) ionically bonded to a molecular fragment in such a way that it optically behaves as a gas-phase M^+ cation radical. Calculations have revealed that complex M-O-R (*i.e.* alkaline-earth alkoxide) structures can be realized while retaining the ability to optically cycle [92–95]. However, the principles governing which ligands (R) will retain or even potentially promote optical cycling are not well understood and searches for acceptable species currently rely heavily on trial and error with expensive theory calculations for each candidate.

Building upon the M-O-R motif [93, 94], here we investigate functionalized phenyl rings for R and introduce a guiding principle by which the vibrational wavefunction overlap can be enhanced by straightforward chemical substitution within the molecular ligand. Using multireference wave functions and ground state and time-dependent density functional theory (TD-DFT) calculations, we investigate the Franck-Condon factors (FCFs, $q_{v',v''} \equiv |\langle v' | v'' \rangle|^2$, which typically approximate the vibrational branching ratio) of alkaline-earth phenoxides. We show that (i) electronic transitions in Ca and Sr phenoxides are promising for optical cycling (see also [94]) and (ii) electron-withdrawing substituents on the phenyl ring make the M-O bond more ionic via induction and resonance effects. This substitution suppresses the FCF-induced vibrational branching of spontaneous emission roughly in proportion to

the total electron withdrawing strength of the substituents. In particular, making three $H \rightarrow CF_3$ substitutions on the ring of calcium phenoxide, despite nearly doubling the number of atoms in the molecule, boosts the FCF limit on the expected number of spontaneously emitted photons from 22 to more than 500, a level relevant for laser cooling [16]. This technique should be applicable to a wide variety of molecules where the ionic character of the M-O bond in MOR can be manipulated from a distance via electron-withdrawing organic functional groups in R.

3.1.2 Computational Methods

Many previous theoretical studies of optical cycling in molecules have used complete active space self-consistent field (CASSCF) and multireference configuration interaction (MRCI) methods in order to produce highly accurate results [96–100]. However, these methods become prohibitively expensive when applied to large molecules. DFT and TD-DFT, on the other hand, can compuationally assess large species, but the accuracy of these methods for calculating vibrational branching is not well established. Hence, we first benchmarked DFT and TD-DFT (using Gaussian16) [101–105] against both CASMRCI calculations and experimental measurements for the smallest MOR molecules, finding good agreement for the PBE0 hybrid functional [106] with the D3 dispersion corrections [107], def2-TZVPPD basis set [108] and the double harmonic approximation with Duschinsky rotations for Franck-Condon factors [109]. While the accuracy of these methods for the large species considered below will remain an open question until they are tested by experiment (see Ch. 3.2), the FCFs we obtain from DFT and TD-DFT for the comparatively smaller alkaline-earth hydroxides (MOH) and metholixdes ($MOCH_3$) are within 2% of the experimentally measured branching ratios (see SI of Ref. [110] for details).

3.1.3 Results and Discussion

Using the techniques that produced the most accurate results for the smaller species, we first investigate the optical cycling properties of Ca- and Sr-phenoxide (*i.e.* a benzene molecule functionalized with an MO optical cycling center). Figure 3.1 shows electron iso-surfaces for the highest occupied molecular orbial (HOMO, analogous to the ground state wavefunction of the unpaired valence electron) and the first few lowest unoccupied molecular orbitals (LUMOs, the same for the excited states). In all cases shown, the electron density remains far from the molecular ligand, indicating that this valence electron plays very little role in the molecular bonds, a desirable property for suppressing vibrational branching. In further support of the promise of these species for optical cycling, the orbitals themselves qualitatively resemble hydridized versions of the s and p orbitals that constitute the optical cycling transition of the gas-phase atomic M^+ ion. Transitions between the HOMO and the LUMO and LUMO+1 correspond roughly to the $X\,^2\Sigma^+ \leftrightarrow A\,^2\Pi_{|\Omega|}$ fine structure doublet in the smaller, linear MOR species, while the LUMO+2 is analogous to the $B\,^2\Sigma^+$ state of those species. We label the electronic states as $\tilde{X}$, $\tilde{A}$, $\tilde{B}$ and $\tilde{C}$, in order of ascending energy.

To examine vibrational leakage from the optical cycle, we calculate the Franck-Condon factors (FCFs) for transitions from the vibrational ground state of the $\tilde{A}$ and $\tilde{C}$ electronic excited states to the electronic ground state in the Born-Oppenheimer approximation. Due to the lack of spectroscopic data and the difficulty of performing highly accurate calculations with large species (and since we will be interested in the *marginal* effect of the the chemical substitutions, discussed below), we use the calculated FCF as a proxy for the true spontaneous emission branching. We refer to $\eta_{0,0} \equiv \frac{q_{0,0}}{1-q_{0,0}}$ as the *Franck-Condon limit* of the expected number of spontaneously emitted photons before a leakage event when no vibrational repumping lasers are applied.

For the $\tilde{A} \rightarrow \tilde{X}$ transitions in both Ca- and Sr-phenoxide, we find that the FCFs are indeed highly diagonal, as expected [94], with $CaOC_6H_5$ capable of emitting an average of $\eta_{0,0} = 22$

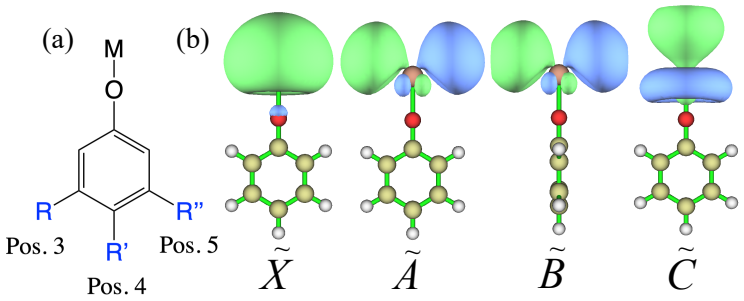

Figure 3.1: (a) Substitution positions investigated on the metal (Sr, Ca)-oxygen phenyl ring. (b) Global minimum structures and molecular orbitals (isosurface value of 0.03) for $SrOC_6H_5$ show the atom-like character of the electron distribution for the ground and first three excited states. The lack of electron density on the ligand suggests very little structural change will be involved in the electronic transitions.

photons before FCF-induced vibrational branching (we refer to the FCFs as "diagonal" if the Franck-Condon matrix **q** is approximately equal to the identity). We also find that the $\tilde{C} \rightarrow \tilde{X}$ transitions have even higher overlap, corresponding to both Ca- and Sr-phenoxide yielding $\eta_{0,0} > 150$ photons before FCF-induced vibrational branching. However, we find that vibronic coupling among the excited electronic states is likely to lead to perturbations that increase the vibrational branching ratios for $\tilde{B}$ and $\tilde{C}$ from those predicted by the unperturbed state analysis (see [111, 112] and SI of [110]) and we therefore focus below exclusively on the FCF-boosting effect of chemical substitution on $\tilde{A} \rightarrow \tilde{X}$, which is likely to be the most closed transition.

Fundamentally, the large values of $\eta_{0,0}$ attained by these species can be traced to the highly ionic nature of the M-O bond; the bonding electron of neutral M is pulled sufficiently far from the M^+ ion core that excitations of the remaining electron on the core do not perturb the bond. This suggests that if the electron withdrawing strength of the ligand can be increased, the FCF limit on the number of emitted photons would likewise increase [113]. However, if electron-withdrawing chemical groups are located too close to the metal atom, they pull on it and bend the bond, significantly degrading the diagonal FCFs. We therefore

require an approach that allows the placement of electron-withdrawing chemical groups far from the M atom while still retaining sufficient chemical intercourse with M to increase the ionicity of the M-O bond.

For this, we employ substituents at the 3, 4 and 5 positions of the phenyl ring that withdraw electrons via resonance and inductive effects and influence the M-O bond character without compromising its linearity. As a predictor of their expected influence on the M-O bond ionicity, we apply the concept of Hammett σ constants [114], dimensionless parameters that are empirically determined from ionization of organic acids in liquid and have been tabulated for many functional groups and substitution locations (see *e.g.* [115]). Despite the seeming conceptual disconnect between the chemistry of species in solution and optical cycling, we show that the Hammet σ constants effectively provide a guide for the effect of substituents on Franck-Condon overlap since they quantify the electron donating or withdrawing effect of each substitution. Roughly speaking, positive Hammett constants indicate electron withdrawing strength with negative constants indicating electron donation, so we therefore expect large, positive totals for the Hammett constants of the substituted functional groups to suppress FCF-induced vibrational branching.

Figure 3.2 and Table 3.1 show calculated vibrationless (*i.e.* from absolute vibrational ground state to absolute vibrational ground state) Franck Condon factors $q_{0,0}$ on $\tilde{\mathrm{A}} \rightarrow \tilde{\mathrm{X}}$ as a function of the total of the Hammett constants for a variety of functional groups added to the phenyl rings of Ca- and Sr-phenoxide. For this we chose to examine OH, Cl, F and CF_3 in all possible configurations of the 3, 4 and 5 positions, as well as several mixtures of these. The FCF-limited optical cycle closure shows a clear positive correlation with Hammett constant total as various substitutions are made that remotely impact the ionic nature of the M-O bond, in accordance with the principle described above. In particular, the substitution of three CF_3 groups for three hydrogens on the far side of the ring in $CaOC_6H_5$ increases $q_{0,0}$ from 0.958 to 0.998, a boost in the FCF-limit for the expected number of photons ($\eta_{0,0}$) by more than a factor of 20$\times$ compared to the unaltered variant.

Substituent for H in MOC_6H_5	Hammett Total $\sum\sigma$	CaOR $\tilde{A}\rightarrow\tilde{X}$ Ca-O change (Å)	FCF $q_{0,0}$	SrOR $\tilde{A}\rightarrow\tilde{X}$ Sr-O change (Å)	FCF $q_{0,0}$
4-OH	-0.37	0.01809	0.949	0.02077	0.922
3,4-OH	-0.25	0.01756	0.946	0.02045	0.920
3,4,5-OH	-0.13	0.01606	0.958	0.01938	0.931
(none)	0.00	0.01680	0.958	0.01996	0.933
4-F	0.06	0.01657	0.957	0.01961	0.931
3-OH	0.12	0.01622	0.960	0.01956	0.934
4-Cl	0.23	0.01552	0.962	0.01896	0.936
3,5-OH	0.24	0.01568	0.961	0.01919	0.935
3-F	0.34	0.01497	0.965	0.01855	0.941
3-Cl	0.37	0.01461	0.965	0.01832	0.940
3,4-F	0.40	0.01479	0.964	0.01826	0.938
3-CF_3	0.43	0.01376	0.967	0.01765	0.940
4-CF_3	0.54	0.01358	0.971	0.01767	0.942
3,4-Cl	0.60	0.01357	0.969	0.01754	0.941
3,5-F	0.67	0.01302	0.974	0.01707	0.949
3,4,5-F	0.74	0.01290	0.973	0.01686	0.948
3,5-Cl	0.74	0.01269	0.977	0.01662	0.950
3,5-CF_3	0.86	0.01022	0.983	0.01498	0.957
3,4,5-Cl	0.97	0.01159	0.979	0.01610	0.952
3,4-CF_3	0.97	0.01009	0.979	0.01296	0.970
3,5-CF_3-4-Cl	1.09	0.00927	0.986	0.01236	0.972
3,5-Cl-4-CF_3	1.29	0.00882	0.987	0.01231	0.973
3,4,5-CF_3	1.40	0.00290	0.998	0.01198	0.974

Table 3.1: Calculated changes in the M-O bond length (positive indicates bond lengthening upon emission) and Franck-Condon factors for the $\tilde{A}\rightarrow\tilde{X}$ transitions in M-phenoxide with various functional groups on the 3, 4 and 5 positions of the phenyl ring. The Hammett σ constants of each substituent are summed to indicate the additional electron withdrawing strength contributed by the substitution.

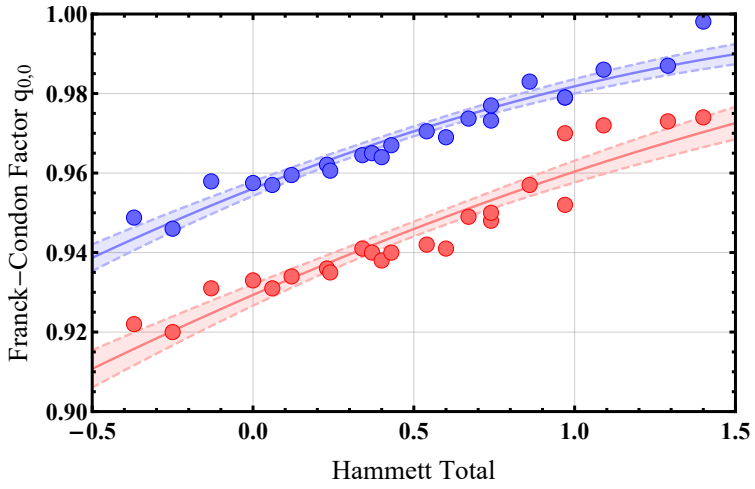

Figure 3.2: The calculated vibrationless $\tilde{A} \rightarrow \tilde{X}$ Franck-Condon factors for substituted MOC_6H_5 derivatives show a strong correlation with the total of the Hammett σ constants of their substituents. CaOR (SrOR) species are shown in blue (red). Solid curves are fits to Gaussians centered at the x-intercept of the bond length change vs. Hammett total trends (Table 3.1).

The effect of chemical substitution on vibrational branching in these species can be traced largely to their geometry. Table 3.1 shows that the length change of the M-O bond for the $\tilde{A} \rightarrow \tilde{X}$ transition is approximately linearly correlated with the Hammett total of the substituents. In all cases, the largest geometry change from ground to excited state was the M-O bond length. Extrapolation of the linear trend to zero bond length change can be used to build a simplified model for how the FCFs should depend upon the Hammett total. Since vibrational ground states are typically approximately Gaussian and the transition's bond length change is linear in the Hammett total, the vibrationless FCFs ($q_{0,0}$) will be Gaussian in Hammett total. The solid curves in Fig. 3.2 are Gaussian fits to the calculated points, which appear consistent with this model.

In all MOC_6H_5 derivatives, the $\tilde{A} \rightarrow \tilde{X}$ transition's off-diagonal FCFs were dominated by a normal mode strongly associated with stretching of M-O. Figure 3.3 shows the diagonal FCF (the fundamental transition) and the largest two off-diagonal FCFs, labeled with their associated normal modes for the unsubstituted and trifluoromethyl-substituted $SrOC_6H_5$ and

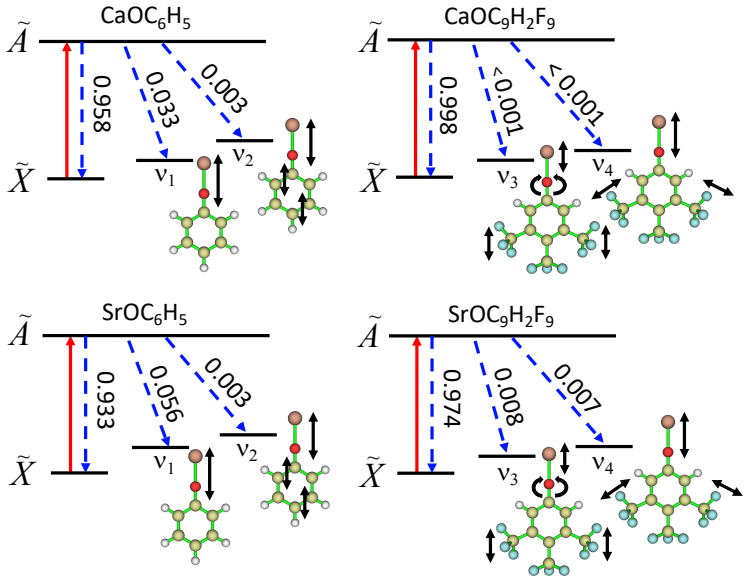

Figure 3.3: Photon cycling scheme with an excitation (red) to the first excited electronic state ($\tilde{\text{A}}$) and decay (blue) to the ground electronic state ($\tilde{\text{X}}$). The FCFs are shown along with each decay.

$CaOC_6H_5$. For both $SrOC_6H_5$ and $CaOC_6H_5$, the largest leakage pathways are normal modes with almost entirely M-O stretch character. As more electron-withdrawing susbstituents are added, this isolated stretch mode incorporates more and more bending behavior, until the largest electron-withdrawing group case, $MOC_9H_2F_9$, has a leakage pathway dominated by a vibrational mode with combined M-O stretching and bending character. In addition, analysis of second-order coupling to nearby vibronic levels predicts induced loss channels smaller than 10^{-3} on $\tilde{\text{A}} \rightarrow \tilde{\text{X}}$, suggesting that these FCFs can be used as a guide to investigate optical cycling in these species since they are all less than ≈ 0.999 (see SI of [110]).

The use of electron-withdrawing functional groups to boost the FCF of the optical cycling transitions in large molecules relies on two basic properties of the metal and ligand. First, the (possibly substituted) ligand's HOMO/LUMO gap must be large enough to fit the electronic excitation of the metal in the gap. For example, benzene and adamantane have a naturally large HOMO/LUMO gap which can easily append a metal with an unpaired electron such as Sr or Ca and can be decorated with electron-withdrawing substituents. The

new HOMO/LUMO gap for these M-O-R species becomes the metal to metal electronic transition, creating an isolated electronic transition. Second, it is important that electron-withdrawing substituents do not delocalize the optically active electron. For example, we find that if 4-NO_2 is substituted on the phenyl ring, it promotes delocalization through the π system of its molecular orbitals, unlike trifluoromethyl substituents and spreads the electronic wavefunction across NO_2 and the benzene ring. This reorders the unoccupied orbitals such that the new LUMO is the electron density delocalized on the benzene ligand instead of localized on the metal. This can also be seen as electron density mixing of metal and NO_2 in natural transition orbitals [110]. As a result, substituents that favor delocalized π bonds are poor candidates for FCF tuning.

3.1.4 Conclusions

Using chemical substitution to bolster optical cycling introduces a principle for informed design of species for quantum information and precision measurement applications. By using Hammett constants to choose electron-withdrawing substituents, it is possible to circumvent the expectation that increasing the number of vibrational modes (and therefore decay channels) will compromise optical cycle closure. Indeed, we have shown here that optical cycling can actually be improved by adding more complexity to certain ligands. This is possible when the size and aromatic properties of a ligand allow functional substitutions to alter the M-O bond character while being held far from the optical cycling center — a capability that only large molecules can provide. While we have focused here on a particular feature of some large molecules (aromaticity) that can promote optical cycling, the observation that new phenomena can emerge as complexity increases supports the claim that more aspects of polyatomic molecules are likely be identified in the future to allow increased quantum control of molecular species.

3.2 Experimental Realization of Tuning the FCF with Electronic Substitution

3.2.1 Introduction

Molecules and surfaces can be augmented with smaller molecules or groups that imbue a desired property to the system. Such functionalization can determine the system reactivity and properties, allowing a host of capabilities, such as catalysis [116, 117] and biological and chemical binding and sensing [118–121]. As the properties of the functional groups are often not strongly affected by the bonding to the host molecule, the technique can bring the same function to a wide-variety of systems.

It is interesting to consider extending the idea of a functional group to new operations. For example, can a robust qubit moiety be designed to act as a functional group attached to a larger molecule? Can multiple such *quantum functional groups* connect through space, allowing the host compound to serve as a bus for entanglement? And, relatedly, can a quantum functional group be used to control or witness the dynamics of a larger molecular whole?

Here, we shed light on these questions by demonstrating the key features of a quantum functional group, known as an optical cycling center (OCC). We experimentally show that a functional group, an alkaline-earth(I)-oxygen moiety, can be attached to a variety of aromatic compounds while retaining the property that it can scatter many photons without changing vibrational state. This property opens the door to using lasers to cool [33] external and internal degrees of freedom of large molecules by simply functionalizing them with an OCC. With this capability come the prerequisites for quantum information science with large molecules, namely mechanical control and qubit state preparation and readout.

The process for OCC functionalization can be understood intuitively by considering the neutral molecules that have previously been laser cooled. Much success has been had

with diatomic molecules composed of an alkaline-earth metal atom bonded to a halogen atom [21, 122]. In such molecules, the halogen atom withdraws an electron from the alkaline-earth atom, leaving one metal-centered radical electron whose highest-occupied and lowest-unoccupied molecular orbitals, HOMO and LUMO, respectively, do not strongly participate in the molecular bonding and closely resemble those of an alkali atom. The result is a molecule that can absorb and emit many photons without changing vibrational state [123].

More recently, this theme was demonstrated experimentally with an alkaline-earth metal atom bonded to -OH [17]. It was proposed that the same approach could be used for an entire class of alkaline metal-oxide-radical molecules, including complex polyatomic molecules [92] and later laser cooling was extended to the -OCH_3 ligand [25]. Like a halogen atom, all of these fragments withdraw an electron from the metal atom. This suggests that the alkaline-earth(I)-oxygen moiety can be considered as a functional group, akin to an alcohol or ether. Subsequent bonding of this functional group to electron-withdrawing ligands should therefore allow scattering of many photons without changing the vibrational state of the resulting molecule [94, 110, 113, 124].

To explore the limits of this concept, we studied the functionalization of aromatic compounds with an OCC. Specifically, we attached a Ca(I)−O unit to a phenyl group (-Ph) and its derivatives (-Ph-X, X = 3-CH_3, 3-F, 3-CF_3, 3,4-F_2 and 3,4,5-F_3, see Fig. 3.4(a)) and measured the vibronic spectra of the resulting molecules with dispersed laser-induced fluorescence (DLIF) spectroscopy. We found that the OCC transition frequency is linearly related to the acid dissociation constant (pK_a) of the precursor compound, providing a simple means for predicting molecular properties. Further, the vibrational branching ratios (VBRs) were determined and regardless of the choice of ligand it was found that $\gtrsim 90\%$ of the photon scattering events did not change the vibrational state of the molecule. Small variation in the VBR, at the few percent level, was observed and found to be consistent with a theoretical calculation suggesting that pK_a provides a simple guide for designing ligands with the best OCC performance [110]. From this work, we found that CaO-Ph-3,4,5-F_3 does

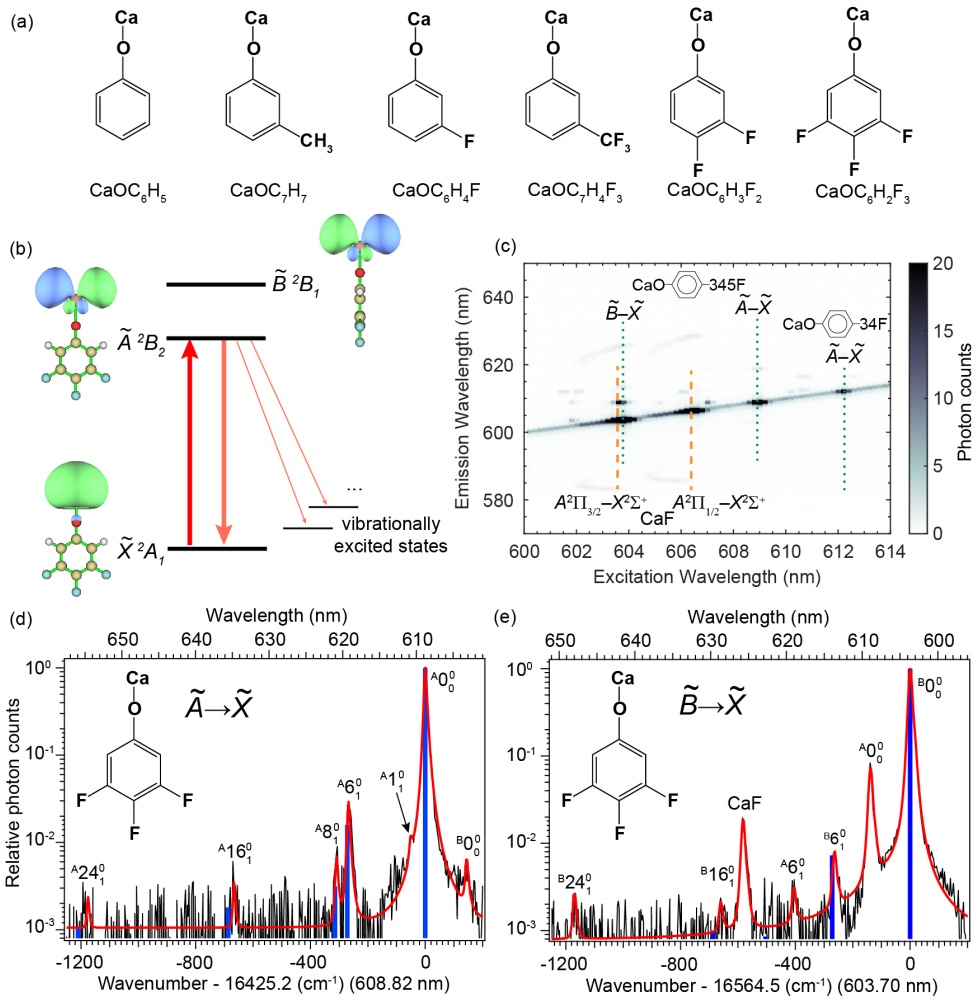

Figure 3.4: 2D and DLIF spectra of CaO-Ph-3,4,5-F_3. (a) Molecular structures of calcium phenoxide and derivatives. (b) Molecular orbital and schematic energy levels of CaO-Ph-3,4,5-F_3. All other molecules have similar orbitals and energy levels. (c) 2D excitation-DLIF spectrum following the reaction of Ca with 3,4,5-trifluorophenol. The orange dashed lines indicate the transition bands of CaF while green dotted lines indicate the transition bands of CaO-Ph-3,4,5-F_3 and CaO-Ph-3,4-F_2. (d) DLIF spectrum for the $\widetilde{A} \rightarrow \widetilde{X}$ decay of CaO-Ph-3,4,5-F_3 when exciting at 608.82 nm. (e) DLIF spectrum for the $\widetilde{B} \rightarrow \widetilde{X}$ decay of CaO-Ph-3,4,5-F_3 when exciting at 603.70 nm. In (d) and (e), the experimental spectra (black) are overlaid with a Pearson distribution fits (red, see Supplementary Information for further details). The blue vertical lines indicate the calculated frequencies of the vibrational modes and the height of the lines reflect their calculated relative strengths.

not change its vibrational state during roughly 99% of scattering events, implying that laser cooling is possible with current technology. In what follows, we describe the apparatus and experiments, present the recorded spectra and measured VBRs and discuss the next steps for decorating molecules and surfaces with quantum functional groups.

3.2.2 Experimental Methods

The molecules were produced by the reaction of Ca atoms with ligand precursors and cooled in a cryogenic He buffer-gas cell operated at ≈ 9 K [28]. A tunable, pulsed optical parametric oscillator (OPO) provided the excitation light and a monochromator augmented with an intensified charge-coupled device camera (ICCD) recorded the dispersed fluorescence (see Ref. [125] for further details).

3.2.3 Results and Discussion

Molecular species were first identified via 2D spectroscopy, performed by scanning the OPO frequency and recording the DLIF. Transitions between the ground ($\widetilde{X}\,^2A_1$) and two lowest-energy electronic states ($\widetilde{A}\,^2B_2$ and $\widetilde{B}\,^2B_1$) were predicted to have potential for laser-cooling (Fig. 3.4(b)) due to the localization of the molecular orbitals on the Ca atom. Example data is shown in Fig. 3.4(c) for CaO-Ph-3,4,5-F_3, while the 2D spectra of all other molecules observed are shown in Extended Fig. 1 of Ref. [125]. Four strong spectral features were observed. The excitation to the $\widetilde{B}$ electronic state of CaO-Ph-3,4,5-F_3 is indicated by the green dotted line near 603.5 nm, while the excitation to the $\widetilde{A}$ electronic state is at 608.5 nm. The two broad bands near 603.5 nm and 606.5 nm, marked by dashed orange lines, are attributed to the $v' = 0 - v'' = 0$ bands of the $A\,^2\Pi_{3/2} \leftarrow X\,^2\Sigma^+$ and $A\,^2\Pi_{1/2} \leftarrow X\,^2\Sigma^+$ transitions, respectively, of CaF, which is also formed when Ca reacts with a fluorinated phenol. A weaker feature at 612.0 nm is due to the $\widetilde{A} - \widetilde{X}$ transition of CaO-Ph-3,4-F_2, which is a by-product of the reaction between Ca and 3,4,5-trifluorophenol. Assignments

were made by comparing observed and calculated vibrational frequencies (see SI Table 1 in Ref. [125]), as discussed further later.

Having identified the molecules, DLIF measurements were recorded by tuning the OPO to a selected resonance and accumulating between 4000-8000 ICCD exposures. Representative DLIF spectra for CaO-Ph-3,4,5-F_3 are shown in Fig. 3.4(d-e). All spectra are plotted in terms of the energy difference (in cm^{-1}) relative to the excitation energy and are normalized to the peak at the origin. The measured peak widths (full width at half maximum) are $\approx$ 0.5 nm and mainly due to the spectrometer resolution ($\approx$ 0.5 nm) and the rotational distribution on decay ($\approx$ 0.1 nm). Fig. 3.4(d) shows the DLIF spectrum of CaO-Ph-3,4,5-F_3 when exciting the $\widetilde{A} \leftarrow \widetilde{X}$ transition at 608.82 nm. The peak, labeled as ${}^{A}0_0^0$, represents the decay from the excited $\widetilde{A}(v' = 0)$ state to the ground $\widetilde{X}(v'' = 0)$ state. The strongest vibration-changing decay, observed at -267 cm^{-1} and labeled ${}^{A}6_1^0$, is assigned to the Ca$-$O and ring stretching mode of the $\widetilde{X}$ state with a predicted harmonic frequency of 272 cm^{-1} (Fig. 3.5(a)). Similarly, peaks at -309 cm^{-1} and -666 cm^{-1} can be assigned to 8_1^0 and 16_1^0, respectively, which are both symmetric stretching modes involving the benzene ring (Fig. 3.5(a)). A weak decay at -1175 cm^{-1} is attributed to the high-frequency stretching mode 24_1^0 (Fig. 3.5(a)). The small shoulder next to the diagonal peak is due to decays to the lowest-frequency fundamental bending mode, 1_1^0. The vertical blue lines are the calculated VBRs normalized by the predicted value for the 0-0 decay. Interestingly, as noted by the absence of a predicted VBR for the 1_1^0 peak, theoretical calculations predict this decay pathway to be negligible. The observed strength of this decay is likely due to vibronic couplings among and anharmonicities within the low-frequency modes [110, 126, 127] not considered in the present calculation.

The DLIF spectrum of CaO-Ph-3,4,5-F_3 from the $\widetilde{B}$ state is shown in Fig. 3.4. In addition to the non-vibration-changing decay ${}^{B}0_0^0$ and the dominant vibration-changing decay ${}^{B}6_1^0$, decays are observed with shifts of -139 cm^{-1} and -407 cm^{-1}. These peaks are due to emissions from $\widetilde{A}(v' = 0)$, which is presumably populated by collisional relaxation in the

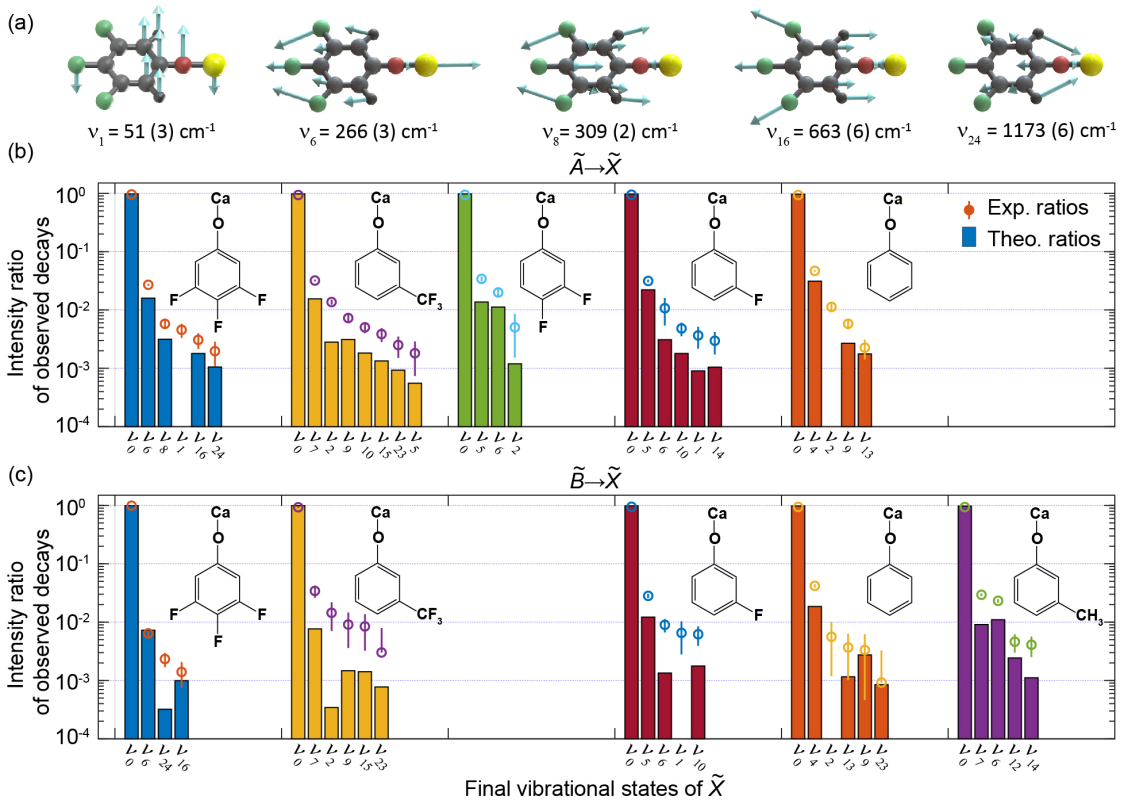

Figure 3.5: Vibrational decay ratios for all observed modes. (a) The observed vibrational modes of CaO-Ph-3,4,5-F_3 with an experimentally determined and theoretical frequencies listed. The Arrows indicate the direction of vibrational displacements. (b and c) Intensity ratio of observed decays, relative to total observed decays, for $\widetilde{A} \rightarrow \widetilde{X}$ and $\widetilde{B} \rightarrow \widetilde{X}$ transitions, respectively, for all molecules and modes studied in this work, arranged in order of increasing pK_a. Experimental values are denoted with circles while calculated values are depicted as bars for clarity. Error bars (s.d.) are statistical standard errors. The vibrational mode denoted as v_I indicates the decay to the final vibrational state of I_1^0. The $\widetilde{A} \rightarrow \widetilde{X}$ decay of CaO-Ph-3-CH_3 and $\widetilde{B} \rightarrow \widetilde{X}$ decay of CaO-Ph-3,4-F_2 are omitted due to coincidences with CaOH and CaF decays, respectively. The values are summarized in Table S3 of [125]

buffer gas [128, 129]. Interestingly, we also see evidence of collision-induced excitation when exciting to the $A^2\Pi_{1/2}$ state; as seen in Fig. 3.4(d), a small peak at a positive shift of 140 cm^{-1} can be assigned to the ${}^B0_0^0$ decay. This excitation process is presumably due to collisions with

hot reaction products before they are thermalized by the buffer gas. Lastly, a weak peak at -1172 cm^{-1} is attributed to the stretching mode 24_1^0, while the strong peak at -584 cm^{-1} is assigned to CaF $A^2\Pi_{3/2}(v'=0) \rightarrow X^2\Sigma^+(v''=1)$ decay. The comparison of experimental and theoretical frequencies of all observed modes is summarized in Table S2 of [125].

As seen in the relative heights of the ${}^A0_0^0$ and ${}^B0_0^0$ peaks in Figs. 3.4(d-e), both $\widetilde{A}-\widetilde{X}$ and $\widetilde{B}-\widetilde{X}$ transitions are promising for optical cycling as vibrational-state-preserving decays are strongly favored. Because vibration-changing decays below the measurement sensitivity ($\sim\ 1\times\ 10^{-3}$) or obscured by other peaks may not have been observed, the ratio of the intensities of these peaks is not strictly a VBR (see SI in Ref. [125]). Therefore, to compare to theoretical calculations we plot the ratio of intensities of only the observed peaks in Figs. 3.5(b-c). In general, Figs. 3.5(b-c) show reasonable agreement between experiment and theory, other than the aforementioned underestimate of the decay to low-frequency bending modes (v_1 or v_2). The theoretical and observed values of the vibrational decay ratios of all observed modes are given in Table S3 of [125].

To explore the effect of the ligand on the OCC, Fig. 3.6 plots the measured transition energies and estimated 0_0^0 VBRs as a function of the precursor pK_a in solution. The pK_a is a convenient parameter that indicates the strength of an acid R$-$OH and therefore quantifies the electron-withdrawing capability of the R$-$O$^-$ ligand. A smaller pK_a implies a more ionic Ca(I)$-$O bond in R$-$O$-$Ca. A similar metric to pK_a, shown on a second horizontal axis, is the Hammett parameter total [114], which has been used in previous theoretical work [110] and varies monotonically with the pK_a (Table S5 in [125]). As can be seen in Fig. 3.6(a), the excitation energies follow a monotonic and apparently linear trend with pK_a. This behavior is qualitatively understood as an increase in HOMO-LUMO gap as the electron-withdrawing strength of the ligand increases [130], yielding more localized molecular orbitals on the Ca atom (Fig. 3.4(b)) with a trend toward the atomic Ca$^+$ ion. The calculated $\widetilde{A}-\widetilde{B}$ energy differences are systematically smaller than the experimental values by ≈ 5 meV, likely a result of the omission of spin-orbit coupling from the theoretical calculation [131].

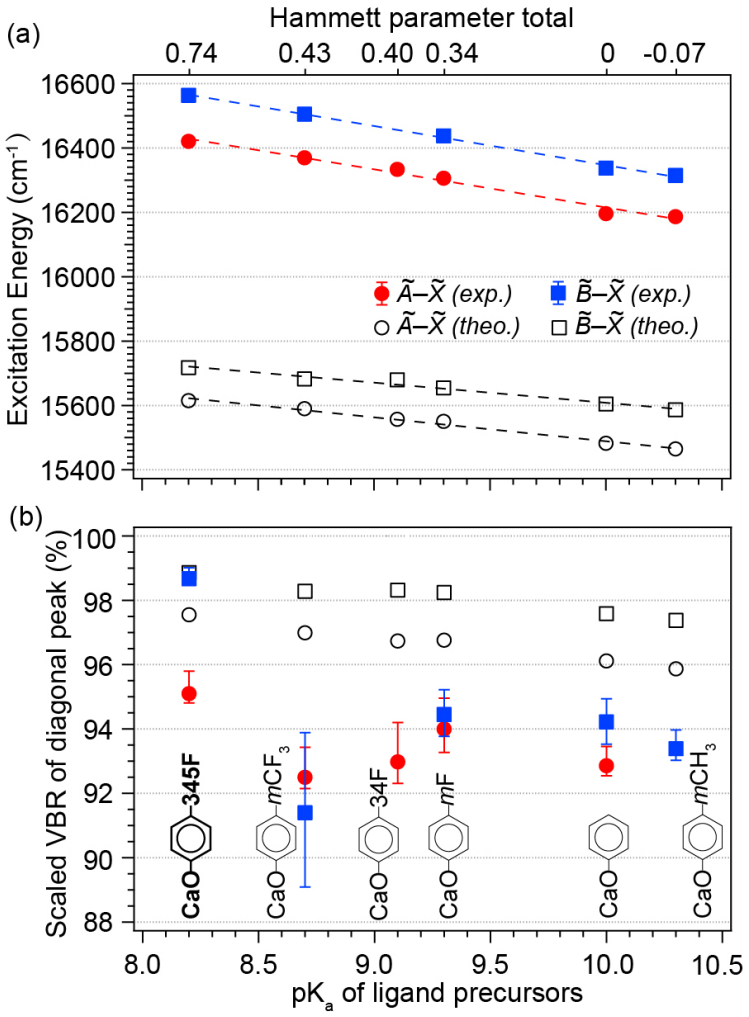

Figure 3.6: pK_a trends. (a) $\widetilde{A} - \widetilde{X}$ and $\widetilde{B} - \widetilde{X}$ transition energies versus pK_a for all molecular species studied here. The linear fits to the experimental data yield $E_{\widetilde{A}} = 17,400 - 118.0 \times pK_a$ (cm^{-1}) and $E_{\widetilde{B}} = 17,561 - 121.5 \times pK_a$ (cm^{-1}). (b) Scaled VBR for diagonal decay as a function of pK_a. The large error bar for $\widetilde{B} \rightarrow \widetilde{X}$ decay of CaO-Ph-3-CF_3 is due to a partial spectral overlap with CaF. The pK_a and Hammett parameter can be linked by the derived Hammett equation (see Table S5 of [125]).

Figure 3.6(b) shows the estimated 0_0^0 VBRs as a function of pK_a. The 0_0^0 VBR for each transition is estimated by normalizing the observed 0_0^0 decay signal by the signal of all observed transitions plus an estimated contribution of the unobserved peaks. The error bars

on each point represent the combination of the statistical standard error and the uncertainty from the unobserved peaks. Systematic errors, discussed in Methods and Supplementary Information of [125], are expected to be smaller than a few percent.

Remarkably, across all six ligands and a considerable range of pK_a, the VBRs are relatively unchanged and always $\gtrsim$ 90 %, indicating that the OCC function can indeed be made orthogonal to the ligand molecule. The theoretical calculations in Fig. 3.6(b) show an increase in VBR for stronger acids, as previously predicted [110]. This trend is consistent with the experimental data and is understood as the localization of the electronic wavefunction on the Ca atom with a more ionic Ca(I)−O bond, leading to further isolation of the electronic and vibrational degrees of freedom [110]. This suggests that while an OCC can be successfully attached to a wide range of molecules, performance may still be optimized by choosing ligands with strong electron-withdrawing character. Deviation from this trend likely occurs in CaO-Ph-3-CF_3. Here, the lower symmetry and large electron inductive effect may lead to larger vibronic mixing between the $\widetilde{A}$ and $\widetilde{B}$ excited states, which can increase vibration-changing decay. Our level of theory cannot capture this mixing and therefore would underestimate the effect.

Together, these features illustrate that a quantum functional group, furnishing a means for gaining full quantum control of a wide range of molecules, should be possible. As an example, from the recorded structure and measured state lifetimes (Supplementary Fig. 1), we estimate a magneto-optical trap of CaO-Ph-3,4,5-F_3 is possible using the $\widetilde{B}-\widetilde{X}$ transition with six to eight lasers [95]. Interestingly, this is similar to the number of lasers required in molecules with roughly an order of magnitude fewer vibrational modes [112]. Further, using the same laser system, single quantum states can be prepared via optical pumping and measured by state-resolved fluorescence with high fidelity.

The ability to laser cool and prepare single quantum states of such 'large' molecules opens the door to a host of new science. The rich structures of these molecules allow robust encoding of quantum information [6] and provides new platforms for precision measurement and tests

of fundamental physics [91, 132] as well as quantum simulation and computing [10, 83]. Ultracold organic hydrocarbons can be produced via zero-energy photofragementation [133] of those complexes and offer new opportunities for ultracold chemical reactions and collision studies [134]. Further, theoretical work suggests that the scheme demonstrated here can be continued to even larger molecules [124] and extended to surfaces [135].

3.2.4 Conclusions

In summary, we have functionalized six precursor compounds (phenol, *m*-cresol, 3-fluorophenol, 3-(trifluoromethyl)phenol, 3,4,-bifluorophenol and 3,4,5-trifluorophenol) with an optical-cycling center composed of a Ca(I)−O functional group. The resulting molecules were studied at cryogenic temperature via 2D and dispersed fluorescence spectroscopy. The excitation energies of the molecules showed a linear correlation with the pK_a of the organic precursors, providing a convenient way of discovering new molecules. Meanwhile, the vibrational branching ratios were largely unaffected by the choice of ligand and at a level sufficient for laser cooling and trapping as well as quantum state preparation and measurement. This demonstration of the orthogonality of the OCC function to the ligand function lays the ground work for functionalizing molecules with quantum functional groups and establishes principles of chemical design that can be used to build molecules of increasing size, complexity and function for quantum science and technology.

3.3 The Role of Fermi Resonance in Developing an Optical Cycling Center

3.3.1 Introduction

Functionalizing large molecules with optical cycling centers (OCCs) is being explored as a means for extending the exquisite control available in quantum information science to the chemical domain.[92–95, 110, 113, 123–125, 136–141] Success requires that these OCCs absorb and emit many photons without changing vibrational states. To accomplish this task, molecular design rules are being developed, aided and validated by experiments, to guide the creation of the ideal quantum functional groups [125, 142–144]. For example, prior work has demonstrated that alkaline-earth alkoxides provide a general and versatile chemical moiety for optical cycling applications, as the alkaline-earth radical electron can be excited without perturbing the vibrational structure of the molecule [125, 137, 138, 142, 143]. Similarly, traditional physical organic principles, such as electron-withdrawing, have been shown to improve OCCs performance [110, 125]. Further, experimental and theoretical extensions to more complex acenes [124, 142], diamondoids [139] and even surfaces [135] suggest an exciting path forward for creating increasingly complex and functional quantum systems.

However, an open question for this work is: what role intramolecular vibrational energy redistribution (IVR) will play as the molecule size is further increased [145–147]? In the typical description of IVR, the normal modes of molecular vibrations are treated within the harmonic approximation, while any anharmonic couplings between these modes are treated as a perturbation. Laser excitation to an excited (harmonic) vibrational state is then followed by the redistribution of the vibrational energy driven by the anharmonic couplings. This outflow of energy from one vibrational mode to other modes arises from the selection of basis states that are not eigenstates of the molecular Hamiltonian and thus not stationary.

An alternate and equivalent, description of IVR takes the vibrational eigenstates of the

molecular Hamiltonian as the basis. These basis states are mixtures of the harmonic vibrational modes, with amplitudes set by the anharmonic couplings. As these states are eigenstates of the molecular Hamiltonian they are, of course, not time-evolving (except for their coupling to the electromagnetic vacuum) and therefore there is no energy redistribution between them unless perturbed by an external field or collision. Instead, the effect of IVR in this picture is simply that there is more than one vibronic state within the spectrum of the exciting laser leading to non-exponential fluorescence as decay from these nearby states interfere.

This latter picture is convenient for understanding the role that IVR will play in functionalizing large molecules with OCCs. If harmonic vibrational states are close together and possess the correct symmetry, then anharmonic couplings will mix them. In this case, a harmonic vibrational state that is initially not optically active becomes optically active by mixing with an optically active harmonic mode. While this does not change the fraction of diagonal decays ($\Delta v = 0$, where v is the number of quanta in a vibrational mode), it does change the number of accessible final vibrational states and requires more repumping lasers to achieve optical cycling [15, 148, 149].

Therefore, to push optical cycling to larger and larger molecules it is desirable to develop molecular design principles for avoiding these vibrational couplings by energy separation and/or symmetry. Here, we explore these phenomena in both the calcium and strontium phenoxides, which have recently been shown as promising candidates for optical cycling [125, 143, 150]. We show that in certain derivatives of these molecules it is possible to find combination modes (within the harmonic approximation), which are not themselves optically active, close to optically-active stretching modes. Anharmonic coupling between these modes – *e.g.* Fermi resonance [151, 152], which is the simplest instance of IVR – leads to intensity borrowing and the activation of the combination mode so that a new decay pathway is opened. Such molecules will require extra repumping lasers for optical cycling. By comparing phenoxides with and without this effect, we present further design rules for functionalizing

ever larger molecules with optical cycling centers.

3.3.2 Computational Methods

All calculations were performed at the PBE0-D3/def2-TZVPPD level of theory [106–108, 153] with a superfine grid in Gaussian16 [101]. Optimized geometries, vertical excitation energies and frequencies were calculated with density functional theory (DFT)/time-dependent DFT (TD-DFT) methods. Harmonic Franck Condon factors (FCFs) were obtained using the harmonic approximation with Duschinsky rotations up to three quanta in ezFCF [109]. Anharmonic frequencies and anharmonic-corrected FCFs were calculated with vibrational perturbation theory (VPT) [154, 155] using $PyVPT_n$ [156, 157].

As seen in this work, anaharmonic coupling that leads to intensity-borrowing is missed by the harmonic approximation. To predict Fermi resonances and anharmonic-corrected FCFs, we use the numerical, matrix-form VPT as implemented in $PyVPT_n$ with the full $3N-6$ mode basis. Gaussian16 was used to obtain the quartic expansion of the normal mode potentials by evaluating the first and second derivatives of the Hessian at the PBE0-D3/def2-TZVPPD level of theory. A wavefunction threshold of 0.3 and energy threshold of 500 cm^{-1} was used for identifying degenerate subspaces, based on past investigations of these thresholds [158].

Since VPT coupling matrices are sensitive to small changes in the diagonal energies and diagonal energies are based on the quality of the original Hamiltonian initial inputs of harmonic frequencies and quartic expansions, some frequencies were shifted up to 7 cm^{-1} based on experimental evidence, as done in past work [159, 160]. For CaOPh, the $2v_4$ diagonal perturbed anharmonic frequency was shifted $2v_4 + 6.8$ cm^{-1}. This shift is incorporated in the resulting coupling matrices (see SI in Ref. [161]), whose diagonalized matrices gave the corrected frequencies and coefficients used for anharmonic FCFs. For CaOPh-3-F, the original harmonic v_6 was shifted by $v_6 - 2$ cm^{-1}, but no deperturbed anharmonic frequencies were shifted. For all other molecules, no shifts were made.

To incorporate intensity borrowing effects and include anharmonic effects into our predicted vibrational branching ratios, we adopt the same method used in Ref. [160] to include anharmonic corrections based on harmonic FCFs.

Anharmonic vibrational eigenstates are given by:

$$|\chi''\rangle = \sum_j c''_j \, |\Phi''_j\rangle \tag{3.1}$$

where c''_j are the eigenstates from the diagonalized VPT coupling matrices (see Table in SI) and $|\Phi''_j\rangle$ represents the zeroth-order state basis used in VPT.

Anharmonic FCFs are calculated as a transition form some initial state, j, to final state, k, as:

$$|\,\langle\chi'|\chi''\rangle\,|^2 = |\sum_{j,k} c'_k c''_j \,\langle\Phi'_k|\Phi''_j\rangle\,|^2 \tag{3.2}$$

We approximate the zeroth-order wavefunctions used in VPT are approximately the harmonic normal mode wavefunctions, $|\Phi\rangle \approx |\Phi_h\rangle$. This is expected to be a good approximation because $|\Phi\rangle$ are from the deperturbed VPT calculations, which makes other state contributions small compared to the leading term in the expansion. The matrix is then diagonalized to get obtain full state mixing contributions which are incorporated via the mixing coefficients, $|c|^2$. This gives the revised equation, below:

$$|\,\langle\chi'|\chi''\rangle\,|^2 = |\sum_{j,k} c'_k c''_j \,\langle\Phi'_{h,k}|\Phi''_{h,j}\rangle\,|^2 \tag{3.3}$$

Since our excited-state molecule is at its vibrational ground state, we can approximate the initial state as one eigenstate, $|\chi''\rangle \approx |\Phi''_{h,j}\rangle$, so that the FC factor arising from the zeroth-order excited state only involves a single overlap integral between two harmonic states, which is computed analytically in ezFCF:

$$|\sum_j c''_j \,\langle\Phi'_k|\Phi''_j\rangle\,|^2 = |\,\langle\Phi'_k|\Phi''_j\rangle\,|^2 \tag{3.4}$$

Using these approximations, anharmonic-corrected FCFs, which we report in Table S3 of [161], are built using harmonic wavefunctions ($|\phi_h\rangle$) as a basis and mixing coefficients (c'_k)

obtained from VPT, using the final equation below:

$$|\langle\chi'|\chi''\rangle|^2 \approx |c'_k|^2 |\langle\Phi'_{h,k}|\Phi''_{h,j}\rangle|^2 \tag{3.5}$$

3.3.3 Experimental Methods

A series of calcium and strontium phenoxides (CaOPh, CaOPh-3-F, CaOPh-4-F, CaOPh-3,4,5-F_3, SrOPh and SrOPh-3,4,5-F_3, Ph = phenyl group, Fig. 3.7a) were produced via laser ablation of the alkaline-earth metal into a mixture of the precursor ligand and Ne buffer gas inside a cryogenic cell operated at a temperature of ∼20 K (Fig. S1) [143]. As sketched in Figs. 3.7b-c, the vibrational structure of these molecules was probed with two types of measurements: dispersed laser-induced fluorescence (DLIF) spectroscopy, which probes the vibrational structure in the electronic ground state ($\widetilde{X}$) and excitation spectroscopy, which examines the vibrational structure in the excited states ($\widetilde{A}$ and $\widetilde{B}$). In DLIF spectroscopy (Fig. 3.7b), vibrationally cold molecules are excited to the ground vibrational level of the electronically excited $\widetilde{A}$ and $\widetilde{B}$ states, $\widetilde{A}/\widetilde{B}(v' = 0) \leftarrow \widetilde{X}(v'' = 0)$ and the resulting fluorescence is recorded as a function of wavelength. In excitation spectroscopy (Fig. 3.7c), the exciting laser is tuned to drive excitation to excited vibrational levels of the excited $\widetilde{A}$ and $\widetilde{B}$ states, $\widetilde{A}/\widetilde{B}(v'_n) \leftarrow \widetilde{X}(v'' = 0)$, while simultaneously monitoring the resulting fluorescence from diagonal decays. In both cases, excitation is provided via a tunable pulsed dye laser and the resulting fluorescence is coupled into a grating monochromator and detected using a photomultiplier tube. Compared to previous measurements [125, 143], improvements, such as better source handling techniques to reduce the production of alkaline-earth oxide contaminants, provided an increase in signal-to-noise ratio (SNR) of ∼3×. This improved SNR enabled spectrometer measurements with a higher resolution of 0.20 nm. Additional experimental details and theoretical methods are provided in the Supporting Information of Ref. [161].

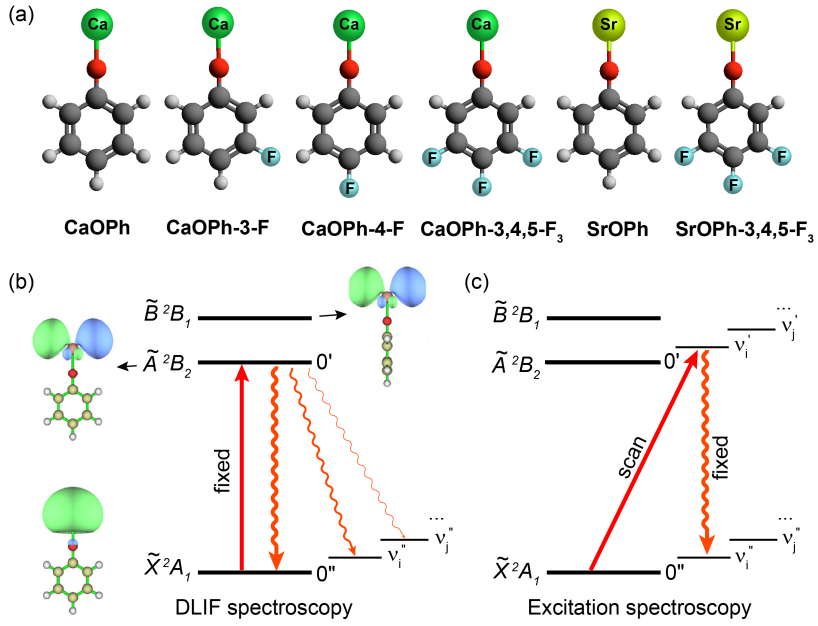

Figure 3.7: (a) Molecular structures of all studied calcium and strontium phenoxide and derivatives. (b) and (c) Schematic diagrams illustrating the DLIF measurement and excitation spectroscopy performed for all molecules in this study, respectively. DLIF measurements were done by fixing the laser wavelength at the transitions of $\widetilde{A}/\widetilde{B}(v' = 0) \leftarrow \widetilde{X}(v'' = 0)$ and detecting the dispersed fluorescence. Excitation spectroscopy was carried out with off-diagonal excitation scan, $\widetilde{A}/\widetilde{B}(v'_n) \leftarrow \widetilde{X}(v'' = 0)$ and diagonal fluorescence detection $\widetilde{A}/\widetilde{B}(v'_n) \rightarrow \widetilde{X}(v''_n)$. The molecular orbital and symmetries of the electronic states are based on the CaOPh molecule with a C_{2v} symmetry.

3.3.4 Results and Discussion

Using the improved resolution explained above, we recorded DLIF spectra for the $\widetilde{A} \rightarrow \widetilde{X}$ and $\widetilde{B} \rightarrow \widetilde{X}$ transitions of CaOPh, shown as the red lines in Figs. 3.8a and 3.8b, respectively. For comparison, the previously recorded DLIF spectra for this molecule [125] are shown as black lines. Several improvements are immediately clear. First, spectral contamination by CaOH molecules, features denoted by *, is greatly reduced. Second, while in the previous work three fundamental vibrational modes (v_2, v_4 and v_9) were resolved within the frequency range of $\sim$660 cm^{-1} below the respective 0-0 transition, the improved measurements here

reveal several new features which were either unresolved in or below the detection limit of the previous measurement. Specifically, the lowest-frequency out-of-plane bending mode v_2 (Fig. 3.8d) is much better resolved at a frequency shift of -60 cm^{-1} (Figs. 3.8a-b). A new weak decay is also observed at -241 cm^{-1} (Fig. 3.8b) and readily assigned to the fundamental out-of-plane bending mode v_3 (Fig. 3.8d).

Further, the previously assigned peaks due to decay to the Ca-O stretching modes v_4 and v_9 are seen to be doublets. While theoretical calculations within the harmonic approximation predict v_4 should be the strongest off-diagonal decay ($\Delta v \neq 0$) and occur at -313.6 cm^{-1} (Table S3 in [161]), the weaker peak at -295 cm^{-1} is not readily assignable. Compared with the theoretical harmonic vibrational frequencies, the weak peak is near the combination modes $v_1 + v_3$ and $v_2 + v_3$, as shown in Fig. 3.8d, however, the predicted Franck-Condon factors (FCFs) for these decays are $< 10^{-4}$, well below the current detection limit. The observed decay can be explained by an intensity borrowing mechanism [162, 163], which arises from anharmonic coupling between the nearly degenerate stretching mode v_4 and the combination mode consisting of two bending modes, also known as a Fermi resonance [146, 151, 152]. To corroborate Fermi resonance doublets, vibrational perturbation theory (VPT) with resonances was applied on top of anharmonic frequency calculations to predict corrected frequencies, resonance doublets and obtain anharmonic FCFs (see Computational Methods for more details). As seen in the insets of Figs. 3.8a-b, the predicted separations (vertical blue lines) agree well with the observed vibrational doublets (red traces).

Given the requirement that coupled vibrational modes have the same symmetry, the weaker peak is attributed to the combination mode $v_2 + v_3$ with A_1 symmetry, rather than $v_1 + v_3$ with A_2 symmetry (Fig. 3.8d). Similarly, the doublet near v_9 is interpreted as a result of vibrational decays to a fundamental mode v_9, as observed previously [125] and the overtone of the stretching mode v_4. In the harmonic approximation, the decay intensity of v_9 is relatively consistent between $\widetilde{A} \rightarrow \widetilde{X}$ and $\widetilde{B} \rightarrow \widetilde{X}$ transitions, whereas $2v_4$ exhibits significant variation. The decay from $\widetilde{A}$ gives a higher intensity for $2v_4$, attributed to a larger

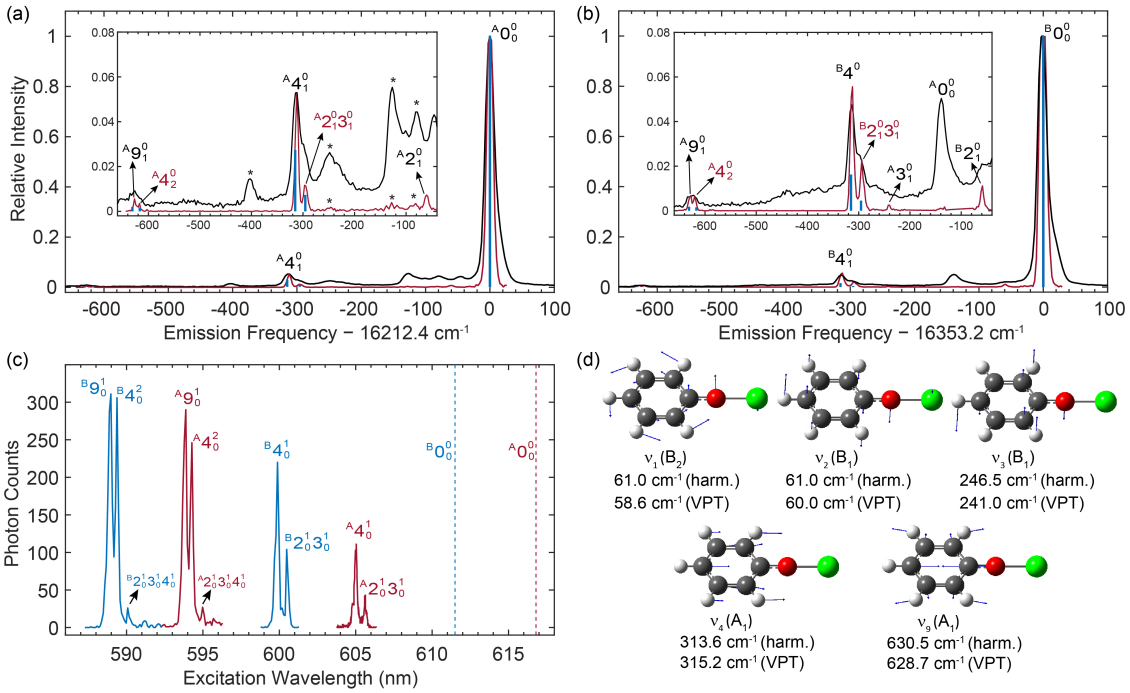

Figure 3.8: (a) and (b) Dispersed fluorescence spectra obtained for the $\widetilde{A} \rightarrow \widetilde{X}$ and $\widetilde{B} \rightarrow \widetilde{X}$ transitions of CaOPh. The black traces, adopted from previous work[125], were obtained with a spectral resolution of ≈ 0.5 nm. The red traces come from an improved measurement with resolution of ≈ 0.20 nm. The insets display the weak peaks in the range of -660 cm^{-1} to -40 cm^{-1} and show the presence of doublet peaks around -300 cm^{-1} and -630 cm^{-1}. The blue sticks depict the calculated frequencies and relative strengths (FCFs) of the vibrational modes using the VPT method. The symbol * indicates CaOH contamination. (c) Excitation spectrum of the $\widetilde{A}(v_n') \leftarrow \widetilde{X}(v'' = 0)$ (red traces) and $\widetilde{B}(v_n') \leftarrow \widetilde{X}(v'' = 0)$ (blue traces) transitions. The resulting fluorescence is monitored on diagonal decays. The two dashed lines indicate the excitation wavelengths corresponding to the respective 0-0 transitions. The assignments of all observed vibrational resonances are given. (d) Vibrational displacements of five related fundamental modes. The symmetries and theoretical frequencies in $\widetilde{X}$ using harmonic and VPT methods are provided. All vibrational modes are labeled with increasing frequency regardless of their symmetries.

overlap of vibrational displacement of v_4 with the in-plane orbital of the $\widetilde{A}$ state (Fig. 3.7b). Consequently, this results in an intensity ratio of $v_9/2v_4$ being four times in the $\widetilde{A} \rightarrow \widetilde{X}$ and

ten times in the $\widetilde{B} \rightarrow \widetilde{X}$ transition. The observed nearly equal intensities in both transitions in Figs. 3.8a-b are due to the intensity borrowing via Fermi resonance.

The presence of vibrational doublets due to anharmonic couplings is also observed in the electronically excited $\widetilde{A}$ and $\widetilde{B}$ states by excitation spectroscopy, as presented in Fig. 3.8c. Here, it is seen that for both electronically excited states, as in the ground state, the Fermi resonance leads to activation of the combination mode $v_2 + v_3$ at a spacing of around 16 cm^{-1} from the v_4 vibrational level (Table S5 in [161]). Similarly, excitations to the excited vibrational levels of v_9 and $2v_4$, as well as a very weak resonance to the combination band of $v_2 + v_3 + v_4$, are observed. The observation of the vibrational anharmonic coupling across different electronic states highlights the significance of Fermi resonances in the spectral characteristics of large molecules like CaOPh.

To explore the universality of Fermi resonances, we extended our study to the substituted molecules CaOPh-4-F, CaOPh-3-F and CaOPh-3,4,5-F_3. In Fig. 3.9, the DLIF spectra of the $\widetilde{A} \rightarrow \widetilde{X}$ and $\widetilde{B} \rightarrow \widetilde{X}$ transitions for these substituted molecules are presented. Remarkably, with a single fluorine atom substituted at the *para*-position of the phenyl ring, the DLIF spectra of CaOPh-4F (Figs. 3.9a-b) show only a single peak for the vibrational decay to the stretching mode v_4 for both transitions. This implies the absence of a Fermi resonance, which can be attributed to the substantial frequency spacing of 64 cm^{-1} (harm.) or 69 cm^{-1} (VPT) between v_4 and the symmetry-allowed combination band of $v_1 + v_3$ (Fig. 3.9e). Furthermore, the insets in Figs. 3.9a-b reveal two weak peaks at frequencies of around -53 cm^{-1} and -346 cm^{-1}, which can be assigned to mode v_2 and $v_2 + v_4$, respectively, by comparing with theoretical frequencies (Fig. 3.9e). These weak peaks are likely due to the anharmonic mode-coupling involving the low-frequency bending mode v_2 [125]. Additionally, the complex peaks observed at around -150 cm^{-1} result from collision-induced relaxation from $\widetilde{B} \rightarrow \widetilde{A}$, followed by fluorescence decay to the $\widetilde{X}$ state and a vibrational decay to mode v_3 at -170 cm^{-1}.

In the case of CaOPh-3-F, where the *para*-F is replaced with a *meta*-F and the molecular

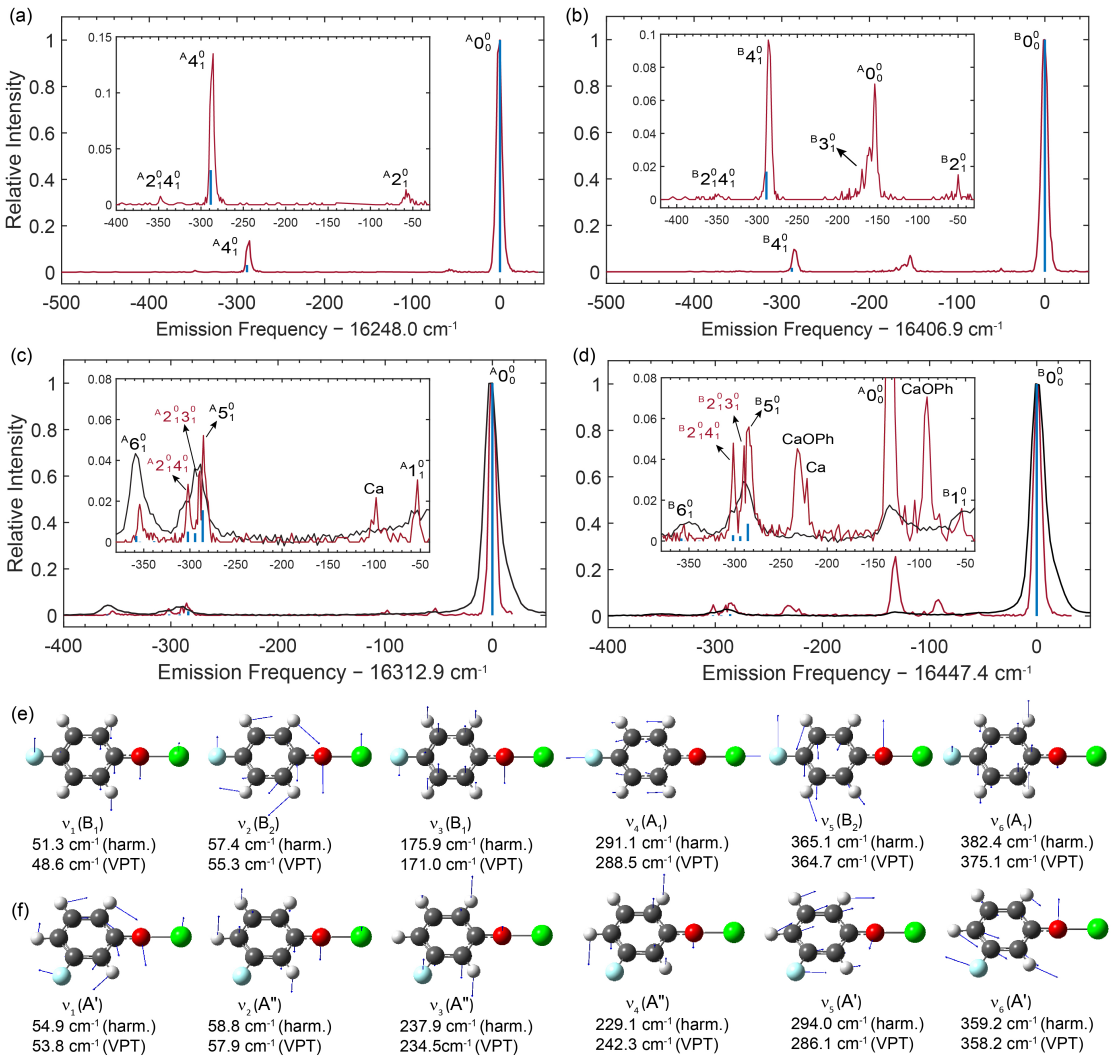

Figure 3.9: (a) and (b) Dispersed spectra for the $\widetilde{A} \rightarrow \widetilde{X}$ and $\widetilde{B} \rightarrow \widetilde{X}$ transitions of CaOPh-4-F molecule, respectively. Only a single peak is observed for the stretching mode v_4 around -286 cm^{-1}. Due to the absence of Fermi resonance coupling, the theoretical relative strengths (blue vertical lines) are calculated under harmonic approximation. (c) and (d) Dispersed spectra for the $\widetilde{A} \rightarrow \widetilde{X}$ and $\widetilde{B} \rightarrow \widetilde{X}$ transitions of CaOPh-3-F molecule, respectively. The black traces are taken from previous work [125], measured with a spectral resolution of ≈ 0.5 nm, while the red traces represent an improved measurement with resolution of ≈ 0.20 nm. (e) and (f) Vibrational displacements of the six lowest-frequency fundamental modes in the ground state. Theoretical frequencies and symmetries for these modes are given. All vibrational modes are labeled with increasing frequency regardless of their symmetries.

symmetry is reduced from C_{2v} to C_s, the coupling phenomenon is markedly different. While previous DLIF studies [125] of $\widetilde{A} \rightarrow \widetilde{X}$ and $\widetilde{B} \rightarrow \widetilde{X}$ transitions found a broad peak for the stretching mode peak v_5 at -290 cm^{-1} (black traces in Figs. 3.9c-d), the present, higher resolution spectra, resolve three separate transitions, which are also predicted by the VPT calculation (blue lines in Figs. 3.9c-d). The strongest peak at -284 cm^{-1} corresponds to the vibrational decay to the stretching mode v_5 (A', Fig. 3.9f), while the other two peaks at -291 cm^{-1} and -302 cm^{-1} are assigned to two combination levels, $v_2 + v_3$ (A') and $v_2 + v_4$ (A'), respectively. This more complex coupling behavior can be attributed to the lower C_s symmetry of CaOPh-3-F molecule. All three vibrational modes, v_2, v_3 and v_4, are out-of-plane bending modes with A'' symmetry. The combination levels of $v_2 + v_3$ or $v_2 + v_4$ results in A' symmetry and frequencies close to that of the stretching mode v_5 (Fig. 3.9f), leading to intensity borrowing and activation of these unexpected combination bands.

The absence of Fermi resonance in the CaOPh-4-F stretching mode decay and the presence of complex coupling in CaOPh-3-F are further supported by the excitation spectra obtained for the excited states. Fig. S2 in [161] demonstrates a single peak corresponding to the stretching mode v_4 in the excitation spectra of CaOPh-4-F, while the excitation spectra of CaOPh-3-F (Fig. S3 in [161]) reveal the presence of three transitions in the frequency region associated with the stretching mode v_5.

A more complex molecule with three F atoms substituted, CaOPh-3,4,5-F_3, has also been revisited as it is potentially the most attractive calcium phenoxide for optical cycling [125]. The DLIF spectra in Fig. S4 and excitation spectra of excited states in Fig. S5 both reveal the presence of doublet vibrational peaks near the stretching mode peak region. One of these peaks corresponds to the stretching mode v_6 with an A_1 symmetry, while the other peak arises from a combination band involving two out-of-plane bending modes v_1 (B_1) and v_4 (B_1).

To investigate the influence of metal atoms on anharmonic vibrational coupling, we have also studied two strontium phenoxides, SrOPh and SrOPh-3,4,5-F_3. A previous study [143]

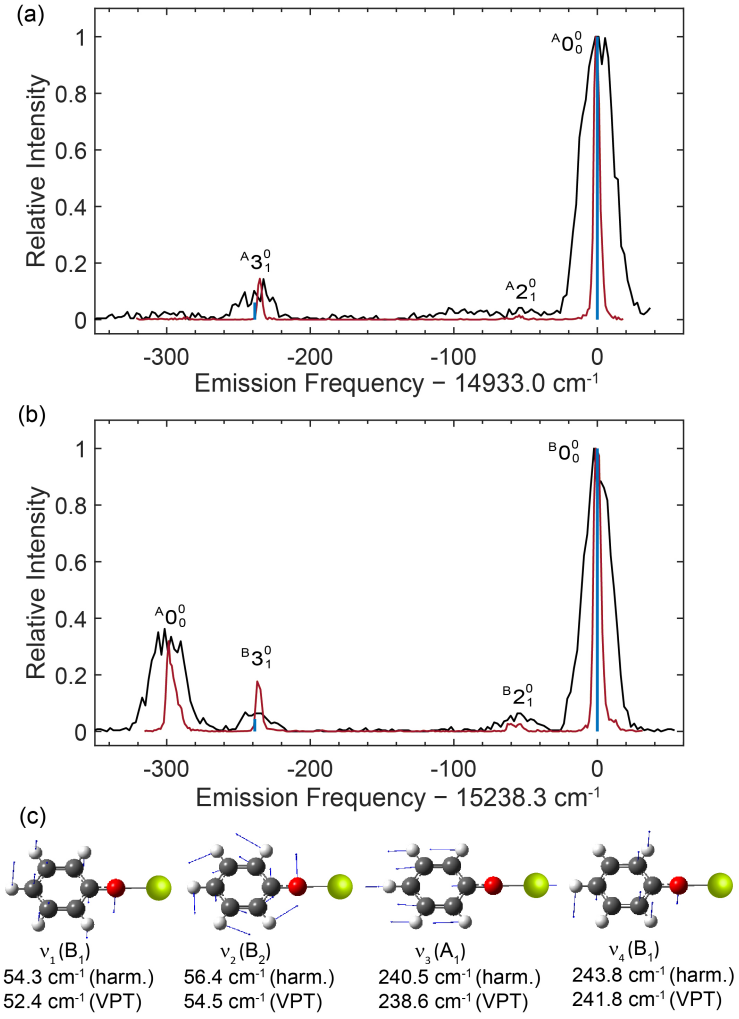

Figure 3.10: (a)-(b) DLIF spectra obtained for the $\widetilde{A} \rightarrow \widetilde{X}$ and $\widetilde{B} \rightarrow \widetilde{X}$ transitions of SrOPh molecules. The black traces are taken from a previous study [143], measured with a spectral resolution of ≈ 0.5 nm, while the red traces represent an improved measurement with a resolution of ≈ 0.20 nm. The blue sticks show the calculated frequency (VPT) and relative strength (harm.) of vibrational decays. (c) Vibrational displacements of four lowest-frequency fundamental modes. Theoretical frequencies and symmetries for these modes are provided. All vibrational modes are labeled with increasing frequency regardless of their symmetries.

has provided low-resolution DLIF spectra for these molecules. Figs. 3.10a-b display the higher resolution DLIF spectra recorded here for SrOPh from the excited $\widetilde{A}$ and $\widetilde{B}$ states.

Only a single transition is observed for the stretching mode v_3 at around -235 cm^{-1}, indicating the lack of Fermi resonance. The absence can be explained by the different symmetry of the combination level of $v_1 + v_2$ (A_2) and the stretching mode v_3 (A_1), along with a substantial energy gap of either 130 cm^{-1} (harm.) or 132 cm^{-1} (VPT), as shown in Fig. 3.10c. This is also validated by the presence of a single stretching mode transition in the excitation spectra of $\widetilde{A} \leftarrow \widetilde{X}$ and $\widetilde{B} \leftarrow \widetilde{X}$ in Fig. S6.

Contrary to SrOPh, both DLIF spectra (Fig. S7) and excitation spectra (Fig. S8) of SrOPh-3,4,5-F_3 exhibit a weak transition assigned to the $v_1 + v_3$ combination mode close to the stretching-mode peak v_4, implying the existence of a small anharmonic coupling, as also captured by the VPT calculation.

The branching ratios and frequencies of all observed vibrational modes in the DLIF and excitation spectra are summarized in Tables S3-S6 of [161]. From these, a consistent understanding of the role of vibrational coupling in the calcium and strontium phenoxides molecules emerges. As summarized in Tables 3.2 and S3-S4, except for CaOPh-4-F and SrOPh molecules, all examined molecules show additional off-diagonal decays near the most off-diagonal decays to the stretching mode (v_k). Specifically, a ombination band ($v_i + v_j$) comprising two low-frequency bending modes, which is absent in the harmonic approximation, is activated by anharmonic vibrational coupling. This occurs in a predictable manner according to the vibrational frequency spacing and vibrational mode symmetry and can be captured by the VPT calculations.

The strength of this coupling can be estimated from an intensity borrowing model in a molecular system with effects of anharmonicity [164]. Following the convention, the anharmonic vibrational Hamiltonian is expressed as

$$H_{anh}^{(\widetilde{X})} = \frac{1}{6} \sum_{i,j,k} \left(\frac{\partial^3 V^{(\widetilde{X})}}{\partial Q_i \partial Q_j \partial Q_k} \right)_0 Q_i Q_j Q_k + \ldots, \tag{3.6}$$

where the higher-order anharmonic terms in the vibrational potential energy in the $\widetilde{X}$ state ($V^{(\widetilde{X})}$) are negelected. By rewriting the normal coordinates Q_i, Q_j and Q_k with the anni-

Table 3.2: Summary of Fermi resonance for the most off-diagonal decays to the stretching modes in all studied molecules. All frequencies and coupling strengths are given in units of cm^{-1}.

Species	Theo. (VPT)					Exp.		
	v_i	v_j	v_k	$\Delta v^{(0)}_{ij,k}$	$\Delta v_{ij,k}$	$\Delta v'_{ij,k}$	$\beta_{k/ij}$	$\phi^{(\widetilde{X})}_{ij,k}$
CaOPh	60.0 (B_1, v_2)	241.0 (B_1, v_3)	315.2 (A_1, v_4)	14.2	19.6	18.0(0.4)	2.9(0.8)	7.9(0.6)
CaOPh-3-F	57.9 (A'', v_2)	234.5 (A'', v_3)	286.0 (A', v_5)	6.4	8.2	6.1(0.6)	3.0(1.0)	-
	57.9 (A'', v_2)	242.3 (A'', v_4)	286.0 (A', v_5)	14.2	16.0	17.4(0.6)	1.9(0.4)	-
CaOPh-3,4,5-F_3	48.9 (B_1, v_1)	217.2 (B_1, v_4)	271.2 (A_1, v_6)	5.1	9.6	8.2(0.4)	1.0(1.0)	4.2(2.4)
SrOPh-3,4,5-F_3	45.7 (B_1, v_1)	143.6 (B_1, v_3)	203.5 (A_1, v_4)	14.2	16.2	18.7(1.0)	9.0(4.0)	6.0(2.6)
CaOPh-4-F	48.6 (B_1, v_1)	171.0 (B_1, v_3)	288.5 (A_1, v_4)	68.9	None	No doublet observed		
SrOPh	52.4 (B_1, v_1)	54.5 (B_2, v_2)	238.6 (A_1, v_3)	131.7	None	No doublet observed		

Notes: v_i and v_j are two low-frequency out-of-plane bending modes. The combination band of $v_i + v_j$, FCF-inactive mode under harmonic approximation, is likely to show up due to the intensity borrowing from Fermi resonance coupling with the most-off diagonal decays to the stretching mode v_k based on the frequency spacing and symmetry. $\Delta v^{(0)}_{ij,k} = |v_k - v_i - v_j|$ is the unperturbed frequency separation and $\Delta v_{ij,k} = |v_k - v_i v_j|$ are the predicted Fermi resonance doublets ('None' indicates no Fermi resonance for the mode v_k). The difference of $|\Delta v^{(0)}_{ij,k} - \Delta v_{ij,k}|$ indicates the frequency shift due to Fermi resonance. All frequencies are calculated at the anharmonic-VPT level of theory. $\Delta v'_{ij,k}$ is the measured frequency spacing between the combination band and the stretching mode. $\beta_{k/ij}$ is the averaged measured peak intensity ratio of the stretching mode to the combination band in $\widetilde{A} \rightarrow \widetilde{X}$ and $\widetilde{B} \rightarrow \widetilde{X}$ transitions. $\phi^{(\widetilde{X})}_{ij,k}$ is the estimated Fermi resonance coupling strength between the combination band and the stretching mode in the ground state according to equation (3.11). Due to the complexity of coupling between multiple vibrational bands, the coupling strength of CaOPh-3-F could not be estimated from the measurement.

hilation and creation operators for the vibration modes, *e.g.*, $Q_i = \frac{1}{\sqrt{2}}\left(\hat{a}_i^\dagger + \hat{a}_i\right)$ [165], the Fermi resonance Hamiltonian affecting the combination mode $v_i + v_j$ and fundamental mode v_k in the ground $\widetilde{X}$ state can be expressed as:

$$H^{(\widetilde{X})}_{FR,ij,k} = \phi^{(\widetilde{X})}_{ij,k}\left(\hat{a}_i^\dagger \hat{a}_j^\dagger \hat{a}_k + \hat{a}_i \hat{a}_j \hat{a}_k^\dagger\right), \tag{3.7}$$

where $\phi^{(\widetilde{X})}_{ij,k}$ is the coupling strength. In the absence of the Fermi resonance (*i.e.* $\phi^{(\widetilde{X})}_{ij,k} = 0$), we assume the probability of decay from the excited state $|e, v' = 0\rangle$ to $|\widetilde{X}, v''_k\rangle$ (denoted

as I_{e0,Xv_k}) is appreciable, while decay to the combination mode $|\widetilde{X}, v_i'' + v_j''\rangle$ (denoted as I_{e0,Xv_iv_j}) is negligible. As $\phi_{ij,k}^{(\widetilde{X})} \neq 0$, the extra and main line intensities can be presented as

$$I'_{e0,Xv_iv_j} = \left(C_{k,ij}^{(X)}\right)^2 I_{e0,gv_k} \tag{3.8}$$

and

$$I'_{e0,Xv_k} = \left[1 - \left(C_{k,ij}^{(X)}\right)^2\right] I_{e0,gv_k}, \tag{3.9}$$

respectively, where the coefficient $\left(C_{k,ij}^{(X)}\right)^2$ is the ratio of the borrowed intensity. In experiment, the ratio of the two intensities are measured, *i.e.*, $\beta_{k/ij} = I'_{e0,Xv_k}/I'_{e0,Xv_iv_j} = \left(C_{k,ij}^{(X)}\right)^{-2} - 1$. Treating the case of only one combination mode mixing with the stretching mode as a simple two level system, one can obtain

$$C_{k,ij}^{(X)} = \sqrt{\frac{1}{2}\left(1 - \frac{\Delta v_{ij,k}^{(0)}}{\Delta v'_{ij,k}}\right)}, \tag{3.10}$$

and

$$\phi_{ij,k}^{(\widetilde{X})} = \frac{\sqrt{\beta_{k/ij}}}{\beta_{k/ij} + 1}\Delta v'_{ij,k}, \tag{3.11}$$

where $\Delta v_{ij,k}^{(0)}$ is the unperturbed energy gap between the modes. Using this expression, coupling strengths are extracted and shown in Table 3.2. For this comparison, though the unperturbed gap $\Delta v_{ij,k}^{(0)}$ could be evaluated from the measurement ($\beta_{k/ij}$ and $'_{ij,k}$) and the above equations, we employ the calculated VPT frequencies for a straightforward comparison of calculated and measured gaps.

Although Fermi resonance occurring between multiple vibrational modes (v_5, $v_2 + v_3$, $v_2 + v_4$) is observed in CaOPh-3-F, evaluating the anharmonic coupling strengths between these modes is challenging. This is due to the mismatch between the numbers of independent elements and available observables: we represent the three-level system with a 3×3 matrix, containing six independent elements, but only have five observables (three frequencies and two relative intensity ratios). Such mismatch results in non-unique solutions from the intensity borrowing model, leading to significant uncertainties in the matrix elements. As a result, the measurement of coupling coefficients of CaOPh-3-F is not available in Table 3.2.

The observed anharmonic couplings have substantial implications for the laser-cooling of these molecules. The presence of additional vibrational decay pathways requires the use of additional repumping lasers to achieve efficient photon scattering [15, 148, 149]. Therefore, it is crucial to design molecules that can minimize or avoid such resonant couplings. Several such strategies for mitigating vibrational anharmonic coupling are readily apparent in these molecules. First, the spacing of vibrational energy levels can be tailored to maintain sufficient separation of *harmonic states* to avoid detrimental Fermi resonances. This can be achieved via several approaches, such as substituting groups on the phenyl ring (*e.g.* CaOPh-4-F) or altering the metal atom hosting the optical cycling center (*e.g.* SrOPh). For example, according to theoretical calculations, it is anticipated that CaOPh-4-Cl, CaOPh-4-OH, SrOPh-3-F and SrOPh-3-OH will not exhibit Fermi resonance coupling between the stretching mode and the bending mode combination band due to their large frequency spacings, as indicated by values exceeding > 60 cm^{-1}, (Table S7 in [161]). Second, choosing molecules with higher symmetry may protect the stretching mode from mixing with other nearby combination modes, as Fermi resonance only affects modes in the same symmetry.

As molecular size and complexity increase above the molecules studied here, the increased density of vibrational states from the increasingly diverse molecular structure will pose challenges for the effectiveness of the mitigation methods discussed here. Selecting suitable ligands with strong electron-withdrawing capability can offer a general suppression of Fermi resonance and higher order couplings. For these molecules, as the orbital motion of the electrons is highly separated from the vibrational degrees of freedom [110, 125], the anharmonic effects induced by these molecular orbitals can be mitigated, therefore the couplings relative to the most off-diagonal decays are suppressed.

3.3.5 Conclusions

In summary, we have studied Fermi resonance coupling of calcium and strontium phenoxides and their derivatives, employing high-resolution dispersed laser-induced fluorescence and ex-

citation spectroscopy. Fermi resonance phenomena were observed in the ground and excited states for CaOPh, CaOPh-3-F, CaOPh-3,4,5-F_3 and SrOPh-3,4,5-F_3 molecules. This resonance led to intensity borrowing, particularly in vibrational combination bands consisting of two low-frequency bending modes close in energy to a stretching mode. The Fermi resonance effect was absent in CaOPh-4-F and SrOPh due to large frequency differences between the combination band and the stretching mods. While Fermi resonance does not significantly alter vibrational branching ratios, it does require additional repumping lasers for effective optical cycling. Several strategies were presented to minimize the impact of Fermi resonance in phenoxide-related molecules, including ligand substitutions and changes in metal atoms. These findings help to provide a roadmap for the design and engineering of ever-larger and more intricate molecular systems with enhanced optical cycling properties for advancing quantum information science.

CHAPTER 4

Extending Optical Cycling to Larger Scaffolds

4.1 Optical Cycling Functionalization of Arenes

4.1.1 Introduction

Experimental quantum information science is built on systems that feature easily prepared and measured quantum states, such as spin states, for utilization as qubits. Currently, superconducting qubits and trapped atomic species arguably lead this quantum hardware race. Atoms and atom-like molecular moieties with optically-induced, closed transitions have been explored in the field of atomic physics, particularly in the context of laser cooling, for quantum computation, analog quantum simulation and precision measurement [22, 74, 89, 90, 93]. Alkaline earth and, recently, other metals, ionically bonded to an oxygen linearly bonded to an R group ligand (M-O-R) were shown to be capable of optical cycling, such as SrOH, CaOH, BaOH and most recently, YbOH [91, 166–169]. Additionally, symmetric top molecules, such as such as $CaOCH_3$, $SrOCH_3$, $BaOCH_3$ and $YbOCH_3$, were shown to be optical cycling centers (OCCs) [25, 92, 170–175].

Even larger molecules, such as calcium phenoxides, have been proposed as M-O-R OCCs theoretically [94, 110]. Recently, an extension of such optical cycling centers toward larger polyatomic molecules has been realized in the laboratory. It is currently an open question whether the optical cycling of functionalized molecules can be engineered so that the Franck-Condon factor (FCF) can be retained in the large molecule limit, *i.e.* where the molecular ligand grows beyond a size where its details no longer affect the optical cycling. Should this

prove possible, it would open the door to adding modularized quantum state readout to any substrate to which such a ligand can be attached.

In this contribution, we show that the ligand, L, in Ca-O-L can grow beyond a single carbon ring to larger arenes. This is possible because the geometries of arenes are relatively rigid and their electronic states feature substantial gaps in their highest occupied molecular orbitals (HOMO) to lowest unoccupied molecular orbitals (LUMO), which do not mix with the states on Ca, because they belong to a different irreducible representation in the C_s or C_{2v} point group. The energies of the electronic states of arenes are also easily tuned by electron-withdrawing substitutions on the ring and via arene size.

Conveniently for this investigation, arenes are abundant throughout the universe [176–179] and extensively characterized by, for example, infrared (IR) spectroscopy [180]. Databases exist containing vibrational harmonic spectra for arenes, namely polycyclic aromatic hydrocarbons, up to hundreds of carbon atoms [181, 182]. The extension toward application of arenes in optical cycling benefits from both existing insights from laser cooling molecules and knowledge of extensive arene IR vibrational spectra. Thus, much of the groundwork necessary for adding optical cycling centers to arenes for quantum measurements and computing is already in place.

Previously, identifying optically-cyclable molecules required either finding spectrocopic properties (such as diagonal FCFs) in the literature, or by trial and error. However, recently, some design strategies have emerged. Ivanov *et al.* showed that an alkaline earth metal radical can be attached to phenyl, cyclopentadienyl and pyrrolide and the metal could retain some optical cycling capabilities [94]. Additionally, they showed multiple optical cycling radicals could be attached to the same ligand if they are sufficiently spaced [136]. In a recent study, we showed that a cycling Ca or Sr radical attached to a phenoxide can have its diagonal FCF boosted by chemical substitution on the far side of the carbon ring [110]. This revealed an underlying design principle: when the electronic transition is isolated on a metal radical, the FCF responds in a manner predicted by its substituents' Hammett parameters.

Specifically, electron-withdrawing groups spatially isolated from the cycling center increase the diagonality of the FCF by creating more similar ground and excited state potential energy surfaces, where the largest off-diagonal decay is the Ca-O stretching mode.

This earlier work hinted that the ligand HOMO-LUMO gap might play an important role in keeping the electronic states of the cycling center (and the associated transition) isolated. Here, we hypothesize that the HOMO-LUMO gap is one of the key design parameters for larger molecules that can support optical cycling centers with diagonal FCFs. We explore this possibility on the basis of the Ca-O-L platform, where L is an arene. Arenes are rigid molecules, so their HOMO-LUMO gap can be reliably modified via the number of conjugated aromatic rings. Therefore, we explore arene ligands of increasing size, from naphthalene to ovalene, as well as the large-ligand-limit simulated by a graphene edge. We show the L's HOMO-LUMO gap as an important design consideration for increasingly larger ligands in optical cycling. We additionally explore the relative orientation of L and Ca (or Ca-O placement on the arene rings), as well as further fuctionalization of arenes with fluorines, which was previously shown to help diagonalize the FCF in Ca and Sr phenoxides [110]. All studied molecular ligands are shown in Figure 4.1, while a 2D graphene material ligand is discussed later in Figure 4.6.

4.1.2 Computational Methods

All molecular calculations in this work were done at the PBE0-D3/def2-TZVPPD level of theory [106–108] with DFT and time-dependent density functional theory (TD-DFT) on a superfine grid using Gaussian16 [101]. This level of theory was previously extensively benchmarked against multireference CASPT2 calculations for CaOH, SrOH, CaF, SrF and $CaOCH_3$ [110]. Additionally, electronic excitation energies for neutral naphthalene, pyrene and coronene, computed with TD-DFT matched the experimental data within 0.04 eV (see Supporting Information of [124]). FCFs, including Duschinsky rotations, were calculated from harmonic vibrational frequencies. The harmonic approximation is expected to be re-

liable, because the optical center is well-isolated from the modes of the ligand and the anharmonicity, if any, will be similar from the ground to excited state which should not affect the diagonality of the FCF, as detailed previously [110]. For naphthalene, anthracene and tetracene, the main anharmonic modes were the C-C or C-H stretches, in the 1300-1600 cm^{-1} range [183, 184], sufficiently far from Ca-O stretching or bending modes (dominant contributors to the FCF), which are less than 700 cm^{-1}. However, a discussion of anharmonic effects is included in the SI of [139]. Additionally, rotational losses are outside the scope of this paper, but a discussion on asymmetric tops and rotational losses can be found in Augenbraun *et. al.* [95].

OCCs bound to the edge of a single-layer graphene were computed using VASP [185–188]. Geometry optimizations were carried out using PBE [189]. The hybrid functional, HSE06, was used for charge density and density of states calculations [190–192], as it has been previously benchmarked against experiment for the prediction of band gaps [193]. The interactions between the ionic cores and the electrons were described using the projector augmented-wave (PAW) potentials [194, 195]. A $1 \times 4 \times 1$ Monkhorst-Pack k-point grid and a plane wave cutoff energy of 400 eV were employed. The 2D graphene sheet was represented as an infinite strap with periodic boundary conditions, in which the two edges were covered with H atoms, one of which was removed to deposit CaO. We used a large unit cell of 15 Å $\times$ 15 Å $\times$ 25 Å to prevent the interaction between periodic images. The top three layers of C atoms and the top-edge H atoms were relaxed during the geometry optimization, with a convergence criterion of 0.01 eV/atom.

4.1.3 Results and Discussion

For a species to host an optical cycling transition, the first electronic excitation must be exceptionally vertical and feature minimal vibrational leakage channels for non-radiative decay. The transition should also be isolated from other excitations and lie below the dissociation threshold. Previous calculations and experiments identified the existence of low-lying excited

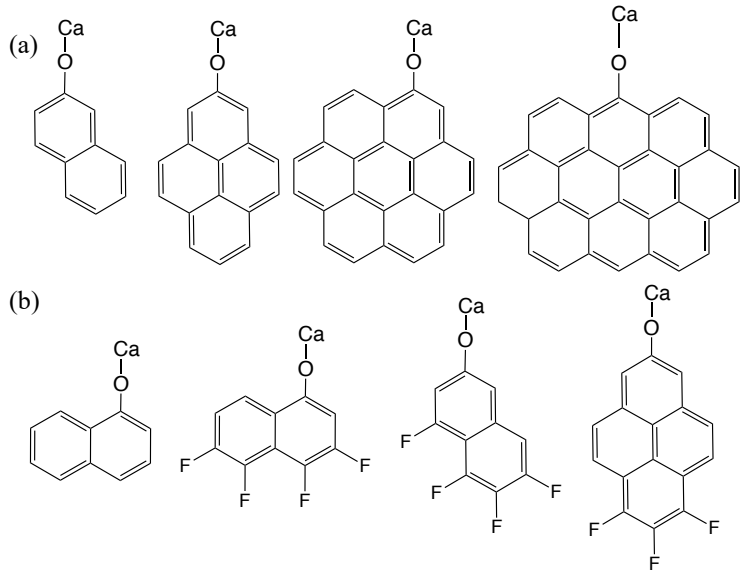

Figure 4.1: Arenes decorated with optical cycling motifs that are considered in this study. Row (a) from left to right: naphthalene, pyrene, coronene, ovalene. Row (b): h-naphthalene ("h" stands for "horizontal") and fluorinated derivatives (F-h-naphthalene, F-naphtalene, F-pyrene).

states for CaL complexes [166–169]. For the CaO-arenes of C_s symmetry, the A'' state lies close in energy to the A' state examined in this work. Our calculations in Table S2 suggest that the A'' and A' states have small energy splitting but are not degenerate, with the magnitude of the splitting similar to that found in CaOPh [110]. There is a possibility that these states cross via out of plane vibrations, in which case DFT is no longer a sufficient approach, whereas multireference approaches are very expensive for systems of this size. Hence, it will be important to verify experimentally that the A'-A'' states do not reorder. For the vertical transition, it is advantageous for both the ground and the excited state electron densities to be localized on the cycling center (in this work, the Ca radical) in Ca-O-L and feature minimal (and equal) amount of Ca-O bond covalency. The natural transition orbitals (NTOs) of the HOMO ($\tilde{\mathrm{X}}$) to LUMO ($\tilde{\mathrm{A}}$) transition for CaO-naphthalene and CaO-coronene are shown in Figure 4.2. The electron density remains isolated on the metal, with a very small contribution from the oxygen. The Ca-O bond ionicity is confirmed for the ground states via natural population analysis (NPA) in Table 4.1. These results suggest that all molecules

feature highly-ionic Ca-O bonds and the ionicity increased slightly upon fluorination.

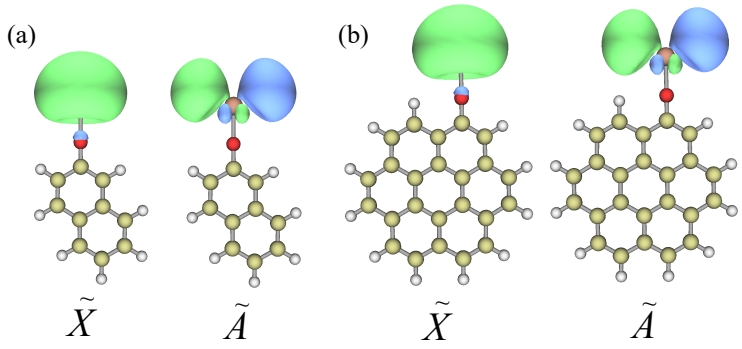

Figure 4.2: CaO-functionalized naphthalene and coronene NTOs of the ground to first excited state transition ($\tilde{X} \rightarrow \tilde{A}$) with an isosurface value of 0.03. No electron density can be found far from the calcium.

Next, we explore the similarity between the ground and first excited potential energy surfaces (Table 4.2). Ca-O bond length changes between the minimum on the ground state surface and the minimum on the excited state surface are below 0.02 Å for all considered species. The bond length change becomes smaller upon fluorination, consistent with the increasingly isolated character of the radical and in accordance with the design principle introduced in [110]. We find that the placement of the O-Ca moiety on the arene plays an important role, as the "horizontal" variants have larger differences between the ground and the excited potential energy surfaces.

Although the unpaired electron is localized on the metal throughout the transition, there is a nearly linear decrease in FCF as the arene ligand increases in size from naphthalene to coronene. The decrease can be related to the slight decrease in the isolated character of the frontier orbitals on the cycling molecules (Figure 4.3). As the arene gets larger, its intrinsic HOMO-LUMO gap (which, for example, in CaO-pyrene corresponds to the HOMO-1-LUMO+1 gap, shown in blue in Figure 4.3), closes and approaches the metal-based electronic transition (shown in black in Figure 4.3). The ligand and Ca's lowest unoccupied orbitals become particularly close as the arene increases in size. While FCFs

Substituent	Charge (Ca)	Charge (O)
benzene	0.95672 [110]	-1.06673 [110]
naphthalene	0.95817	-1.06100
pyrene	0.95924	-1.06000
coronene	0.96138	-1.04898
ovalene	0.96578	-1.03405
h-naphthalene	0.96077	-1.05630
F-h-naphthalene	0.96053	-1.03787
F-naphthalene	0.96086	-1.04382
F-pyrene	1.00522	-1.09231

Table 4.1: Computed NPA charges on Ca and O for all CaO-arenes' ground states.

can be improved slightly by substituting electron-withdrawing groups on the ligand, once L becomes ovalene, the vertical transition is lost due to switching of the excited states, whereby the LUMO becomes an arene-centered orbital, as seen in Figure 4.3. Fluorinating these species systematically shifted all energy levels lower in energy, but the relative HOMO-LUMO gaps remained similar to their unsubstituted versions (see SI of [124]). Although bond length is a good indicator for FCF when adding electron-withdrawing groups, CaO-arenes have varying ligand HOMO-LUMO gap sizes that can interact with the metal and affect the FCF more than just bond length change. This is because the ligand HOMO-LUMO gap is closer to the metal HOMO-LUMO gap, so the Ca-O bond is less ionic and other vibrational leakage pathways, such as in-plane bending, become more dominant.

The HOMO-LUMO gap of the "ligands", where the electron density is not on the metal but solely on the arene molecule, are shifted, but still close to experimental electronic excitation energies of their singlet, neutral counterparts. These neutral species' electronic excitations were benchmarked against experiment [196–198], using our computational method (see SI of [124]).

Substituent	FCF	Ca-O Change (Å)
benzene	0.958 [110]	-0.0168 [110]
naphthalene	0.958	-0.0163
pyrene	0.947	0.0164
coronene	0.931	-0.0140
ovalene	0.167	-0.0010
h-naphthalene	0.931	-0.0163
F-h-naphthalene	0.917	-0.0133
F-naphthalene	0.968	-0.0127
F-pyrene	0.962	-0.0151

Table 4.2: FCFs and Ca-O bond length change (excited state - ground state) for all molecules.

From a vibrational mode perspective, the dominant off-diagonal decay mode changes depending on the arene size and ligand symmetry (Figure 4.4). In CaO-naphthalene, the first two off-diagonal modes are the symmetric Ca-O stretch and the Ca-O bend and stretch. However, with coronene, the dominant off-diagonal mode is the Ca-O in-plane bending, followed by the Ca-O symmetric stretch. This could be due to the interaction of the unpaired electron on Ca with the delocalized electronic states on the arene; these states have a greater spatial overlap in the "horizontal" variants and better match in energy with larger arenes. As such, increasing arene size disrupted the symmetric stretch mode and reduced symmetry in the excited state potential energy surface with respect to the ground state surface. For the same reason, we find placing the cycling centre on a C_6-ring that is more isolated from the rest of the polyaromatic system of the arene helps diagonalize the FCF. Besides vibrational losses due to off-diagonal vibrational decays, symmetries like C_s can have rotational branching which causes further loss. As discussed previously [92, 95], however, carefully chosen rotational transitions following specific rotational and parity selection rules can limit

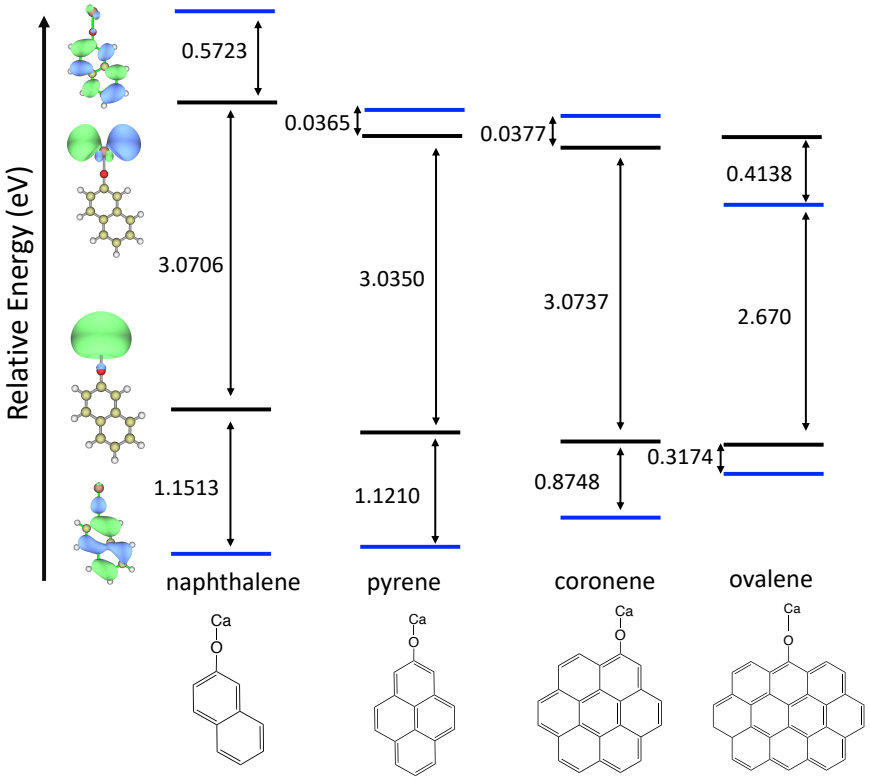

Figure 4.3: DFT energies of electron density localized on the ligand, or "ligand HOMO-LUMO" gap (blue) and density localized on the metal, or "metal HOMO-LUMO gap" (black), for CaO-naphthalene, CaO-pyrene, CaO-coronene and CaO-ovalene. As ligand size increases, the ligand HOMO-LUMO gap decreases and approaches the isolated metal-metal electronic transition, until the transition is disrupted by the switching of the metal and ligand LUMOs, as seen in CaO-ovalene.

or eliminate the rotational losses.

The FCF decrease can be mitigated slightly by adding electron-withdrawing groups in positions on the arenes such that the Ca-O symmetric stretch behavior is favored (*i.e.* far away from Ca-O), as seen in Table 4.2 and Figure 4.5. The substituted F-versions of the molecules designed in this way have more similar ground and excited state potential energy surfaces and thus, larger FCFs than unsubstituted arenes. Electron withdrawing to improve the symmetry of potential energy surfaces is described in more detail in the reference [110].

Interestingly, we find that for the "horizontal" arene ligands, where the in-plane bend

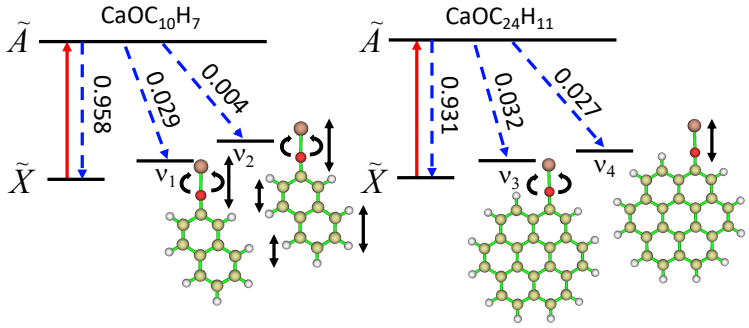

Figure 4.4: Photon cycling scheme with an excitation (red) to the first excited electronic state and decay (blue) to the ground electronic state for CaO-naphthalene and CaO-coronene. The FCFs are shown along with each decay pathway.

mode is already the dominant vibrational leakage channel, fluorination does not help diagonalize the FCF (Table 4.2 and Figure 4.5). When fluorines are substituted, FCFs decrease and the bend off-diagonal decay increases to 0.05. Therefore, we find the "vertical" arene ligands more favorable than "horizontal" arene ligands for optical cycling.

Since increasing arene ligand size appears to lead to the eventual destruction of diagonal FCFs, we pushed the concept to its limit and examined Ca-O bound to the edge of 2D graphene. We consider two edge structures (Figure 4.6): in E1, Ca-O-C maintains a locally linear structure on the ground electronic state, while in E2, Ca-O-C is bent with an angle of 163.9°, due to the asymmetric local structure and charge density.

In the density of states (DOS) calculations, we see density mixing on graphene and the metal, for both structures and both for the ground and excited states. This disrupts the clean transitions, leading to poor FCFs. This is further illustrated by the plots of the charge density, showing the lack of localization and the spread of the charge density throughout the graphene edge. The orbitals of Ca mix with C orbitals and split into two mixed orbitals. Thus, while functionalization of large-band-gap diamond with M-O optical cycling centers was proposed to be possible [135], the graphene edge is not a suitable substrate for this purpose. This is explained by the ligand band gap paradigm proposed in this work.

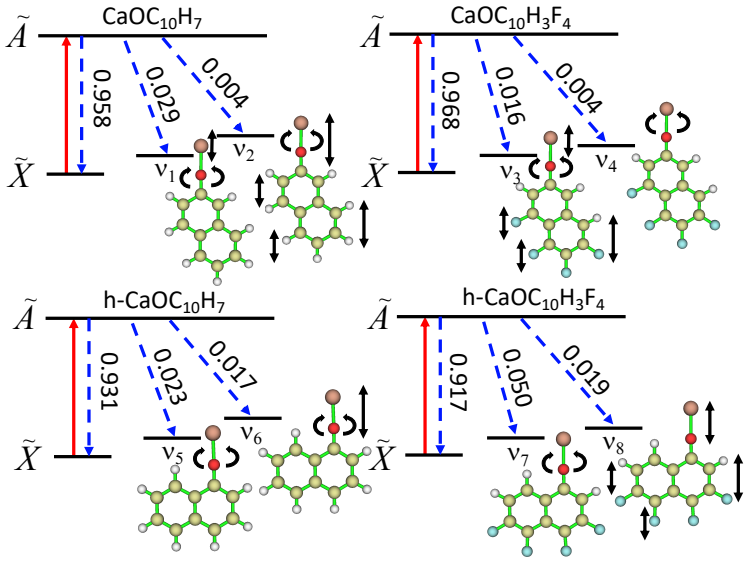

Figure 4.5: Photon cycling scheme with an excitation (red) to the first excited electronic state and decay (blue) to the ground electronic state for, from left to right: CaO-naphthalene, CaO-F-naphthalene, CaO-h-naphthalene and CaO-F-h-naphthalene. The FCFs are shown along with each decay.

Finally, how could one synthesize large arenes functionalized with optical cycling centers? There are many synthetic routes which produce alkaline-earth-radical-containing molecules via reactions of the metal atoms with volatile ligands [92, 174, 199]. The metal atoms are generated either by evaporation in a Broida-type oven [199] or by laser ablation of the metal targets. The atoms then react with the gaseous precursors to form the products. The reaction rate is likely enhanced when pumping the ground-state metal atoms to the metastable excited states.

Supersonic jet and cryogenic buffer-gas cooling [92, 174] are commonly employed to make products vibrationally and rotationally cold. The functionalized arenes discussed here can be produced using similar method. Take CaO-naphthalene as an example: a nanosecond 1064 nm Nd:YAG laser can be used to ablate the calcium target producing Ca atoms. Since the ligand, 2-naphthol, is involatile and has a melting point around 120 °C, a heated source can be used to melt the 2-naphthol to generate enough vapor, which is entrained in a cryogenic

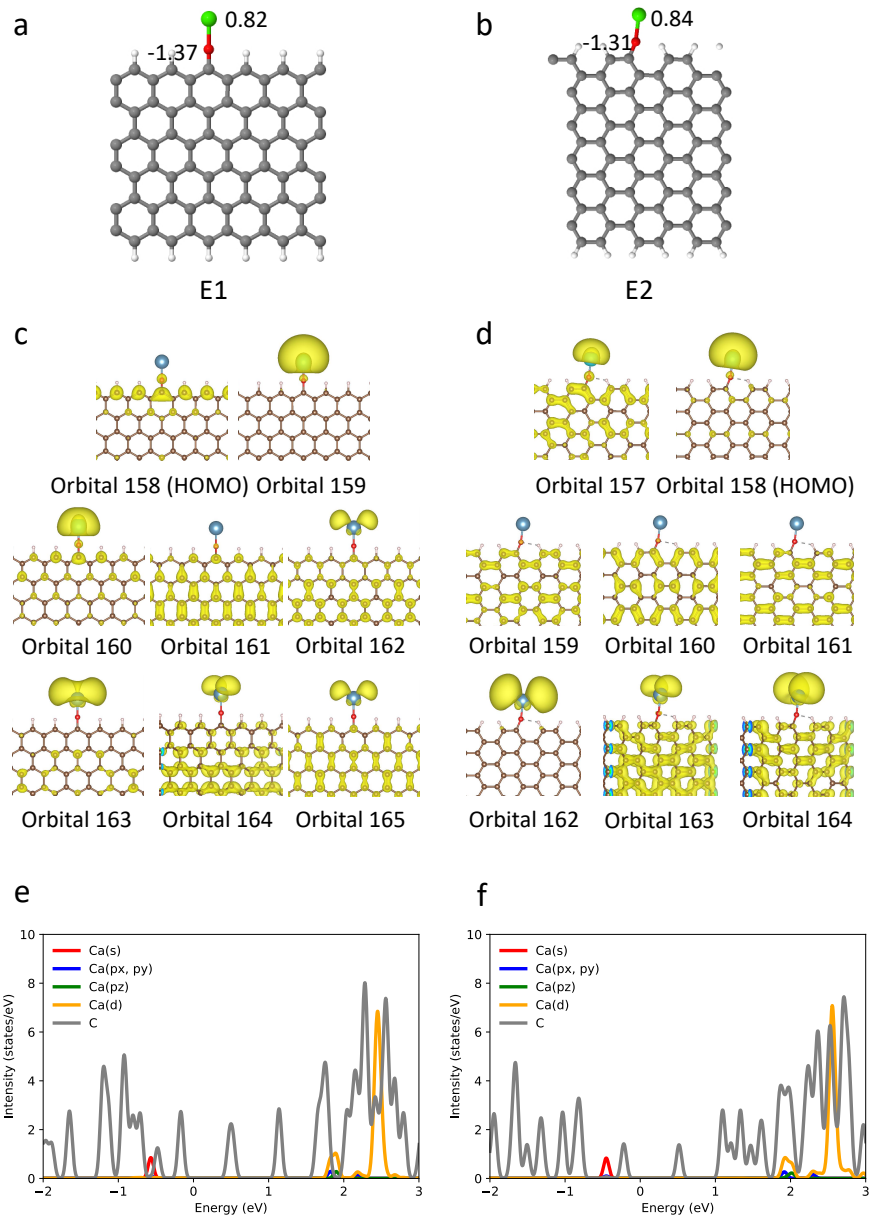

Figure 4.6: (a) (b) Optimized ground state structures for two edge structures, E1 and E2. The atomic charges on Ca and O from the Bader charge analysis are also shown. (c) (d) Electron density of molecular orbitals for CaO supported on two graphene edges. The isosurfaces are plotted with an isovalue of 0.001. (e) (f) PDOS for CaO supported on two graphene edges.

buffer gas of helium to react with Ca atoms. The formed CaO-naphthalene can be probed by laser spectroscopy. At cryogenic temperature, clustering could be possible between the helium gas and molecules with binding energies typically around 100 cm^{-1} [200] which may impede the reaction efficiency. However, previous buffer gas cooling experiments including naphthalene ($C_{10}H_8$) [201], trans-stilbene ($C_{14}H_{12}$) and nile red ($C_{20}H_{18}N_2O_2$) [200], showed no evidence of forming helium-molecule clusters at a cold temperature, around 7 K, though an upper limit of 5% is estimated for the population of He-trans-stilbene cluster. This is likely due to the low number density of helium (typically around 10^{14} cm^{-3}) in the buffer gas condition. The arenes studied here are of similar size to these studies, so likely will not cluster with He, not affecting reaction efficiency with the ablated metal atoms.

4.1.4 Conclusions

To conclude, we found that large, arene ligands attached to a linear Ca-O could be suitable for optical cycling. We propose a design strategy and an upper bound on molecular size for optical cycling with aromatic molecules. The cycling functionality of these large molecules is dependent on the size of the arene and its orientation with respect to the Ca-O center. As the arene ligand grows, its intrinsic HOMO-LUMO gap becomes smaller and encourages electronic state mixing with the states of the cycling center and vibrational mode mixing. These effects produce asymmetric ground and excited state potential energy surfaces and less diagonal FCFs. Extending arenes all the way to ovalene or graphene destroyed the clean electronic transition in this way, as the graphene edge states mixed with the electronic transition in CaO-graphene and the ligand LUMO switched with the metal LUMO in CaO-ovalene. An arene as large as coronene is predicted to be a successful host for the Ca-O optical cycling center, being the largest such ligand proposed to date.

Extensions to ligands of similar size is an ongoing investigation. Molecules that fail as OCC ligands will be flexible and allow the Ca-O bond and ligands to bend/rotate, such as long chains of saturated hydrocarbons, have strong electron-withdrawing groups close to the

metal, reactive unsaturated hydrocarbons not in a ring close to the metal, or have small HOMO-LUMO gaps. Small arene molecules work well as OCC ligands due to their large HOMO-LUMO gap, planar, rigid structure and low reactivity with the metal, but eventually the clean electronic transition will be disrupted if grown too large. Alternatively, a material that can be grown large and support an OCC is diamond, because it has a large band gap and is quite rigid, so it does not interact with the OCC [135]. This work was later experimentally realized in Ref. [142].

4.2 Fully Saturated Hydrocarbons as Hosts of OCCs

4.2.1 Introduction

Molecules which can be laser cooled and favor electronic transitions between only a few controlled, electronic states (optical cycling centers, or OCCs) are useful for the fields of quantum information processing, magnetic sensing and ultracold physics studies [134, 202–209]. Using trapped-ion hardware and theory from atomic physics, small molecules have been laser cooled and shown to exhibit these properties [16, 22, 89–91]. The success of these molecules relies on high Franck-Condon factors (FCFs), which in many cases is quite close to the vibrational branching ratios in these species [123].

In the past, trapping and laser cooling molecules larger than a few atoms seemed formidable due to an increase in the number of vibrational modes, therefore a likely increase in vibrational branching. This vibrational branching poses a threat to laser cooling of molecules for quantum information [10, 79–86], as it would require many more repump lasers than experiment can afford. Successful molecular candidates are those where the ground and excited state potential energy surfaces are highly parallel and their electronic transitions are within the Franck-Condon region. Early investigations into this bonding structure began with alkaline earth molecules bonding to hydroxide and rigid, electronegative ligands such as borohydride and cyclopentadiene [167, 210–212].

Previous work on optical cycling and laser cooling of molecules started with diatomics [21, 122], then M-O-H species (where M is the alkaline earth radical bonded to an oxygen) [17, 167] and recently, alkaline earth alkoxides, built upon an M-O-R scheme where R is a saturated hydrocarbon [92–95, 113]. However, which R ligands are suitable for these systems, *i.e.* what limitations there are on their size and chemical nature, remains an open research question. Previous successful candidates were found through guesswork, rather than guided design [93, 94]. Most recently, multivalent OCCs were explored which required different design principles than the M-O-R framework [213].

Our past work focused on introducing design principles for M-O-R OCCs. We proposed that it is possible to expand these saturated hydrocarbon ligands to much larger sizes, including diamond and cubic boron nitride. The M-O-R motif with such large R is still a good optical cycling candidate, due to the ligand's large band gap [135]. Additionally, we found that arenes could be suitable ligands for optical cycling groups (or quantum functional groups) so long as the arene's HOMO-LUMO gap is large enough to encapsulate the optical cycling transition [124, 214]. In this work, we aim to strengthen these design principles by investigating other possible organic ligands of varying size and degree of electron-withdrawing character which could work as optical cycling centers (OCCs) and emphasize how symmetry and ligand rigidity affects OCCs.

Additionally, we will probe the effect of substituents on these R ligands, motivated by our recent study on alkaline earth phenoxides serving as good OCCs [110, 125]. In particular, we showed we could strategically diagonalize FCFs by adding electron-withdrawing substituents onto the phenyl ring, enforcing closer geometries between ground to excited states and favoring fewer, more dominant vibrational modes contributing to off-diagonal decays. This was due to the M-O bond becoming progressively more ionic, because of the increased pull in electron density. While in aromatic systems the substituents operate through resonance, in this work, we show the effect still holds via induction, though to a weaker degree, in saturated R group ligands.

Design rules in this paper can be applied to a wide variety of open-shell molecules in which an increase in ligand complexity does not lower FCFs but rather outcompetes simpler molecules through built-in electronic effects.

4.2.2 Computational Methods

Molecule geometries were optimized with density functional theory (DFT) and time-dependent density functional theory for excited states (TD-DFT) at the PBE0-D3/def2-TZVPPD level of theory in Gaussian16 [101, 106–108]. An effective core potential (ECP) was used for the

Sr atom. Franck-Condon factors were then calculated using the harmonic approximation including Duschinsky rotations.

Previous theoretical studies on OCCs used Complete Active Space Self-Consistent Field (CASSCF) and Multireference Configuration Interaction (MRCI) methods to produce highly accurate results [96–100]. However, scaling is poor with system size. Hence, cheaper methods must be applied for large molecular screening. Here, we find DFT/TD-DFT methods are a suitable alternative, within a margin of error, when picking the functional and basis set carefully.

In previous work, we compared CaOH, SrOH geometries and vertical excitation energies calculated with CAS/MRCI, TD-DFT and experimental data [110, 125]. At the PBE0-D3/def2-TZVPPD level of theory, TD-DFT-based bond lengths deviated from experimental values by less than 0.02 Åfor both ground and excited states, while the computed CAS/MRCI bond lengths are 0.06 Ålonger than the TD-DFT values. For larger molecules, such as CaOPh and CaO1Nap, our level of theory was benchmarked to experiment and found vertical excitation energies to be within 0.08 eV of experiment (see Table S1 in Ref. [124] for details) [125, 214]. Overall, we find DFT a suitable alternative to more expensive methods for predicting FCFs for these species, particularly when chemical trends are of interest more than the absolute accuracy and will use it throughout this work.

4.2.3 Results and Discussion

First, we explore the saturated hydrocarbon manifold for increasingly larger R group ligands. The R group can extend to a larger size so long as the ligand structure is rigid and spatially separated from the metal. A related requirement is the local linearity of the M-O- motif, to prevent the metal radical from bonding to parts of the molecular host. Lastly, the ligand must have a larger HOMO-LUMO gap than the metal-to-metal OCC transition and fully enclose the it, *i.e.* have the intrinsic HOMO of R below the M-based HOMO of M-O-R and the intrinsic LUMO of R above the M-based LUMO of M-O-R [124].

We investigated these limits in more detail. We found that unsaturated non-aromatic hydrocarbons are poor ligands and will fail because their π-system is much more reactive and will interact with the metal or oxygen, disrupting the clean metal-metal transition. For example, as seen in Figure 4.7, on the HOMO of the ethenyl- or ethynyl- containing derivatives, the metal s and p orbitals mix with the O p orbital as well as the C-C π orbital, indicating that the molecules are less ionic. The LUMO is dominated by the metal p and d orbitals. Thus, we expect the electronic transitions to couple to the molecular vibrations, giving rise to less diagonal FCFs. Similar bonding and orbital mixing have been observed in M-O-R with the -N_2H ligand. In the most stable geometry of the ground electronic state, the metal will bind to the O atom and the N-N π bond near the metal, featuring charge density delocalization with the ligand.

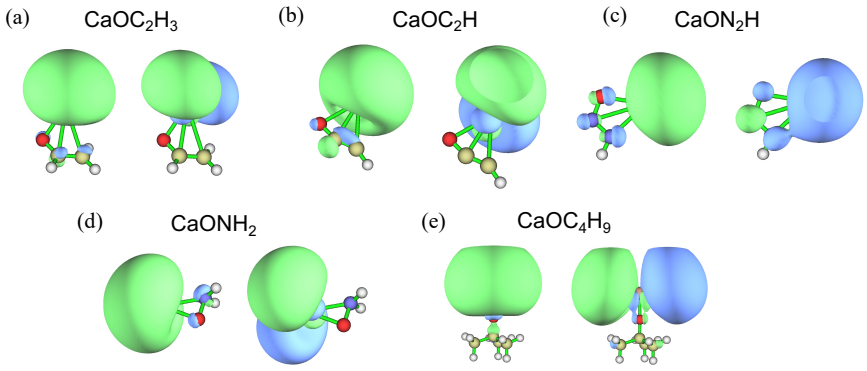

Figure 4.7: Highest occupied molecular orbitals (HOMOs) and lowest unoccupied molecular orbitals (LUMOs) for poor OCC candidates.

Additionally, we find that even if a structure is locally linear, such as $CaOC_4H_9$ which was previously confirmed experimentally [167], it could still be a poor candidate for optical cycling. In this case, the R ligand is too flexible and the states on Ca have an overlap with the R ligand such that the excited states have electron density on the CH_3 groups. This coupling produces a quartic well in which there are two local minima on the excited state (see Figure S1 in Ref. [139]). As a result, the diagonality of the ground to excited state transition is lost.

Contrastingly, a molecule of the same C_{3v} symmetry as $CaOC_4H_9$, CaO-adamantane, appears to be a good candidate for optical cycling. This is due to the ligand rigidity which prevents ligand-Ca interaction. Our calculations show that the electronic HOMO $\rightarrow$ LUMO transition in CaO-adamantane is quite isolated on the metal, as seen by the Natural Transition Orbitals (NTOs) in Figure 4.8. The natural population analysis (NPA) of the charge populations are 0.838 for Ca and -1.069 for O for the ground state. The transition orbitals resemble unhybridized s and p orbitals which are seen in the gas-phase atomic Ca^+ ion, further supporting the promise to use this molecule in optical cycling.

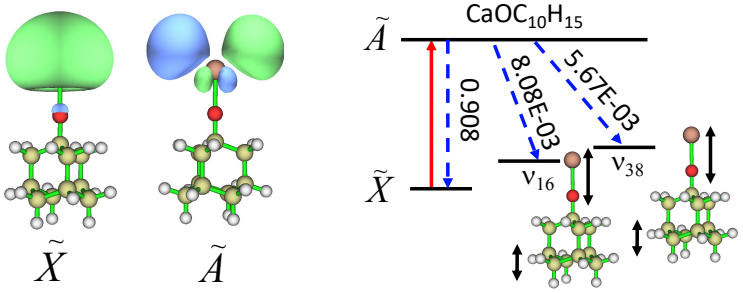

Figure 4.8: Natural transition orbitals (NTOs) for $CaOC_{10}H_{15}$'s ground ($\tilde{X}$) to 1st ($\tilde{A}$) excited state transitions. Orbitals generated with an isosurface value of 0.03. Excitation (red) and most dominant vibrational decays (blue) are shown, along with their associated Franck-Condon factors.

The largest geometry change is the Ca-O bond length. Ca-O-C is linear for these molecules in the $\tilde{X}$ and $\tilde{A}$ states. The Ca-O bond length change from the $\tilde{X}$ state to the $\tilde{A}$ state is 0.023 Å in CaO-adamantane.

As seen in Figure 4.8, the most dominant off-diagonal decays for CaO-adamantane are dominated by stretching motions. We speculate CaO-adamantane is a more successful candidate than $CaOC_4H_9$ because, despite the same symmetry, the large mass and rigidity of adamantane encourages the vibrational stretching motion, instead of the more flexible C_4H_9, which encourages CH_3 bending motions and mixes the metal Ca with the CH_3 groups, disrupting the isolated electronic transition.

Although the FCF for CaO-adamantane (0.908) is worse than a those of M-O-Rs with

certain smaller ligands, such as benzene (0.933 [125]), the transition is not destroyed. In fact, it has a better FCF than smaller molecules, such as $CaOC_2H_5$ (< 0.90 [215]) and $CaOCH(CH_3)_2$ (0.720 [138]), despite an increase in the number of vibrational modes. This suggests that an increase in ligand complexity in some cases outcompetes simpler molecules, paving the way for future, larger optical cycling centers.

In summary, saturated hydrocarbon molecules with large HOMO-LUMO gaps can be appended as ligands to alkaline earth oxides and still allow the M-O motif function as an optical cycling center. As long as the ligand remains rigid, a large increase in a molecule's complexity can still produce a similar or better Franck-Condon factor than a smaller molecule. Additionally, symmetry is an important consideration for optical-cycling-center design. Unsubstituted CaO-adamantane has C_{3v} symmetry. However, as we will show, substituting hydrogens can reduce the symmetry and in some cases boost FCFs, if the substituted groups are electron-withdrawing.

FCFs can also be altered by substituting electron-donating or electron-withdrawing groups. Previously, we showed electron-withdrawing groups improved FCFs through resonance interactions but the strength of this effect or the design rule for fully saturated hydrocarbons remains unexplored [110, 125]. Here, we find that substituting electron-withdrawing groups increases FCFs inductively, through σ-bonding effects and makes the Ca-O bond more ionic. Contrastingly, substituting electron-donating groups decreases FCFs. We demonstrate this by substituting CaO-adamantane, replacing three, five and eight hydrogen atoms at a time, in different positions, as shown in Figure 4.9. We also expand the scope toward SrO-variants (previously shown to have systematically less diagonal FCFs compared to CaO-phenoxides [110]).

Adding electron-withdrawing groups to both CaO- and SrO-adamantane increases FCFs through σ-bonding effects, making the Ca(Sr)-O bond more ionic, as can be seen from NPA charges on the Ca(Sr) and O atoms (see Tables 4.3 and 4.4, ordered according to the electron-withdrawing/donating strength of the substituents). While adding electron-withdrawing

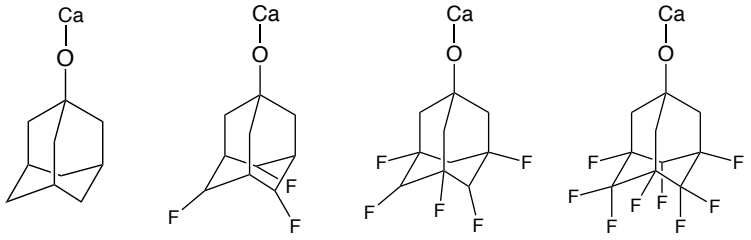

Figure 4.9: Molecules decorated with optical cycling motifs that are considered in this substitution study. From left to right: CaO-Adamantane, CaO-3F-Adamantane, CaO-5F-Adamantane and CaO-8F-Adamantane.

groups reliably increases the ionic character of the M-O bond, the corresponding increase in the FCF does not fully follow the trend, suggesting another factor besides bond ionicity at play, as was also noticed by Ivanov *et. al.* [94]. For example, the FCF increases up to 5F/5Cl subtitution, but decreases for 8F/8Cl substitution. This is due to vibrational mode effects discussed next.

Substituent for H	FCF	CaO-Change (Å)	Charge (Ca)	Charge (O)
$3NH_2$	0.885	-0.0226	0.9578	-1.1335
(none)	0.908	-0.0234	0.9545	-1.1458
3Cl	0.929	-0.0201	0.9610	-1.1190
3F	0.928	-0.0203	0.9599	-1.1230
5Cl	0.939	-0.0186	0.9622	-1.1119
5F	0.939	-0.0188	0.9607	-1.1157
8Cl	0.914	-0.0175	0.9655	-1.1037
8F	0.913	-0.0168	0.9631	-1.1066

Table 4.3: Calculated FCFs, including Duschinsky rotations, bond-length changes from excited-ground state and NPA charges of Ca and O atoms for various substituted CaO-adamantane ligands.

For both CaO-adamantane and SrO-adamantane, the behavior of the vibrational modes

Substituent for H	FCF	SrO-Change (Å)	Charge (Sr)	Charge (O)
$3NH_2$	0.872	-0.0231	0.9694	-1.1320
(none)	0.873	-0.0238	0.9710	-1.1363
3Cl	0.890	-0.0211	0.9727	-1.1177
3F	0.898	-0.0214	0.9715	-1.1223
5Cl	0.914	-0.0203	0.9736	-1.1106
5F	0.915	-0.0203	0.9722	-1.1150
8Cl	0.889	-0.0195	0.9770	-1.1020
8F	0.895	-0.0187	0.9748	-1.1054

Table 4.4: Calculated FCFs, including Duschinsky rotations, bond-length changes from excited-ground state and NPA charges for the Sr and O atoms, for various substituted SrO-adamantane ligands.

are similar (see Fig. 4.10 and Fig. 4.11, respectively). Figure 4.10 shows the diagonal FCF and the largest two off-diagonal FCF leakage pathways for unsubstituted CaO-adamantane and all fluorine substitutions investigated (3F, 5F, 8F). The off-diagonal FCF in CaO-adamantane is dominated by two vibrational modes, v_{16} the Ca-O symmetric stretch and v_{38} the Ca-O-C asymmetric stretch. As more electron-withdrawing substituents are added up to 5F/5Cl, the diagonal FCFs increase. In 8F-substituted CaO-adamantane, the bending mode (v_2) dominates and contributes on par with the symmetric stretch (v_9) that involves the motion of the ligand. As more electron-withdrawing groups are placed on the molecule, the M-O stretch motion is more coupled with the ligand motion. We hypothesize this coupling helps increase FCFs to a certain extent through symmetrizing the excited and ground state surfaces as in the case of 3F and 5F, but then too many withdrawing substituents encourage Ca-O bending motion, disrupting the dominant stretch PES and decreasing FCFs.

For SrO-adamantane, the picture is similar but slightly different (Fig. 4.11). The bending

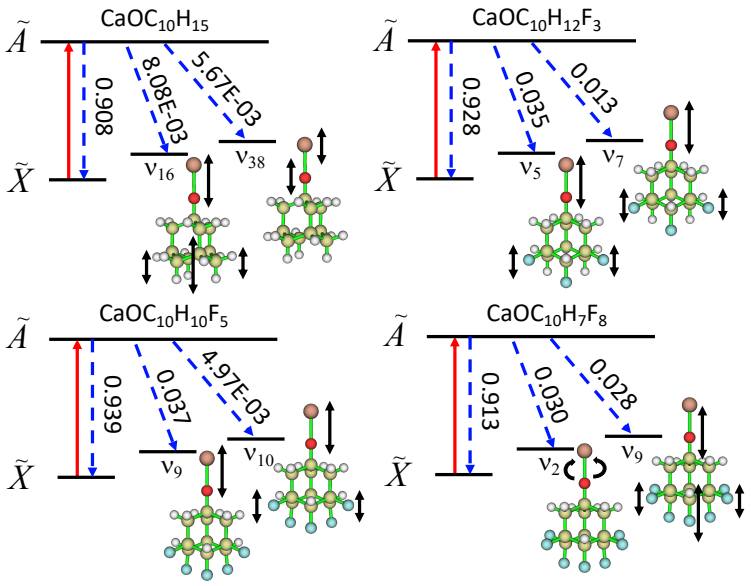

Figure 4.10: Excitation (red) and most dominant off-diagonal vibrational decays (blue) associated with each Franck-Condon factor for (top left to right): unsubstituted CaO-adamantane, 3F-CaO-adamantane, 5F-CaO-adamantane and 8F-CaO-adamantane.

mode, v_2, is always a dominanat off-diagonal decay, which decreases as substituents are added up to 5F, then reappears in 8F, which decreases FCFs. We speculate this bending mode is more pronounced in Sr than Ca due to Sr's heavy mass changing the potential energy surface landscape. Our calculations also lack spin-orbit coupling, which is also more pronounced in the Sr atom (though our theory was recently demonstrated to still predict Sr OCC trends in SrOPh [143]).

Overall, these trends in FCFs can be used as a guide to predict optical cycling success; since they are less than ≈ 0.99, they can be approximated as the vibrational branching ratio.

4.2.4 Conclusions

In summary, we demonstrate a direction for constructing larger R ligands, suitable for hosting quantum functional groups, Ca-O- and Sr-O-, for optical cycling. Carbon-containing ligands (especially saturated) appear to be the most promising so far, due to their stability

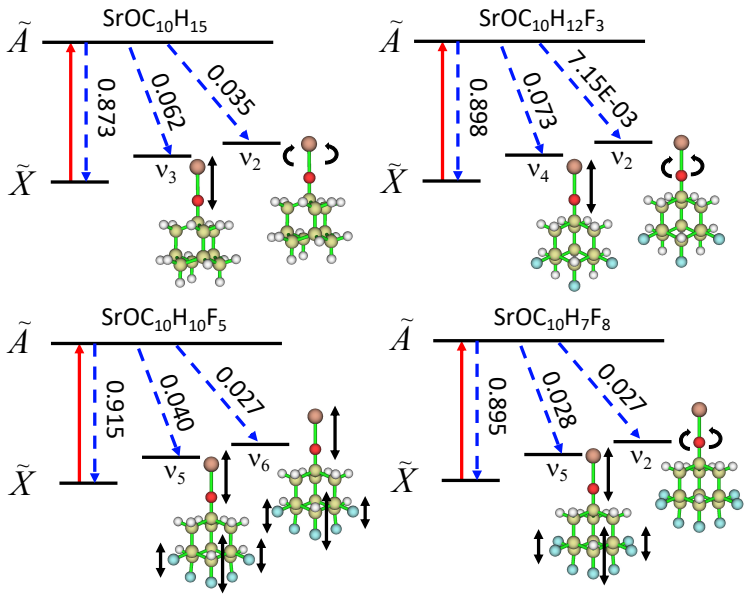

Figure 4.11: Excitation (red) and most dominant off-diagonal vibrational decays (blue) associated with each Franck-Condon factor for (top left to right): unsubstituted SrO-adamantane, 3F-SrO-adamantane, 5F-SrO-adamantane and 8F-SrO-adamantane.

and large separation of bonding and antibonding states, away from the HOMO-LUMO OCC excitation. Moreover, adding electron-withdrawing substituents is shown to further increase FCFs via induction. Lastly, symmetry and behavior of vibrational modes play an important role in controlling the diagonality of the OCC FCF. Specifically, lower symmetry decreases FCFs but substituents can change dominant mode behaviors in electronic decay pathways. For our M-O-adamantane species, in which we design the M-O stretch to be the most dominant decay channel, electron-withdrawing substituents encourage ligand coupling to the M-O stretch mode, which symmetrizes the ground with the excited state potential energy surfaces, increasing FCFs, until electron-withdrawing effects overpower the PES symmetrizing benefits and encourages bending motions which disrupt the transition. As a result, we can design larger molecules to have higher FCFs than smaller molecules, despite an increase in complexity.

CHAPTER 5

Multiple OCCs on Surfaces, Larger Structures

5.1 Surface chemical trapping of OCCs

5.1.1 Introduction

Quantum information processing (QIP) is currently in a stage of parallel exploration of multiple platforms. Much like classical electronics, large-scale QIP will require approaches that are amenable to miniaturization and scalability. Along these lines, it seems fitting to approach building a quantum device (sensor, simulator, computer, etc.) by utilizing the natural scale at which quantum effects are important; for electrons at room temperature, this means the energy and size scale of single atoms. In contrast to larger systems that currently dominate the QIP landscape (such as superconducting qubits [216] and phonons in trapped ion Coulomb crystals [217]), working at the nanometer scale has the potential advantage that inter-qubit coupling can be significantly stronger at short range, leading to systems that require less cooling to access pure collective states. However, single-atom-engineering at nanometer length scales is most naturally accomplished by chemically bonding the atoms to molecular hosts and using chemical (as opposed to mechanical) assembly. Chemical methods will therefore likely play a major role in development of quantum systems built from single molecular qubits.

Here, we present a new concept for molecular qubits that are designed to be scalable and packed at high density via surface modification, potentially produced by self-assembly of organic molecules. By attaching an optical cycling qubit moiety to a chemically defined

crystal surface, we combine initialization and state readout based on optical cycling that trapped atoms provide, with the potential for the nanoscale lithographic control that surfaces furnish. In this way, this "chemically-trapped ion" platform borrows strengths from both gas-phase and solid state devices in an effort to build a concept that can leverage the best features of each for building the next generation of quantum devices.

Recent successes in the laser cooling of molecules forms the basis of our design [16, 89, 90]. That work demonstrated that many photons can be spontaneously emitted by repeatedly laser-exciting optical transitions from polyatomic molecules without partitioning into excited molecular vibronic states. Common in these systems are "functional groups" based on a metal atom that acts as an optical cycling center (OCC) [92]. The primary feature of an OCC is an atom-centered optical electronic transition with a near-zero Franck–Condon overlap for transitions that change its vibrational state. In this system, successive excitation and spontaneous emission from the OCC can result in a reduction of entropy as the internal state of the molecule is cooled, allowing for quantum state preparation (including laser-cooling) and readout. The workhorse of this process is typically alkaline-earth-metal alkoxide groups (M-O-R) in which a radical valence electron centered on the alkaline earth serves as the handle for state preparation and measurement (SPAM).

Our calculations suggest that increasing the size and complexity of the ligands may slightly disrupt the closure of the optical cycle. However, the size and complexity effects may be small and can be compensated by additional repumping lasers, if the ligand is spatially and electronically separated from the OCC [92]. This raises the possibility that an OCC can be chemically tethered to a substrate in vacuo while retaining its ability to spontaneously emit a series of photons upon state-selective excitation, providing readout of the initial internal quantum state of the molecule.

Beyond OCCs' roles in supplying isolated transitions in the molecules, they also provide a natural basis for storing and using quantum information. A quantum state stored in a pair of long-lived sublevels of the electronic ground state (such as hyperfine structure) serves as

a qubit and a state-selective optical cycle would allow excitation of only one of these qubit eigenstates (the "bright state") for laser-induced fluorescence, while the other eigenstate (the "dark state") would not emit photons. Lack of collected fluorescence therefore constitutes detection (and heralds preparation) of the dark state, while detection of fluorescence indicates the bright state. As such, the optical cycling property allows SPAM of the molecular qubit, in a scheme analogous to those used in trapped-ion quantum computers [19, 20].

Taken together, the possibility that OCCs might be realized on surfaces and even patterned to produce multi-OCC interactions argues for a theoretical treatment of whether molecules hosting optical cycling centers can be attached to surfaces while retaining both chemical and physical properties. We approach this by expanding on the complexity of alkyl chain R-groups that are amenable to optical cycling. For strontium (Sr) as our example of an alkaline earth metal, we suggest that diamond and cubic boron nitride (cBN) may serve as a good substrate for OCC anchoring and derive some general trends. We then explore how multiple OCCs may interact chemically or spectroscopically on a surface. We close by speculating on several schemes by which surface bound OCCs may provide next generation quantum systems through nanoscale control and patterning.

5.1.2 Computational Methods

We first probed the electronic structure of the smallest molecular emitters using MRCI/CASSCF (9 electrons/10 orbitals active space) with the def2-TZVPPD basis set [108]. The geometries were optimized using the state-averaged CASSCF method (three lowest-energy states with weights 0.8/0.1/0.1 for the ground state and 0.2/0.4/0.4 for the first excited state given its near-degeneracy) and MRCI method was used to calculate electronic excitation energies in Molpro [43, 48, 49, 51]. These results were used to benchmark the performance of the Density Functional Theory (DFT) and Time-Dependent DFT (TD-DFT) methods [102–105] implemented in the Gaussian 16 package [101], capable of probing larger molecular systems. We show the comparison between DFT and MRCI/CASSCF for the geometries and excita-

tion energies in Table S1 in Ref. [135]. We found the PBE0 hybrid functional with the D3 dispersion correction yielded the most reliable DFT-based results [106, 107]. It is additionally known to work well for excited state calculations [218–220]. We also probed the effects of basis set size and functional (Table S2). DFT geometry optimizations were performed with the def2-SVPD basis set and a larger def2-TZVPPD basis set was used for excitation energy calculations. The effective core potential (ECP) was used for the Sr atom. The Franck–Condon Factors (FCFs) are calculated within the double-harmonic approximation using ezSpectrum [109].

Geometry optimizations of OCCs bound to surfaces were performed using the PBE functional [189] with the projector augmented-wave (PAW) potentials [194, 195], implemented in the DFT-based Vienna ab initio simulation package (VASP) [185–188]. The hybrid functional HSE06 [190] was used for single point energy calculations, density of states calculations and Bader charge analysis [191, 192]. HSE06 has been extensively benchmarked against other functionals and performs well in predicting band gaps that fall within 1-5 eV [221, 222]. A $1 \times 1 \times 1$ Monkhorst–Pack k-point grid centered at Γ-point and a plane-wave cutoff energy of 400 eV are employed, with a convergence criterion of 10^6 eV for the SCF relaxation. The k-point grid is considered sufficient due to the large size of the unit cell and the significant separation between OCCs that we probe, expected to produce flat bands, accurately modeled with just the Γ-point calculation. A five-layer 2×2 supercell with the exposed (110) facet, in periodic boundary conditions, represents the cubic diamond surface as an infinite slab, in which the two surfaces are covered with H atoms. In this supercell 160 C atoms in total, of which 64 are surface-exposed (or 32 per face), all capped with H before SrO deposition. The dimensions of the supercell are 14 Å $\times$ 14 Å $\times$ 20 Å, which we found to be sufficient to prevent the interaction between the periodic images. The top-three layers of C atoms and the surface H atoms are relaxed during the geometry optimizations. The optimizations are considered converged when the residual forces are less than 0.01 eV per atom.

5.1.3 Results and Discussion

We start from the hypothesis that the alkyl group R, in SrOR, can be increased beyond methyl, CH_3. We apply the TD-DFT method to a series of SrOR molecular radicals, R, with increasing numbers of carbon atoms, CH_3, C_4H_9, $C_{13}H_{21}$ (Fig. 5.1). Our goal is to progressively build up to the local structure of a diamond surface. We focus on the changes in geometries within the SrO part of the molecular radicals in the ground and first excited states, the excitation energies and the Frank–Condon factors, FCFs. All the cluster models can maintain a local linear structure, with the Sr–O–C angles of 179.8°-179.9° for the ground state and 179.6°–180.0° for the excited state. This bond angle is characteristic also of SrOH and suggests a strongly ionic bond character between Sr and the O atom. As shown in Table 5.1, the two states in these models are aligned within 0.02–0.03 Å in terms of the equilibrium Sr–O bond length and larger R sizes correspond to slight deviations from the linear character.

Molecule	Δr_{Sr-O} (Å)	ΔE (eV)	FCF
SrOH	-0.017	1.750	0.9651
$SrOCH_3$	-0.018	1.754	0.9556
$SrOC_4H_9$	-0.021	1.738	0.9163
$SrOC_{13}H_{21}$	-0.029	1.721	0.7819

Table 5.1: Electronic excitation properties for SrOR. Δr_{Sr-O} is the Sr–O bond length change from the ground state to the first excited state ($\Delta r_{Sr-O} = r^{ex}_{Sr-O} - r^{gs}_{Sr-O}$), ΔE is the computed vertical excitation energy and FCF is the Franck–Condon factor for the decay transition from the first excited state to the ground state. The initial and target states are vibrational ground states

The three cluster models exhibit similar charge distribution on the Sr and O atoms from the natural population analysis (NPA) [223], due to the similar electron withdrawing strength of the alkoxide groups bound to Sr. The natural transition orbitals (NTOs) in all cluster-bound SrO have the same shape as those in SrOH, with electron density localized on the Sr

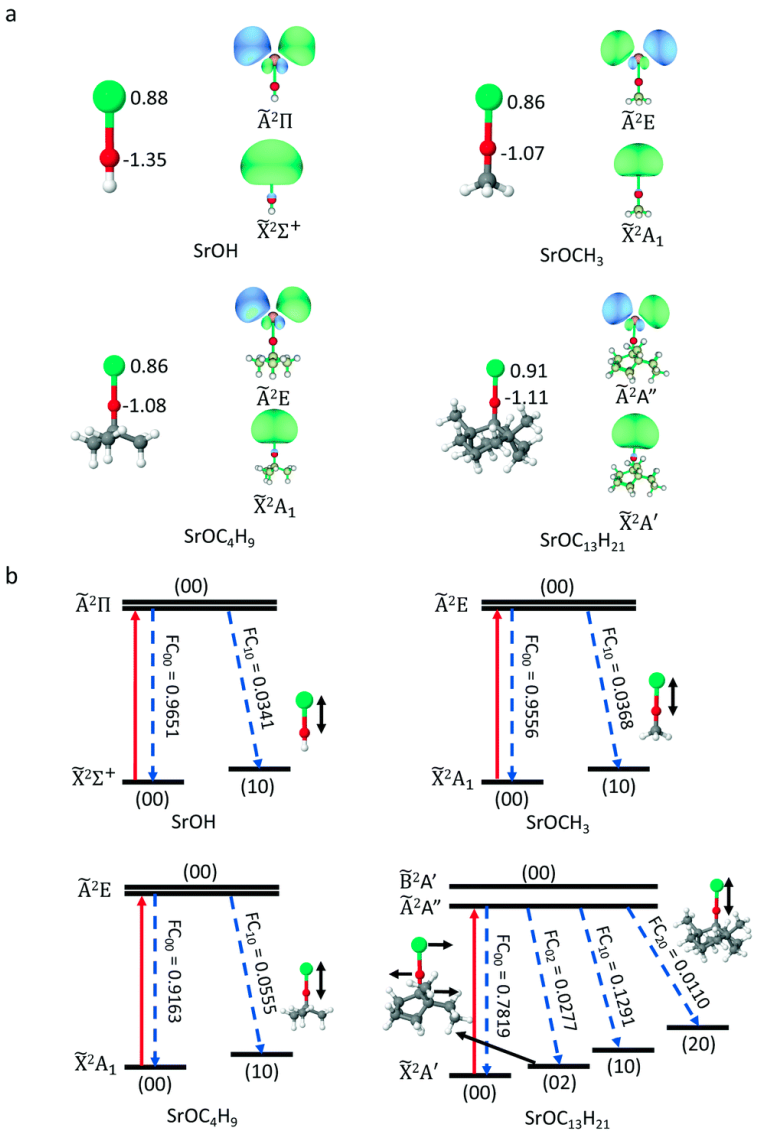

Figure 5.1: (a) Optimized ground-state geometries of SrOR. Atomic charges on the Sr and O atoms, computed from NPA, are also shown in the left side of each sub-figure. The right side of each sub-figure shows the NTO for particle orbitals and hole orbitals. The isosurfaces are plotted with an isovalue of 0.03. (b) Photon cycling scheme for SrOR. Excitation from the ground state to the first excited state and spontaneous decay channels are shown with upward red arrows and downward blue dashed arrows. The FCFs are shown along with each decay. The vibrational quantum numbers (v_1v_2) correspond to the Sr–O stretching (v_1) and Sr–O–C bending (v_2) modes.

atom (Fig. 5.1). This suggests that the perturbation from the R group is minor. However, we observe that as the cluster size increases, a small amount of electron density appears on the O atom and some on the C atoms, which will make the potential energy surfaces (PESs) of the ground ($\tilde{X}$) and first excited ($\tilde{A}$) states, less parallel and thus the FCF less diagonal (deviating more from the highly diagonal FCF in SrOH [16]). This is because more modes are contributing to the off-diagonal FCFs. In addition, the contribution from the Sr–O stretching mode is slightly increased, consistent with our observation that the Sr–O bond length change is increased and thus the PESs of the two states are less parallel along this mode as we move to larger model systems. However, the decrease in FCF, due to the size effect, is not significant and SrO will still have a reasonably good FCF. Note as well that the diamond-supported system will have a very different reduced mass.

In $SrOC_{13}H_{21}$, there is a very small amount of electron density on the two C atoms that are not directly bound to O, but are only 2.7 Å apart from the O atom. These carbon atoms will conform to the top-layer atoms on the diamond surface, which are 2.9 Å away from O in Fig. 5.2. Consistently, we find that the distance between the O atom and these C atoms changes by 0.004 Å from the $\tilde{X}^2$A' to the $\tilde{A}^2$A" state and that constitutes the second largest geometric changes in $SrOC_{13}H_{21}$. Therefore, when the cycling center is deposited onto the diamond surface, the orbitals of these two C atoms may have weak couplings to the O and Sr atoms and affect the FCF. On the other hand, the chemical nature of these atoms in the diamond surface is not identical to that in a finite hydrocarbon and thus, this small involvement of the C atoms of the $C_{13}H_{21}$ system in the key transition does not necessarily preclude the possibility of the infinite surface to be a viable OCC platform.

The TD-DFT calculations show that the first vertical excitation energy is slightly decreased as the size of the R group increases (Table 5.1), agreeing well with previous experimental measurements [167]. Given this trend, the diamond-bound SrO is expected to have slightly lower excitation energy than SrOH.

Encouraged by the FCFs observed so far in small clusters, we now expand the R group

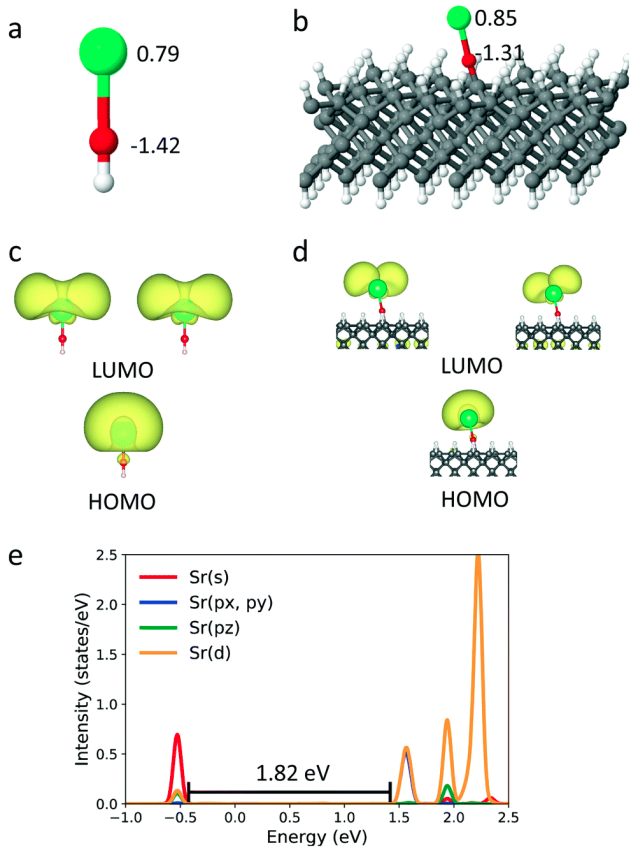

Figure 5.2: (a and b) Optimized geometries of the gas-phase SrOH molecule and the SrO-group bound to the diamond surface. The green, red, gray and white colors represent the Sr, O, C and H atoms, respectively. The atomic charges on Sr and O from the Bader charge analysis are also shown . (c and d) Electron density of the HOMO and LUMO of the SrOH molecule and the SrO supported on diamond. The isosurfaces are plotted with an isovalue of 0.001. (e) PDOS, indicating the excitation energy distance.

to encompass the full diamond surface. We first explore the ground state structure of SrO bound to diamond and compare it to the gas-phase SrOH radical, which is known to have a diagonal FCF. The Sr-Sr separation afforded within this supercell is 14.27 Å. When the SrO group is bound to the surface, the Sr–O–C unit can maintain a roughly linear geometry (Fig. 5.2), with an angle of 175.2°. The sp^3-hybridized C atoms encourage a tilted Sr–O–C unit with respect to the surface normal and the unit thus experiences unbalanced forces

from the two sides of the surface, giving rise to the small bend angle. However, this small bending does not affect the extent of density localization on HOMO and LUMO and will not affect the FCF. The ground-state Sr–O bond length is 2.125 Å on the diamond surface, *i.e.* 0.019 Å longer than that of the gas-phase SrOH molecule. The atomic Bader charge on Sr within the surface-bound SrO (Fig. 5.2(a and b)) is 0.85 e, similar to that in SrOH and nearly identical to those seen in $SrOCH_3$ and $SrOC_4H_9$ (Fig. 5.1), indicating an unpaired electron localized on the cycling center. The overall resemblance of the surface-bound SrO to the best cycling molecules suggests that optical efficient cycling should still be possible at this limit.

Fig. 5.2(c and d) show the electron density of the highest occupied molecular orbital (HOMO) occupied by the unpaired electron and the doubly-degenerate lowest unoccupied molecular orbital (LUMO) of the SrOH molecule with the SrO group attached to diamond. For both the HOMO and LUMO of the surface-bound SrO, a majority of electron density is localized on Sr, leading to electronic transition localized on the cycling center. Again, the molecular orbitals of the surface-bound SrO have similar shapes to those of the SrOH radical, suggesting similar distributions of atomic orbital characters. For SrOH in the $\tilde{X}^2\Sigma^+$ state, the orbital occupied by the unpaired electron is dominated by the Sr s character with the remaining contribution from the Sr p orbital, whereas for the $\tilde{A}^2\Pi$ state, the Sr p and d orbitals dominate the molecular orbital character. Given the similarity in geometry, charge distribution and shapes of the HOMO and LUMO between the diamond-surface-bound SrO and the SrOH molecule, we expect SrO to maintain its excitation properties once bound to the diamond surface. We can roughly estimate the excitation energy from the projected density of states (PDOS) (Fig. 5.2e) to be 1.82 eV for diamond-bound SrO, close to the excitation energy in SrOH (1.83 eV). While the number derived from PDOS is not necessarily approximate, the HSE06 functional is known to be quite reliable for the optical gap, as discussed above. Calculating the FCF for the infinite surface is currently technically intractable and thus, our results are a proposal, substantiated as best as currently possible.

Confirming this requires experimental validation or theory method development.

Next, we believe there is a rational way to improve the properties of the surface-bound SrO, through changing the support to a close diamond analogue, cubic boron nitride (cBN). cBN has the same number of valence electrons and the same crystal structure as the cubic diamond and thus, mirrors diamond's properties. However, it additionally features a small amount of charge transfer between B and N. Given that the surface of cBN is expected to be B-terminated and that SrO- would therefore bind to the boron, the intra-crystal polarization is expected to effectively create a more electron-withdrawing ligand, R, for SrO–. Fig. 5.3 shows the optimized structure for SrO–cBN from periodic DFT calculations. The Sr–O bond is 2.104 Å on cBN, *i.e.* 0.021 Å shorter than that on diamond. The Sr–O–B can maintain a linear structure near Sr, with a now-perfect angle of 180.0°. In line with this finding and our hypothesis regarding cBN, the Sr atom has more positive charge on cBN than that on diamond. The HOMO and LUMO of this system (Fig. 5.3) are the expected singly-occupied states, very similar to those of SrO– on diamond and SrOH in the gas phase. From the PDOS, the excitation energy of SrO– on cBN is 1.70 eV. Thus, we see that the behavior of OCC is likely again preserved on cBN at this low coverage. While the experimental confirmation of the OCC behavior on both surfaces is warranted, our results suggest that both diamond and cBN could be used to support the SrO– cycling radical centers and cBN has a potential to be a superior support.

Finally, the interactions and entanglement between the optical cycling centers would be affected by their spatial separation. The surface allows for certain control of it, since the affordable separations are multiples of the surface lattice constant. We explore the effect of surface coverage on the properties of the cycling centers. First, we have studied the interactions between the SrO– groups when they are uniformly distributed on diamond, by changing the size of the periodic supercell. The structure in Fig. 5.2 corresponds to a coverage of 1/32 monolayer (ML) and it was chosen specifically to avoid the interactions between the Sr centers in the neighboring unit cells. Below we address what happens if

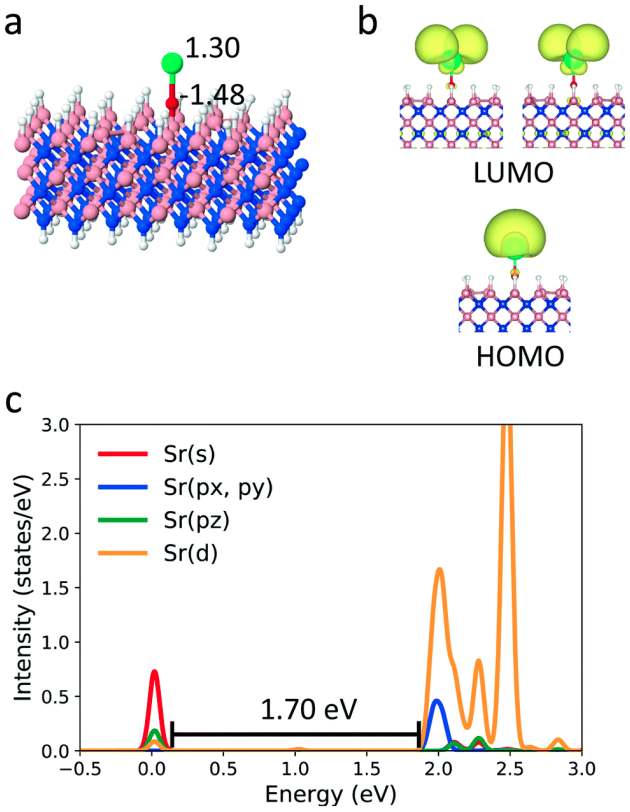

Figure 5.3: (a) Optimized geometry of the SrO– group bound to the boron nitride surface. The green, red, pink, blue and white colors represent the Sr, O, B, N and H atoms, respectively. The atomic charges on Sr and O from the Bader charge analysis are also shown. (b) Electron density of the HOMO and the LUMO of the SrO– supported on cBN. The isosurfaces are plotted with an isovalue of 0.001. (c) PDOS, indicating the excitation energy distance.

coverage increases to 1/8 or even 1/2 ML.

When the cycling center coverage is 1/2 ML, Sr will bind to two O atoms, with bond lengths of 2.33 Å and 2.39 Å, respectively (Fig. 5.4). The distance between the two Sr centers is 3.57 Å. The HOMO and LUMO are completely delocalized, where the adjacent Sr radical orbitals mix, effectively forming a half-filled σ-band. When the coverage is 1/8 ML, corresponding to the distance between the two cycling centers of 7.13 Å, the Sr–O–C unit can maintain the locally linear structure. However, the orbitals of two neighboring Sr atoms still interact with each other, either polarizing the original orbitals or mixing and splitting

into two mixed states.

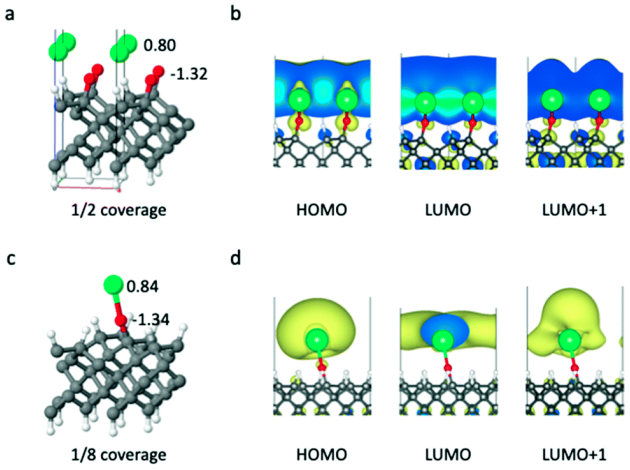

Figure 5.4: (a and c) Optimized geometries for SrO-diamond with the cycling center coverage of 1/2 and 1/8. Two unit cells are shown for the case of 1/2 coverage. (b and d) Electron density of the HOMO, LUMO and LUMO+1 for different coverages of cycling centers. The isosurfaces are plotted with an isovalue of 0.001.

We have also studied the systems where two SrO– units are in the same unit cell and can form dimer geometries. In some cases, one Sr will bind to two O atoms, similar to that in Fig. 5.4(a), while in other cases the two SrO– groups can maintain the locally linear structures, but their orbitals interact with each other. Fig. 5.5 shows one case where the distance between two Sr is 3.73 Å and the distance between the two C atoms that the SrO– groups are bound to is 1.71 Å. The two Sr *s* orbitals with the same energy form a bonding and an antibonding combinations, while the doubly degenerate *p*- and *d*-type orbitals from different Sr form even more mixed orbitals. The charges on the Sr atoms also suggest that they are not chemically identical.

Clearly, these coverages are too high to maintain the clean radical character of the cycling centers in the ground and excited states. Our results indicate that the surface coverage with radical center has to be certainly lower than 1/8 ML, in order for the cycling centers to maintain their local electronic character and the diagonal FCF.

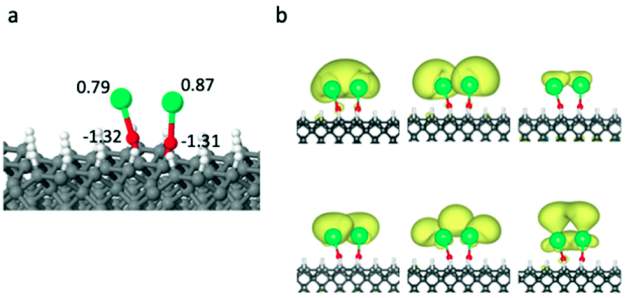

Figure 5.5: (a) Optimized geometry for two cycling centers on the diamond surface. The atomic charges on Sr and O from the Bader charge analysis are also shown. (b) Electron density for 6 low energy orbitals. The isosurfaces are plotted with an isovalue of 0.001.

5.1.4 Conclusions

In this contribution we showed that the SrO- radical cycling center can be attached to R groups as large as the diamond or cBN surface. Surface patterning with such centers allows for spatial control and alignment. The coverage of the surface with the cycling centers cannot be very high, to prevent their chemical interaction with each other (as seen at 1/2 ML), or mutual electronic perturbation (as seen at 1/8 ML). Even though at 1/8 ML the geometries of the SrO– units are linear, their electronic states can still mix, particularly on the excited state. Furthermore, our results suggest that the surfaces that can successfully host radical cycling centers must feature large band gaps, such that the HOMO and LUMO of the radical are located safely within the gap and not mix with the states of the surface.

We hypothesize that surface-supported optical-cycling ligands can be realized through chemical functionalization of the surface. We propose that diamond grown by chemical vapor deposition (CVD) (which is typically H-terminated) can be functionalized with pendant hydroxide groups by low-pressure oxygen plasma treatment [224, 225]. Following this, reactive Sr can be prepared by exciting the Sr atoms to the metastable state $^3P_1$ [95, 210, 226]. To control the deposition, the amount of pendant hydroxide can be tuned by modulating the power and duration of the plasma treatment.

Fig. 5.6 shows three applications that would be enabled by the development of surface-bound, state-selective emitters. For sensing applications, Fig. 5.6(a) shows a conceptual arrangement whereby a single molecular qubit could be used for spatial imaging of, for instance, local magnetic fields by functionalizing the tip of a scanning tunneling microscope (STM) or an atomic force microscope (AFM). Light for SPAM can be delivered to and collected from the OCC via fibers or optical waveguides built into the tip. A superposition of field-sensitive qubit states will process at a rate determined by the local magnetic field and readout after free precession can be used to map the field at the atomic scale.

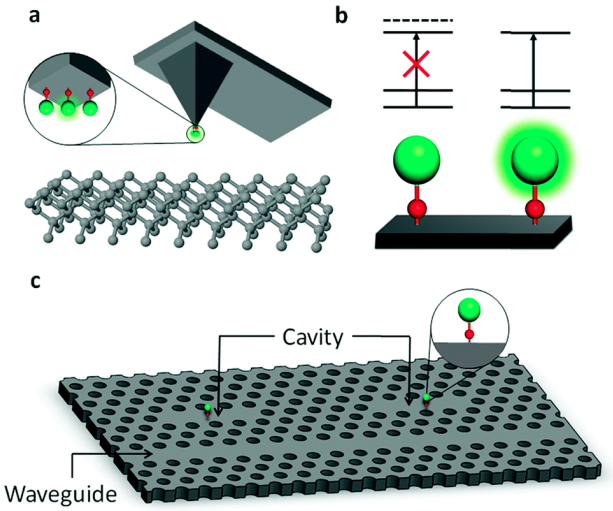

Figure 5.6: Applications of surface-bound OCCs (a) An AFM/STM tip can be functionalized with OCC centers, enabling precision quantum-enhance readout of local magnetic and electric fields through fluorescence. (b) Two OCCs in spatial proximity can provide the two qubit basis for a CNOT gate achieved through dipole blockade. (c) OCCs can be placed in a photonic waveguide, entangling two OCCs via photonic bus.

However, if AFM is conducted at ambient pressures, the Sr radicals are likely to chemically react with the gases and quench. For STM, the tip generates an oriented electric field, which at large enough magnitudes may affect charge separation and hinder Franck–Condon factors. Experimentally, an external electric field generated by STM was shown to stabilize or destabilize charge-transfer in organic molecules placed on gold surfaces, based on alignment.

The external electric field strengths ranged from -1×10^9 to 1×10^9 V m^{-1} [227].

To probe how external fields would affect optical cycling, we introduced electrical fields in two ways. A field between -1×10^{10} to 1×10^{10} V m^{-1} aligned with the Sr–O bond was applied to 1/32 ML Sr–O OCCs on diamond (see SI of [135]). In another case, a field of -1×10^8 to 1×10^{10} V m^{-1} was applied to two SrO– units located 3.88 Å apart and 10.39 Å from other OCCs on diamond (see SI of [135]). In both cases, larger electric fields reduced charge localization on Sr, while the Sr–O bond length would increase or decrease depending on the direction of the field. The effect on charge can be explained by the fact that the field pushes the full electron density in the system, affecting the bonding character on the ground and excited state beyond just the radical-centered HOMO and LUMO. We made a comparison of these results to the cluster model, $SrOCH_3$, with an external electric field applied along the Sr–O bond. As on the surface, the applied field led to charge delocalization and increase or decrease in Sr–O bond length, depending on the field direction. In both field directions, the ground versus excited state geometry difference increases with increasing field magnitude, implying poorer FCFs (see SI of [135]). Thus, in STM, large electric fields can adversely affect radical charge localization and FCF of OCCs.

In Fig. 5.6(b), two qubits in a quantum processor are shown performing a controlled-NOT (CNOT) quantum gate. Each qubit can be defined on a pair of long-lived internal states $|0\rangle$ and $|1\rangle$ (for instance, hyperfine levels) that have nearly identical electric dipole moments. Even so, inhomogeneities in the local surface features and attachment details are expected to result in strong (in the sense that they fully mix opposite parity states) static electric fields that are different at each qubit's location, which will lead to small shifts that produce a unique splitting for each qubit. This will allow individual addressing of single-qubit gates through frequency resolution of the applied resonant fields, with the size of the splitting required for resolution set by the available interaction time. State preparation is furnished by laser-driven optical pumping through the OCC.

For two-qubit operations, a third, long-lived state ($|0\rangle$) in each molecule that possesses

a large electric dipole moment (polarized by the local static field of its environment) can be utilized. Frequency resolution can be used to couple only one of the qubit states of any particular qubit to the auxiliary level, which will Stark-shift all of the auxiliary states of the qubits around it via the dipole–dipole interaction (any residual differential shift of the qubit states near the dipole, including the target qubit, can be removed through global dynamical decoupling). In this way, a dipole blockade CNOT gate [228], between any two qubits within a blockade radius of one another can be performed that does not depend upon their separation. State readout can likewise be performed using frequency-resolved addressing of each molecule's OCC.

Since the proximity of the qubits can be extremely close (but not closer than 1/32 ML on diamond, in our calculations) the energy scale (and therefore achievable speed) of the gate is expected to be high. For example, for 1 Debye dipoles, the 1 MHz blockade radius could contain about 1000 qubits at 1/32 ML packing. While the coherence properties of these qubits remain an open experimental question, the basic tools presented here show that there is no fundamental impediment to achieving universal quantum computation with this platform.

As a third example, Fig. 5.6(c) shows a photonic interconnect for large-scale processing based on surface-bound OCCs. Even qubits that are physically distant can interact strongly with one another due to their strong coupling to photonic cavities built from their substrates and classical routers can turn interactions between individual qubits on and off by optically connecting their photonic cavities together.

We examine the possibility of constructing pendant radical alkaline earth based OCCs on surfaces. Such structures may bridge surface engineering with the precise quantum control afforded by atomic physics. After validating our computational methods, we find that diamond and cBN could support SrO– based OCCs. We establish the necessary density of OCCs on a surface needed to retain independent electronic character and explore how they might be used in applications such as STMs, universal quantum gates, or as substrates for

quantum photonics. We believe this presents a path forward to realizing a novel quantum architecture experimentally.

5.2 Single-Molecule Superradiance for Optical Cycling

5.2.1 Introduction

We propose a strategy for improving the efficiency of laser-cooling large molecules by combining superradiant phenomena with optical cycling. Optical cycling centers (OCCs) are functional groups (also known as quantum functional groups, or QFGs) that feature closed transitions, typically electronic, where one can scatter on the order of thousands of photons without a change in other molecular degrees of freedom, such as vibrational or rotational states. These transitions can be used for laser cooling and quantum state preparation, important first steps for applications in quantum computing, quantum simulation, ultracold chemistry, dark matter detection and fundamental physics searches such as symmetry violations or variations in fundamental constants [9, 11, 87, 88, 208, 229]. While the additional degrees of freedom in molecules compared to atoms makes it more challenging to laser cool molecules than atoms, they also create new opportunities (*e.g.* quantum information can be stored in these extra degrees of freedom) [6, 10, 79–86, 230].

Diatomic molecules were the first molecules to be laser cooled experimentally [21, 22, 96, 122, 231–233] and the field has since expanded to polyatomic molecules [16, 17, 25, 140]. This expansion primarily relied on CaO moieties (or similar alkaline earth metal oxygen moieties) bonded to R group ligands such as CaOH and $CaOCH_3$ [92–95, 136]. CaO moieties are effective OCCs because they host electronic transitions that are strongly localized in real space such that they are within the Franck-Condon region. Large molecules containing CaO OCCs such as calcium phenoxide (CaOPh) were recently shown to optically cycle photons [125, 142]. In this work, we investigate molecules with multiple CaO OCCs and demonstrate that these single molecules can exhibit superradiance. We believe these molecules are both an exciting new platform for studying superradiant phenomena and may show improved optical cycling capabilities due to their superradiant excited states.

Superradiance (subradiance) is a collective phenomena in which a collection of emitters

form coherent excited states in which their transition dipoles constructively (destructively) interfere such that the radiative lifetimes of these excited states are enhanced (suppressed) relative to the individual emitters [234]. Two manifestations of superradiance are the emission of high intensity pulses of photons (superradiant bursts) and the enhanced emission rate from a singly excited state known as single-photon superradiance [235–239]. Superradiant bursts are characterized by the maxima of the emission intensity (I) increasing with the square of the number of emitters (N), $I \propto N^2$. Single-photon superradiance is characterized by the radiative lifetime (τ_{rad}) of a singly excited state being inversely proportional to N, $\tau_{rad} \propto N^{-1}$ [235].

Herein, we purposefully create molecules with multiple, spatially separated OCC sites and demonstrate, for the first time, single molecule superradiance. We elucidate how the OCCs interact with one another through their transition dipole moments and establish geometric rules that govern the energetic ordering of the superradiant and subradiant states through the use of a rather simple model Hamiltonian. Specifically, we show the generality and predictability of the Frenkel exciton model for molecules with multiple OCCs by testing it against accurate electronic structure methods for a set of molecules. We then show the utility of this model by rationally designing superradiant molecules with excited states properties optimal for laser-cooling applications. Lastly, we broaden the scope of this model by investigating two-photon superradiant emission pathways for three surface-patterned OCCs.

5.2.2 Results and Discussion

To these ends, we utilize the following model Hamiltonian (H) to understand the superradiant and subradiant excited states associated with the OCCs in complex molecules [240]:

$$H = \sum_{i\alpha} E_{i\alpha} a_{i\alpha}^{\dagger} a_{i\alpha} + \sum_{\langle i\alpha, j\beta \rangle} J_{i\alpha,j\beta} \left(a_{i\alpha}^{\dagger} a_{j\beta} + a_{j\beta}^{\dagger} a_{i\alpha} \right). \tag{5.1}$$

In Eq. (5.1), $i, j, ...$ are indices going over all OCCs, $\alpha, \beta, ...$ are indices indicating the direction of the transition electric dipole of the excited state, $E_{i\alpha}$ is the on-site energy of the excited

state, $a^{\dagger}_{i\alpha}$ ($a_{i\alpha}$) is a creation (annihilation) operator for the excitonic state $i\alpha$, $\langle\rangle$ indicates unique pairs and $J_{i\alpha,j\beta}$ is the dipolar coupling between spatially separated excited states:

$$J_{i\alpha,j\beta} = \frac{|\vec{\mu}_{i\alpha}|\,|\vec{\mu}_{j\beta}|}{4\pi\epsilon_0\epsilon_r\,|\vec{r}_i - \vec{r}_j|^3}\left[\hat{\mu}_{i\alpha}\cdot\hat{\mu}_{j\beta} - 3\,(\hat{\mu}_{i\alpha}\cdot\hat{r}_{ij})\,(\hat{\mu}_{j\beta}\cdot\hat{r}_{ij})\right] \tag{5.2}$$

In Eq. (5.2), ϵ_r is the relative permittivity of the host material ($\epsilon_r \approx 1$ for the gas-phase molecules studied herein), $\vec{\mu}_{i\alpha}$ is the transition dipole moment, $\vec{r}_i$ is the center of the transition density, $\vec{r}_{ij}$ is the vector connecting sites i and j and $\hat{\mu}_{i\alpha}$ and $\hat{r}_{ij}$ are unit vectors [240].

Fig. 5.7 shows how the model Hamiltonian predicts superradiant and subradiant excited states for a molecule with two OCCs using parameters extracted from an electronic structure calculation of a molecule with a single OCC. Calcium phenoxide (CaOPh) is our reference single OCC-containing molecule here because our molecules have CaO OCCs bonded to aromatic groups and there have been many recent theoretical and experimental studies of CaOPh [110, 124, 125]. The properties associated with the CaO OCC in CaOPh that are relevant to this work are the electronic state energies ($E_{i\alpha}$), location of the electronic transitions densities ($\vec{r}_i$) and electronic transition dipole moments ($\vec{\mu}_{i\alpha}$). These parameters are the CaO OCC in CaOPh are used to parameterize Eq. (5.1) and Eq. (5.2) for larger molecules with multiple OCCs. Specifically, we utilize the three lowest energy electronic states of CaOPh, where an unpaired electron is localized on the calcium, shown in Fig. 5.7: the ground state ($\tilde{\chi}$), the first excited state ($\tilde{A}$) with its transition electric dipole oriented in the plane of the benzene ring perpendicular to the CaO bond and the second excited state ($\tilde{B}$) with its transition electric dipole oriented perpendicular to the plane of the benzene ring. From time-dependent density functional theory (TD-DFT) calculations [241], the electronic excited state energies ($E_{\tilde{\chi}}$ is the zero of energy) are $E_{\tilde{A}} = 1.924$ eV and $E_{\tilde{B}} = 1.938$ eV and the transition electric dipole moments, centered on the Ca atom, are $\vec{\mu}_{\tilde{A}} = (0, 1.110, 0)$ eÅ and $\vec{\mu}_{\tilde{B}} = (0, 0, -1.127)$ eÅ where the CaO bond is along the x-axis and benzene ring in the xy-plane (Fig. 5.7). TD-DFT parameters give radiative lifetimes of 30.0 ns and 28.5 ns for these states, agreeing well with experimentally measured lifetimes [125].

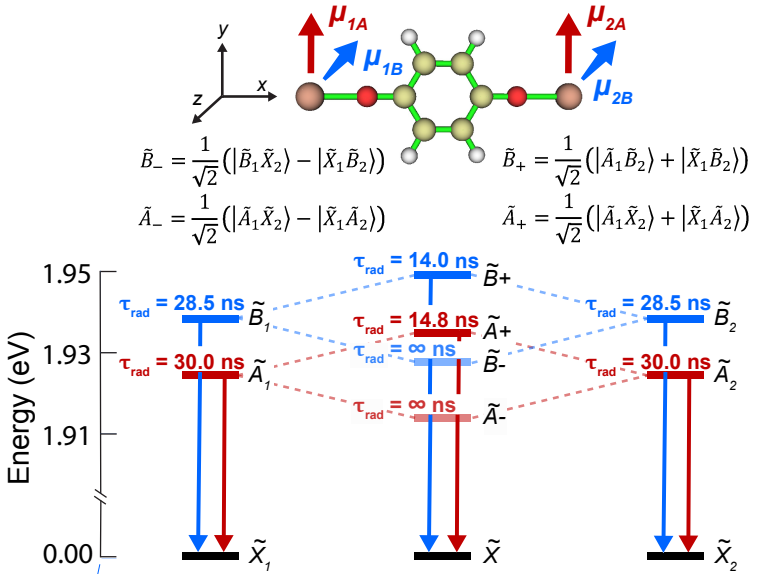

Figure 5.7: Excitation energies and radiative lifetimes (τ_{rad}) for the first few electronic excitations for 2-OCC CaO-quinone-OCa (center) using our model, based on the 1-OCC CaOPh [125]. The two OCC sites in CaO-quinone-OCa, 1 and 2, use excitation energies and transition dipole moments from a TD-DFT calculation of CaOPh as input into Eq. (5.1). The identical sites' energies and radiative lifetimes are seen on the left and right hand side of the figure, which combine to predict the energies and radiative lifetimes of the 2-OCC molecule.

Now, using these parameters of single CaO OCCs in CaOPh, we predict the superradiant and subradiant excited states of single molecules with multiple OCCs using Eq. (5.1). For CaO-quinone-OCa (Fig. 5.7), a diradical molecule where one unpaired electron is localized on each of the spatially separated calcium atoms, this equates to building a simple 4×4 Hamiltonian with the diagonals given by $E_{\tilde{A}}$ and $E_{\tilde{B}}$ since $\alpha \in \left\{\tilde{A}, \tilde{B}\right\}$ for each CaO group ($i, j \in \{1, 2\}$) and the off-diagonal coupling between the excited states of each CaO is given by Eq. (5.2). After diagonalizing this Hamiltonian and analyzing the eigenstates and their radiative lifetimes, we assign the excited state manifolds of CaO-quinone-CaO as $\tilde{A}-, \tilde{B}-, \tilde{A}+, \tilde{B}+$ as shown in Fig. 5.7. We use $+$ $(-)$ to denote superradiant (subradiant) states throughout this work. The two lowest energy excited states $\tilde{A}-$ and $\tilde{B}-$ of CaO-quinone-OCa are perfectly subradiant with infinite radiative lifetimes. The next two excited states, $\tilde{A}+$ and $\tilde{B}+$, are superradiant with radiative lifetimes of 14.8 ns and 14.0 ns, approximately half the radiative lifetimes of 30.0 ns for $\tilde{A}$ and 28.5 ns for $\tilde{B}$ in the single OCC molecule CaOPh (Fig. 5.7). The subradiant states are lower in energy than the superradiant states due to the side-by-side transition dipole alignment, $(\hat{\mu}_{i\alpha} \cdot \hat{r}_{ij})\,(\hat{\mu}_{j\beta} \cdot \hat{r}_{ij}) = 0$ and $\hat{\mu}_{1\alpha} \cdot \hat{\mu}_{2\beta} \geq 0$ in Eq. 5.2. Additionally, the energy level splittings are similar ($E_{\tilde{A}+} - E_{\tilde{A}-} \approx E_{\tilde{B}+} - E_{\tilde{B}-}$) because $|\vec{\mu}_{\tilde{A}}| \approx |\vec{\mu}_{\tilde{B}}|$.

In Fig. 5.8, we address the qualitative and quantitative accuracy of this model by comparing its predictions for the excited states of CaO-resorcinol-OCa to TD-DFT [241], equation-of-motion coupled-cluster singles and doubles (EOM-CCSD) [242] and complete active space self consistent field theory with dynamic correlation treated perturbatively (CASPT2) [243]. See Supplementary Materials in Ref. [244] for computational details. The model agrees with all electronic structure methods on the energetic ordering of the superradiant and subradiant states ($E_{\tilde{A}-} < E_{\tilde{B}-} < E_{\tilde{A}+} < E_{\tilde{B}+}$) and the relative strengths of their transition electric dipoles. These energies are in the same order as Fig. 5.7 due to the similar transition dipoles alignment (*i.e.* angles still within the side-by-side regime) [240]. Because the model uses input parameters from a TD-DFT calculation of CaOPh, its predicted en-

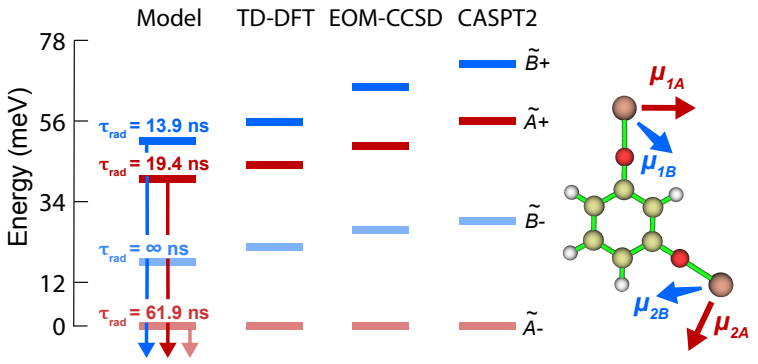

Figure 5.8: The first four excited states for CaO-resorcinol-OCa benchmarked against various levels of theory: the model Hamiltonian given by Eq. (5.1), TD-DFT, EOM-CCSD and CASPT2. The def2-TZVPPD basis set and associated ECP was used for all atoms. All energies are relative to the energy of the $\tilde{A}-$ state. The exact energy values for these states are 1.89 eV (Model), 1.89 eV (TD-DFT), 1.97 eV (EOM-CCSD) and 1.96 eV (CASPT2).

ergies for CaO-resorcinol-OCa most resemble the TD-DFT energies (Fig. 5.8). The model slightly underestimates the dipolar coupling ($J_{1\alpha,2\beta}$), which leads to an underestimation of the energy splittings between $\tilde{A}+$ and $\tilde{A}-$ and $\tilde{B}+$ and $\tilde{B}-$ by 9% and 3%, respectively, for CaO-resorcinol-OCa compared to TD-DFT. EOM-CCSD and CASPT2 have slightly larger energetic splittings as a result of their larger (and more accurate) transition dipoles. Because the model is dependent on input parameters from single OCC calculations, its accuracy can be improved by using inputs from higher levels of theory. Herein, we use TD-DFT inputs so that we can benchmark the model against large molecule calculations.

Now that we have the ability to rapidly understand the superradiant and subradiant states inherent to molecules with multiple CaO OCCs via this model Hamiltonian, the question arises as to how to rationally design molecules with ideal properties for laser cooling. To achieve laser cooling in molecules, the molecule should have an excited state with as large a transition dipole moment as possible with no lower energy excited states that could serve as nonradiative decay channels. Nonradiative processes increase the molecular temperature and decrease quantum coherence, ultimately disrupting laser cooling. With these requirements

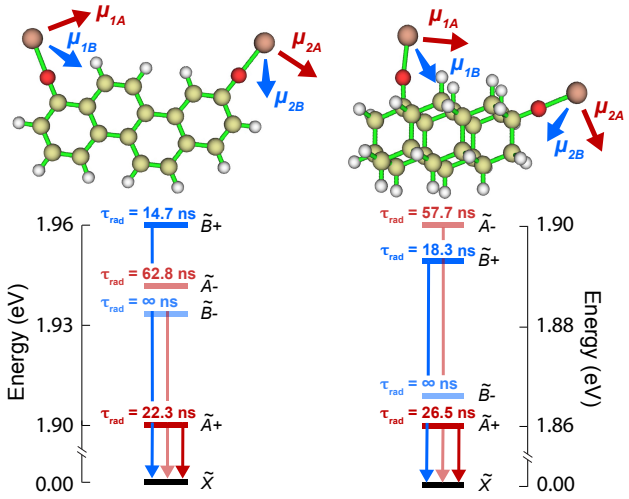

Figure 5.9: Radiative lifetimes (τ_{rad}) and excitation energies for the four single excitations associated with the OCCs of CaO-chrysene-OCa (left) and CaO-tetramentane-OCa (right) are shown. Input parameters for Eq. (5.1) were taken from TD-DFT calculations of 1-OCC CaO-chrysene and 1-OCC CaO-tetramenane, respectively.

in mind, CaO-quinone-OCa and CaO-resorcinol-OCa are not ideal prospects for laser cooling due to their lowest energy excited states being dark, subradiant states (Fig. 5.7 and Fig. 5.8). On the other hand, we propose CaO-chrysene-OCa and CaO-tetramentane-OCa, both shown in Fig. 5.9, as promising candidates for laser cooling, because the superradiant $\tilde{A}+$ state is their lowest energy excited state.

The superradiant $\tilde{A}+$ state is the lowest energy excited state in CaO-chrysene-OCa and CaO-tetramentane-OCa due to the geometrical nature of the dipolar coupling (Eq. 5.2). Specifically, $\tilde{A}+$ is lower in energy than $\tilde{A}-$ due to the head-to-tail alignment of the $\tilde{A}$ transition dipoles. In contrast, $\tilde{B}-$ is lower in energy than $\tilde{B}+$ because of the side-by-side alignment of the $\tilde{B}$ transition dipoles (Fig. 5.9). Quantitatively, the energy splitting between $\tilde{A}+$ and $\tilde{A}-$ is larger than $\tilde{B}-$ and $\tilde{B}+$ as a result of $\hat{\mu}_{i\tilde{A}} \cdot \hat{r}_{ij} \approx 1$ and $\hat{\mu}_{j\tilde{B}} \cdot \hat{r}_{ij} = 0$. Aliphatic ligands have larger HOMO-LUMO gaps than aromatic ligands, which lead to less interaction with the OCC transitions. Thus, $\tilde{A}$ and $\tilde{B}$ are more atom-like and nearly degenerate ($E_{\tilde{B}} - E_{\tilde{A}} < 1$ meV) in aliphatic groups relative to aromatic groups ($E_{\tilde{B}} - E_{\tilde{A}} >$

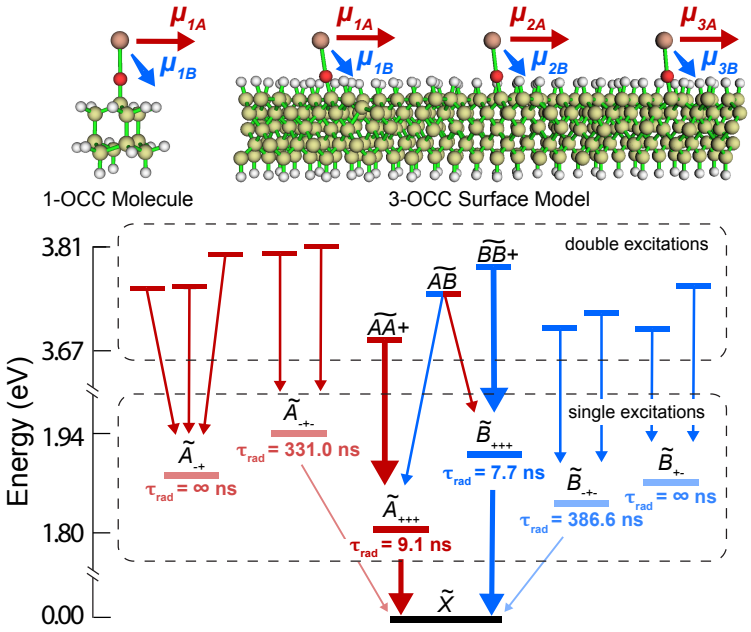

Figure 5.10: Single and double excitations are shown for a 3-OCC model, in which CaO-adamantane is used as the 1-OCC molecule as input, with three CaO OCCs spaced 1 nm apart to mimic CaO OCCs on a five-layer, cubic diamond (110) surface. The unit cell is $10 \times 10 \times 20$ Å^3 for each OCC to generate a $3 \times 3 \times 3$ supercell for this 3-OCCs system, as studied in previous papers [135, 139]. The superradiant states ($\tau_{rad} < 10$ ns) are in the center and the radiatively coupling between states are shown via arrows. Red (blue) arrows indicate radiative transitions that would have emission polarized parallel (perpendicular) to the CaO chain direction and the line thicknesses indicate the strength of the transition dipole moments.

10 meV). For CaO OCCs attached to diamond-like clusters (*e.g.* CaO-tetramentane-OCa), we used input parameters from a TD-DFT calculation of adamantane (Fig. 5.10).

The simplicity of this model Hamiltonian (Eq. 5.1) allows us to expand our scope beyond molecules to study multiple OCCs on surfaces, in this case diamond, out of reach of current electronic structure methods. Both single and double OCC excitations lie within the > 5 eV optical gap of diamond, which opens the door to many applications that require entangled multi-photon states [245–248]. In Fig. 5.10, we use our model to predict the single ($1.80 - 1.94$ eV) and double ($3.67 - 3.81$ eV) excitations for three CaO OCCs (modeled by CaO-

adamantane) spaced 1 nm apart on the surface diamond. This geometry leads to both head-to-tail ($\hat{\mu}_{i\tilde{A}} \cdot \hat{r}_{ij} \approx 1$) and side-by-side ($\hat{\mu}_{j\tilde{B}} \cdot \hat{r}_{ij} = 0$) oriented transition dipoles, similar to Fig. 5.9.

The lowest energy single excitation, $\tilde{A}_{+++}$, is superradiant with a radiative lifetime of 9.1 ns, approximately three times shorter than that of a single CaO OCC. The superradiant $\tilde{B}_{+++}$ has a radiative lifetime of 7.7 ns and is the highest energy single excitation in the $\tilde{B}$ manifold because of the side-by-side alignment. All other single excitations are subradiant. There are twelve total double excitations, but only three ($\widetilde{AA}+$, $\widetilde{BB}+$ and $\widetilde{AB}$) are strongly radiatively coupled to $\tilde{A}_{+++}$ and $\tilde{B}_{+++}$ (Fig. 5.10).

Our model predicts radiative decays of $\widetilde{AA}+ \rightarrow \tilde{A}_{+++}$ and $\widetilde{BB}+ \rightarrow \tilde{B}_{+++}$ that are consistent with expectations based on the Dicke ladder [234, 235, 237]. Specifically, $\widetilde{AA}+$ and $\widetilde{BB}+$ have radiative lifetimes approximately four times shorter than that of $\tilde{A}$ (23.9 ns) and $\tilde{B}$ (23.9 ns) in CaO-adamantane. Interestingly, $\widetilde{AB}$ is radiatively coupled to both $\tilde{A}_{+++}$ and $\tilde{B}_{+++}$. The radiative decay of $\widetilde{AB}$ to $\tilde{A}_{+++}$ ($\tilde{B}_{+++}$) would result in the emission of photon polarized perpendicular (parallel) to the CaO chain axis and the ensuing radiative decay from $\tilde{A}_{+++}$ ($\tilde{B}_{+++}$) to $\tilde{\chi}$ would result in the emission of a photon polarized parallel (perpendicular) to the CaO chain axis. This is an exciting feature as it can serve as an avenue for using superradiance to generate polarization entangled multi-photon states. Overall, our model shows that multiple CaO OCCs on diamond could be an exciting new platform for observing superradiant and emergent phenomena. For example, the excited states of CaO OCCs arranged in a square lattice may contain novel physics similar to the electronic bands of square net systems [249–252].

5.2.3 Conclusions

In summary, *single molecule superradiance* can occur in molecules containing multiple CaO optical cycling centers. We showed that these superradiant states are accurately captured by the Frenkel exciton model, which allowed us to design superradiant molecules suited

for laser cooling. Lastly, we went beyond single excitations and analyzed the multi-photon superradiant emission pathways for three CaO moieties on diamond. We are excited to see future extensions of this work (*e.g.* performing quantum dynamical simulations, the inclusion of electron-nuclear coupling, etc.) and uses of this model to uncover exotic physics in the excited states of systems with many optical cycling centers.

CHAPTER 6

Yb(III) Complexes as Quantum Sensors

6.1 Introduction to Atomic-Like Molecular Sensors

Atomic vapor cells (AVCs) are one of the most sensitive and widely deployed methods of detecting electromagnetic fields with applications ranging from astronomy, medicine, geophysical surveys, explosives detection to remote sensing [253, 254]. AVCs are typically derived from K, Cs, or Rb in a sealed container, where laser excitation is used to drive an 'ns' to '$(n+1)p$' transition. By monitoring the absorption/fluorescence of these gas-phase alkali atoms, AVC magnetometers have reached extraordinary sub-femtotesla sensitivity in a relatively compact form factor [255, 256]. Furthermore, combining microwave excitation and optical pump lasers allows for the preparation of collective quantum states of these systems that can be used for quantum measurement [255, 257, 258].

The established limit of AVC sensitivity for magnetic fields is set by the spin-projection noise:

$$\Delta B \approx \frac{1}{g\mu_B}\frac{\hbar}{\sqrt{N\tau T}} \tag{6.1}$$

Where ΔB is the uncertainty in the measured magnetic field, g is the ground state Landé factor, μ_B is the Bohr magneton, $\hbar$ is Planck's constant, N is the number of atoms, τ is the coherence time and T is the measurement duration. In AVCs, a higher N would improve sensitivity, but in practice it is offset by lower τ due to increased collision-based dephasing [253, 256, 259–262]. A liquid analogue to an AVC, *e.g.* an atomic-like molecular sensor (ALMS), would utilize atom-like transitions while minimizing drawbacks by accessing

much higher number densities. If narrow linewidths can be retained in solution, the number density/pathlength limits of AVCs could be overcome.

To explore this capability, we chose the *f-f* transitions in trivalent lanthanide complexes, often referred to as 'atom-like', as a potential testbed for the applicability of atomic physics technologies in condensed-phase chemistry. We focus on Yb^{3+}, noting that the $4f_{13}$ electron configuration allows for well-protected, electronic transitions between a small manifold of spin-orbit electron configurations. For a Yb^{3+} ion in the gas phase, transitions among spin-orbit states are parity forbidden, interacting only through magnetic dipole. However, the crystal field asymmetry in a Yb^{3+} complex results in coupling between $4f$ and $5d$ orbitals. The $4f/5d$ coupling intensifies with further deviation from centrosymmetric point groups, leading to higher oscillator strength. Simultaneously, interactions of the ligands with Yb^{3+} lower the energy of its open $5d$ orbitals, facilitating increased $4f/5d$ coupling. The net result is weakly allowed electric dipole transitions among f-electron configurations, creating atom-centered transitions with non-negligible oscillator strengths as described by the Judd-Ofelt theory [263–265]. They display near infrared absorption bands, which retain extremely narrow yet measurable linewidths even in condensed phase environments [266, 267]. Solubilization allows for a high number density of these species in a set volume, reaching upwards of 10^{19} molecules per cm^3 (*i.e.*, 10 mM), a value eight orders of magnitude greater than the average density of their AVC counterparts [268–271].

In this paper, we demonstrate an unprecedented ultra-narrow (< 1 meV) linewidth achieved in a solution at room-temperature of a molecular lanthanide system- a suggestive first step to liquid-based quantum sensing. Optical and magnetic spectroscopy with detailed electronic structure calculations allow us to assign these spectral features and point to design principles for "near-atomic" localized transitions in the metal center of the molecule and even narrower homogenous linewidths at 77 K. We show that a suitably narrow linewidth allows for liquid-based optical measurements of magnetic fields through direct transmission of circularly polarized light, down to the Earth's magnetic field (~ 0.25 G), paving the way

toward a novel liquid-based magnetometry method. Our results represent first steps toward liquid systems that can be analogized to an atomic vapor cell technology.

6.2 Methods

6.2.1 Computational Methods

The ground state of (thiolfan)YbCl(THF) was optimized in Turbomole [272], using the TPSSh functional [273, 274], the ANO-RCC basis set [275, 276] (ANO-RCC-VTZP for Yb, ANO-RCC-VDZP for Fe, ANO-RCC-VTZ for Cl, O, S and ANO-RCC-VDZ for C and H) and the D3 dispersion correction [107]. The effect of solvation on geometry optimization was included by employing the conductor-like screening model (COSMO) with a dielectric constant of $\epsilon = 7.58$ to model THF [277]. From this optimized geometry, a reduced model was used for multireference calculations below. In the truncated model, the ferrocene unit was removed and the sulfur atoms were capped with hydrogens, after which the hydrogens were relaxed while the other atoms were held fixed.

As implemented in Openmolcas [278], the multireference CASSCF/MS-CASPT2 methods [279–283] were used in combination with the same ANO-RCC basis set. The second-order DouglasKrollHess (DKH2) one-electron spinless Hamiltonian was applied for all wave function theory calculations to allow for spin-free relativistic effects [284–286]. A complete active space used in the CASSCF calculations comprised of 13 electrons in 12 orbitals (seven Yb $4f$-like orbitals and five Yb $5d$-like orbitals, Tabs. S3 and S4 in [287]). The state-averaged (SA-)CASSCF formalism was used, involving the 20 lowest-lying states. The dynamic MS-CASPT2 correlation was then included via the CASPT2 module. Spin-orbit coupling was added through the RASSI-SOC module [288, 289], where oscillator strengths and transition energies were calculated for electric and magnetic dipole transitions.

Finally, g tensors and spin-orbit coupling matrix elements were computed with the RASSI module [290]. Length-dipole oscillator strengths were reported in the main text, the length

and velocity dipole results are listed in [287]. The tables underscore the importance of $4f/5d$ orbital mixing and its effect on spin orbit coupling, which in turn mediates oscillator strength. Recent findings suggest that f-orbitals are quite sensitive to SOC and these orbitals should be optimized with SOC included [291]. One way to include this effect is through an exact two-component transformation (X2C) but the quantitative importance of including SOC via X2C vs. other methods requires further study [292].

Several limitations of our theoretical calculations should be mentioned. Due to the large system size and number of electrons, the active space used in the CASSCF calculations is still fairly limited, prohibiting us from including all the ligand-metal bonding orbitals. We thus cannot accurately capture the covalency of metal-ligand bonds and how much the pure $4f$ states are influenced by the ligand. Additionally, spin-orbit coupling is added for calculating transitions and oscillator strengths, but (thiolfan)YbCl(THF) orbitals are not optimized to include spin-orbit coupling. This could allow for an increased $4f/5d$ mixing in our complete active space orbitals that we currently do not observe and could also alter the symmetry of the $4f$ orbitals involved in transitions II-V. Furthermore, the multireference calculations are performed in the gas phase and as a static approximation. Dynamic calculations of the molecular vibrational structure and solvent contributions and fluctuations will help aid additional understanding of the nature of the target transition IV, such as its linewidth.

6.2.2 Experimental Methods

The Yb^{3+} complex $[(\text{thiolfan})\text{YbCl}]_2$ (thiolfan = 1,1-bis(2,4-di-tert-butyl-6-thiomethylenephenoxy) ferrocene) was synthesized by deprotonating H_2(thiolfan), followed by a reaction with $YbCl_3(THF)_3$ (THF=tetrahydrofuran) at -78°C (SI Section I-A, B in [287]). The structures of the monomer with THF coordination, (thiolfan)YbCl(THF) and dimer bridged by two chlorides, $[(\text{thiolfan})\text{YbCl}]_2$, were confirmed by single crystal x-ray diffraction (Figs. S1-S2 in [287]). Characterization of the compounds was also accomplished by nuclear magnetic resonance (NMR) spectroscopy and elemental analysis (SI Section I-A, B, D, E in [287]). We note that the spectral mea-

surements in the following sections were performed after dissolving a sample in THF or 2-MeTHF (2-methyltetrahydrofuran), in which both compounds exist as the monomer, (thiolfan)YbCl(THF). The monomer vs. dimer equilibrium is evident in concentration-dependent absorption, diffusion ordered spectroscopy (DOSY) and NMR measurements (SI Section I-E in [287]).

The magnetic properties were investigated using a superconducting quantum interference device (SQUID) in the solid state and the Evans method in solution [293]. A magnetic susceptibility value of $\chi_m T = 4.77$ emu·K/mol was obtained for the solid sample crushed out of toluene from direct current susceptibility measurements at 290 K after a diamagnetic correction. This is in line with the reported $\chi_m T = 5.14$ emu·K/mol for two Yb^{3+} centers ($^2F_{7/2}$, $g_J = 8/7$) (further details in SI Section I-F in [287]). The paramagnetic properties of the monomer, (thiolfan)YbCl(THF), were evaluated in THF-d_8 revealing $\chi_m T = 2.47$ emu·K/mol at room temperature, in line with the reported value for a single Yb^{3+} center ($\chi_m T = 2.57$ emu·K/mol). This suggests minimal interaction of the Yb^{3+} center(s) in both the monomer and dimer.

6.3 Results and Discussion

To investigate the relationship between the structural and spectral properties of this class of Yb^{3+} compounds, two derivatives of (thiolfan)YbCl(THF), **1**, were synthesized: (thiolfan*)YbCl(THF), **2**, thiolfan* = 1,1-bis(2,4-di-tert-butyl-6-thiophenoxy)ferrocene and (thiolfan) Yb[$N(SiMe_3)_2$], **3**. They were made separately for comparison by modifying the supporting ligand and exchanging the chloride with an amide, respectively. Spectroscopic data presented in this study pertains to Yb samples in THF, unless otherwise noted.

6.3.1 Electronic Spectroscopy

We measured the broadband electronic absorption spectrum of (thiolfan)YbCl(THF) (Fig. 6.1a, b) using a conventional UV-Vis spectrometer (Fig. 6.1c, top panels). We observe several features: a broad ligand absorption band (I) in the visible range around 400-600 nm (Fig. S30 in [287]), several weakly absorbing transitions (II and III) from 880-950 nm and the transition of primary interest: the strongly absorbing, ultranarrow transition (IV) at 980 nm. As evident in the small spread of transitions II-IV, lanthanide complexes possess strong spin-orbit coupling (1 eV) and much smaller ligand field splitting ($\sim 10 - 100$ meV) than typical transition metal complexes [294, 295]. Our primary focus is on the narrow transition denoted IV, which shares a similar energy gap as the transition between the $^2F_{7/2}$ and $^2F_{5/2}$ states of the gas phase Yb^{3+} ion (10214 cm^{-1} or 1.2664 eV, arising almost entirely from spin-orbit splitting) [296]. Conventional UV-Vis spectrometers lack the resolution necessary to quantify sub 1 meV linewidths in the near infrared. Therefore, we utilize a narrowband, continuous-wave Ti:sapphire laser to scan the transmission (Fig. 6.1c, bottom panel; SI section II-B in [287] for methods).

The resulting high-resolution spectrum of IV fits best to a Lorentzian function with a center energy of 1.2637 eV with a full width at half maximum (FWHM) of 0.625 ± 0.006 meV. Exciting at the ligand absorption band (425 nm), we also recorded the fluorescence spectra using a home-built high-resolution Fourier spectrometer (Fig. 6.1d). The emission is collected in an all-reflective off-axis parabolic epifluorescence setup, after which it goes through a Mach-Zender interferometer and towards superconducting nanowire single photon detectors [297]. We note two emission bands, one which overlaps nearly perfectly with IV observed in absorption and another band, V, separated by 80 meV. IV shows negligible Stokes shift between absorption and emission, consistent with minimal intersystem crossing and vibronic coupling.

To investigate the intrinsic linewidth of transition IV, we collected absorption as a func-

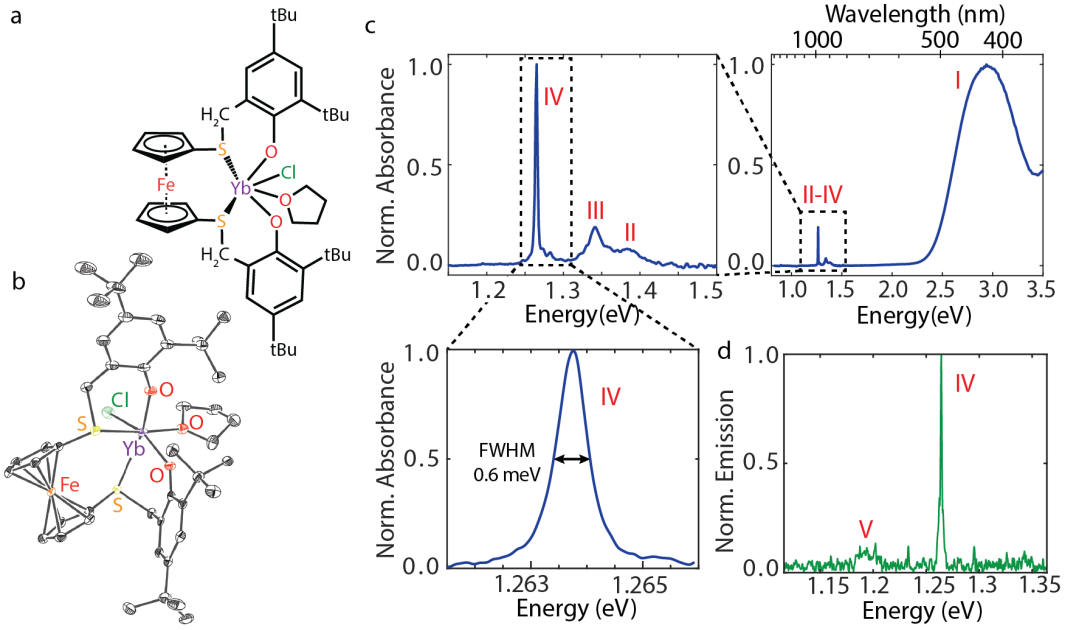

Figure 6.1: Optical characterization of (thiolfan)YbCl(THF) (a) Drawing and (b) crystal structure of (thiolfan)YbCl(THF). (c) Wide-field absorption spectrum with zoomed-in absorption spectra around the Yb features, showing a high-resolution absorption scan of the Yb transition with the highest oscillator strength around 980 nm or 1.264 in the bottom left. The absorption spectra were taken with a 3 mM solution in THF at room temperature. (d) Normalized emission spectrum, obtained through Fourier-transform spectroscopy.

tion of temperature down to 7 K (Fig. 6.2a-b). The feature remains unimodal at cryogenic temperatures, with a slight broadening and blue shift in peak energy as the temperature increases to 300 K (full temperature range shown in (Fig. S32 in [287]). It should be noted that the sample was frozen in a glass-forming solvent (2-MeTHF) and not crystallized out of solution. Thus, the spectra in Fig. 6.2a reflect the optical behavior of the sample in disordered glass at varying temperatures, therefore more closely reflecting its behavior dissolved in solution, as opposed to a solid or crystal. The peak frequency and the FWHM starts to increase near 100 K, corresponding to the glass transition of the solvent and its concurrent decrease in density [298]. The fact that cryogenic temperatures did not resolve any underlying features suggests that IV is dominated by an inhomogeneously broadened

set of transitions, brought on by different solvation environments (rather than vibrational coupling). That is, individual chromophores may have slightly different geometries and thus varying transition energies. We hypothesize that the intrinsic linewidth of individual chromophores is most likely narrower than the feature shown in Fig. 6.2a. Further discussion on the sources of linewidth broadening can be found in SI Section II-D in [287].

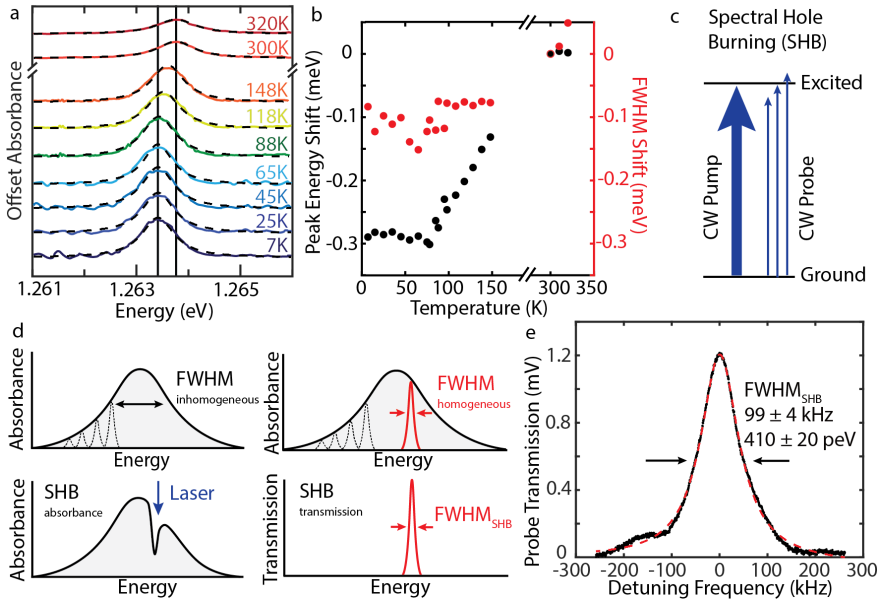

Figure 6.2: Investigating linewidth broadening mechanisms a) Temperature-dependent absorption scans of (thiolfan)YbCl(THF). Solid vertical lines are visual guides to emphasize the shift in peak center. b) FWHM and transition energy offsets from corresponding room temperature values. Error bars were too small and are shown in Fig. S32 in [287]. c) Energy diagram of the SHB experiment. d) Top panels: diagrams of inhomogeneously and homogeneously broadened linewidth. Bottom panels: diagrams of SHB in absorption and transmission. e) SHB transmission signal of (thiolfan)YbCl(THF) at 77 K.

To resolve the homogeneous linewidth, we performed spectral hole burning (SHB) experiments on (thiolfan)YbCl(THF). A 0.2 mm cuvette with $\sim$ 30 mM sample in 2-MeTHF is placed in the cryostat and cooled to 77 K. We place a narrow-band, pump laser at the resonant frequency of transition IV (305.5 THz) and scan the probe laser around that fre-

quency (SHB setup in Fig. S33 in [287]). The CW pump excitation (8 mW) creates a hole in the ground state population, which is detectable by a weaker CW probe beam (0.7 mW), as shown in Fig. 6.2c. The homogeneous linewidth can be delineated from the inhomogeneously broadened feature by analyzing the probe transmission as it scans around the pump laser frequency (Fig. 6.2d). The probe transmission as a function of the detuning frequency is plotted in Fig. 6.2e, demonstrating a narrower feature with a FWHM of 99 kHz or 410 peV, which is more than six orders of magnitude narrower than the room-temperature absorption linewidth. Presumably, this 410 peV linewidth is near the limit of the homogeneous linewidth of the transition. The SHB linewidth corresponds to a 1.6 μs lifetime that is very close to the 3.2 μs measured fluorescence lifetime at room temperature (Fig. S34 in [287]), which is comparable to lifetimes of other Yb complexes [299–301]. The narrower SHB linewidth indicates that absorption feature at room temperature consists of many transitions. However, we were not able to observe SHB at room temperature, suggesting the liquid environment results in spectral diffusion, frozen out in the glass.

(thiolfan)YbCl(THF) displays a narrower absorption linewidth in solution at room temperature than those of other Yb^{3+} molecules in a variety of media and temperatures. We compare the 0.6 meV linewidth to those of other Yb^{3+} coordination complexes in solution as well as in single crystal, some of which were measured at cryogenic temperatures (Fig. 6.3a; expanded linewidth comparison in SI Sec. II-E in [287]) [302–305]. Our central hypothesis for the correlation between molecular structure and ultra-narrow absorption linewidth is that the rigidity of the ferrocene backbone in the supporting ligand sphere minimizes spectral broadening. For example, Yb(trensal) (where H_3(trensal) is 2,2',2"-tris(salicylideneimino)triethylamine) is a compound with a high degree of magnetic anisotropy and well-defined optical features that shows a linewidth of 4.6 meV (Fig. 6.3a), roughly an order of magnitude broader than (thiolfan)YbCl(THF) [303]. Contrary to our system, Yb(trensal) shows many absorption features assigned to other spin-orbit transitions and vibrations and a large apparent Stokes shift, suggesting a more mixed and "molecular" elec-

tronic structure in comparison. Even Yb^{3+} doped crystals at 4 K show a larger absorption linewidth of 3.6 meV (Fig. 6.3a), almost six times broader than that of (thiolfan)YbCl(THF), attributed to inhomogeneous crystal environments and phonon coupling [304, 306].

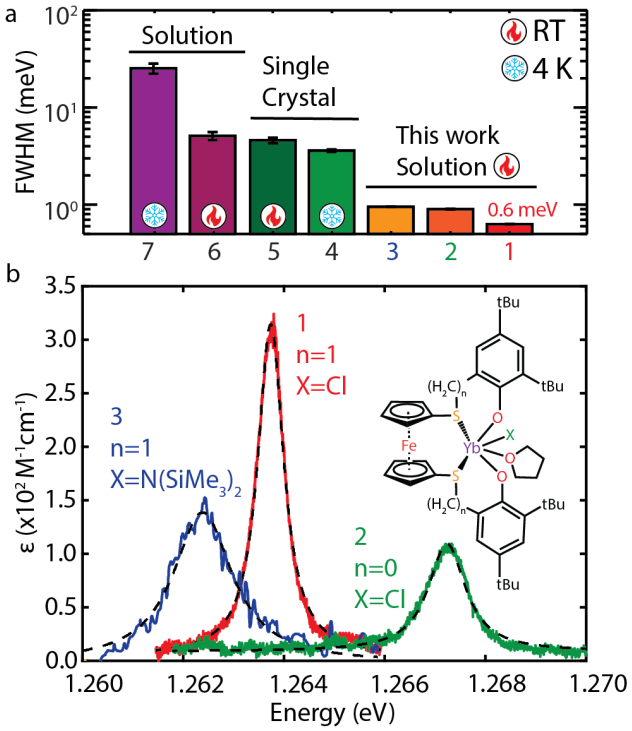

Figure 6.3: Effects of coordination environment on linewidths a) Absorption FWHM comparison to other Yb^{3+} complexes [302–305]. b) Drawing of compounds with different ligand designs and their corresponding absorption peaks at 3 mM concentrations. Clarification on the numbered compounds in SI section I-B in [287].

We investigated the relationship between this ultranarrow solution linewidth and molecular geometry by synthesizing two derivatives of (thiolfan)YbCl(THF) with slightly different ligand environments (Fig. 6.3b). Variations consists of one fewer carbon connecting the ferrocene and phenoxy moieties (Fig. 6.3b: **2**) and of replacing -Cl with -$N(SiMe_3)_2$ (Fig. 6.3b: **3**). A high-resolution scan of the transmission of the three derivatives indicates that the linewidth of transition IV is preserved, likely because the rigidity of the ferrocene backbone provides protection of the radiative transition IV from other sources of line broadening. Com-

pound **3** has a FWHM of 0.947 ± 0.005 meV, while **2** has a FWHM of 0.902 ± 0.007 meV, which are both comparable to the 0.625 meV linewidth of **1**. Although the exact broadening mechanism is unknown, the slight increase in linewidth is mostly likely due to the shorter carbon bridge of **2** changing metal-ligand coupling and the strong ligand field of the amide group in **3** contributing to the inhomogeneous broadening of the metal transition. The important observation, however, is that all three ytterbium complexes display near record linewidths in solution at room temperature, despite shifts in the primary transition energy that can be attributed to slight deviations in the coordination geometry. Therefore, the original thiolfan ligand preserves the narrowest Yb^{3+} transition linewidth, while minimizing the ligand effects relative to the ground spin-orbit transition (IV).

6.3.2 Electronic Structure Analysis

The isolated Yb^{3+} ion possesses seven degenerate states arising from orbitals of the $4f$ shell with 13 valence electrons. Large, electronic spin-orbit coupling separates the $4f$ states into spin-orbit states, creating the optical NIR transition from the eight-state $^2F_{7/2}$ to the six-state $^2F_{5/2}$ manifolds [267]. In a molecular framework, each spin-orbit manifold is further split due to the ligand-field contributions, giving rise to the individual electronic transitions II-V (Fig. 6.4a). Magnetic dipole analysis of transition energies and oscillator strengths (SI section III-A) prompted us to assess the degree of molecular/atomic character of electric dipole transitions using multireference electronic structure theory (SI section III-B) [307]. Our calculations show that IV is primarily composed of states with $\sim 99\%$ $4f$ character, with the ground and excited states containing mixtures of several $4f$ orbitals. To demonstrate, a visual guide (Fig. 6.4b) captures the primary basis orbitals that contribute to the ground and excited state wavefunctions, although we note that these pictures do not reflect the overall multireference nature of the molecular orbitals (full set of complete active space, CAS, orbitals shown in Tabs. S3 and S4 in [287]).

We find that inclusion of the virtual Yb $5d$ orbitals into the '13 electrons in 12 orbitals'

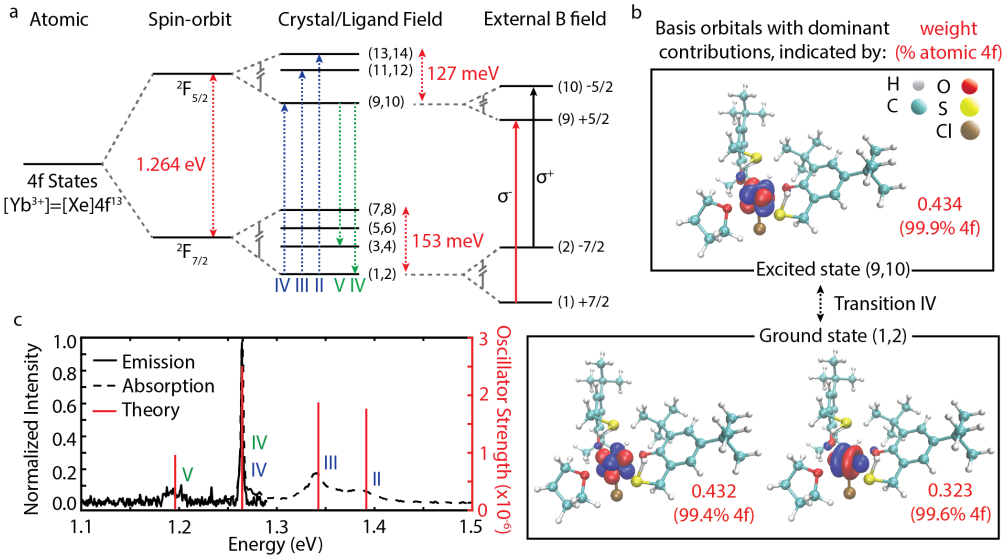

Figure 6.4: a) Electronic structure diagram of (thiolfan)YbCl(THF) showing the incorporation of spin-orbit and ligand field effects on the Yb^{3+} atomic orbitals, calculated with CASSCF/CASPT2/RASSI-SOC level of theory. In a magnetic field, the molecular orbitals are further split to states with primarily spin and characters. b) Visualization of the CASSCF basis orbitals that have dominant contribution(s) to the molecular orbitals involved with transition IV, demonstrating "atom-like" properties. c) Comparison between emission/absorption spectra and the calculated transition energies and oscillator strengths.

active space (*i.e.*, seven Yb($4f$) + five Yb($5d$)) is critical for obtaining the transition energies and oscillator strengths, in agreement with experiment and in accordance with the Judd-Ofelt theory (Fig. 6.4c) [265, 308]. Primarily, we attribute the enhanced oscillator strengths to an increased mixing between the $4f$ and $5d$ states, allowing E1 transitions (Tab. S6 in [287]). The $5d$ virtual orbitals mix with virtual ligand orbitals, lowering them in energy and further enhancing oscillator strength [309]. By incorporating the virtual $5d$ orbitals in the active space, we observe a slight change from the purely $4f$ atomic orbitals to molecular orbitals containing small contributions from the ligands (Tab. S7 in [287]). Due to lowering the symmetry of $4f$ states, the increased ligand character may also be responsible for an enhancement in the calculated oscillator strengths in transitions II-IV. Also,

the atom-like characteristic of the molecular orbitals is further confirmed by the agreement among calculated g factors for the ground and excited states ($g_g = 7.89$ and $g_e = 4.26$), the expected g factors of gas-phase Yb^{3+} ($g_g = 8$ and $g_e = 4.28$) and experimentally obtained values ($g_g = 7.486 \pm 0.008$ and $g_e = 3.2 \pm 0.2$; further details in SI Section III-D in [287]). Altogether, we describe the transitions II-V from fig. 6.4c as dominated by Yb $4f$ orbitals. Since the strength of spin-orbit coupling fundamentally contrasts with the covalency of the metal-ligand bond, we speculate both $4f/5d$ and $5d$/ligand effects must be balanced in the system and the transition energies and intensities can thus be influenced by the geometry and the nature of the ligand, as observed for different ligand designs (Fig. S37 in [287]).

6.3.3 Detecting Magnetic Fields

We decided to leverage the extraordinarily narrow linewidth of (thiolfan)YbCl(THF) and its open-shell character to detect magnetic fields. We first performed magnetic circular dichroism (MCD) measurements to study spin characteristics. MCD measures the differential absorption of + and − circularly polarized light induced in a sample under a strong magnetic field that is oriented parallel to the light propagation [310]. Typically, resolving these shifts requires a superconducting magnet, cryogenic temperatures and lock-in detection [311]. In contrast, we easily measure these shifts using a permanent rare-earth magnet set under the sample at room temperature. With a 0.38 T field, we induce a 23 GHz (0.096 meV) shift in IV between right- and left-hand circularly polarized excitations (Fig. 6.5a), corresponding to the Zeeman splitting of transition IV (Fig. 6.4a). We observe a linear correlation between the magnetic field strength and Zeeman splitting by changing the distance between the static magnet and the sample (Fig. S42 in [287]). From the linear correlation of the Zeeman splitting with the static magnetic field, we can extract the effective transition magnetic moment as 2.2 ± 0.1B. Finally, the subtraction between the + and - transitions produces the MCD signal, which varies in intensity with the change in magnetic field strength (Fig. 6.5b).

Using this MCD signal, we demonstrate three different schemes for magnetic sensing.

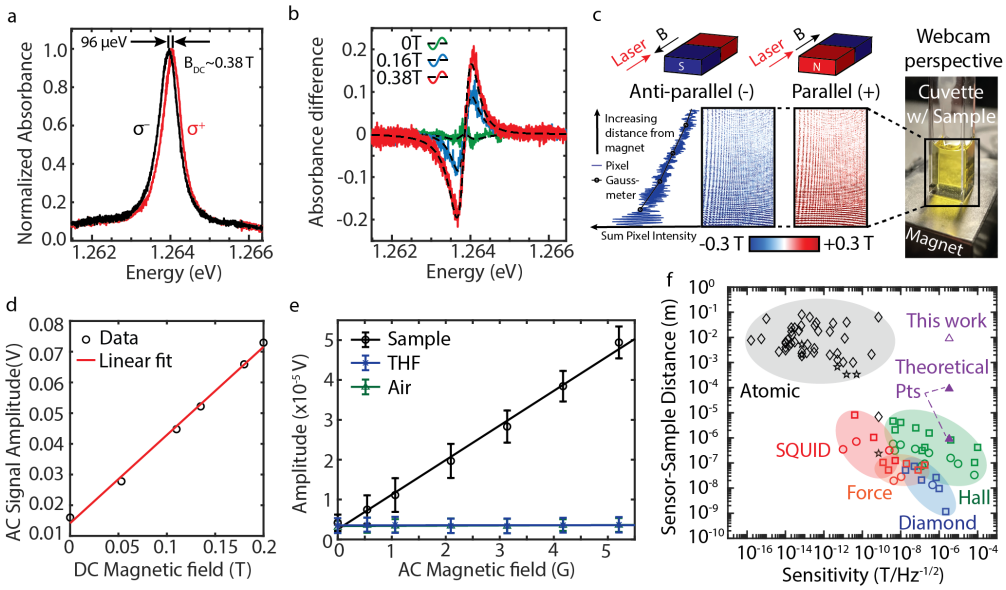

Figure 6.5: a) Room temperature Zeeman splitting under a static magnetic field of 0.38 T at around 3 mM concentration. b) Differential absorbance of left and right circularly polarized light under varying DC field strengths. c) Two snapshots of dynamic MCD imaging video demonstrating parallel and anti-parallel orientations of the magnetic field and laser propagation. d) Amplitude of the oscillating transmitted light through the sample under a static magnetic field of 0-0.2 T, measured by a gaussmeter. e) Increase of frequency modulation signal with the amplitude of the applied AC magnetic field in the presence of (thiolfan)YbCl(THF). f) Compilation of sensitivity values of other spin-based magnetometry imaging methods, as it compares to our work, plotted against the "closes't' approach of the sensor in proposed device design. This plot was adapted with permission from [312]).

First, we imaged a DC magnetic field at room temperature (Fig. 6.5c). The transmitted beam was expanded and imaged with a webcam through the sample in a glass cuvette placed above a static magnet. The pixel intensity was converted to magnetic field strength by calibrating to gaussmeter measurements. Since the circularly polarized transmission varies with the strength of the magnetic field, we can extrapolate to a magnetic field map, both in intensity and relative direction (*e.g.*, parallel or anti-parallel to laser propagation). The sensitivity of this measurement depends on the uncertainty of the g factor and the resolution

of the absorption measurement, leading to a sensitivity of 0.05 T (500 G) with this MCD setup (SI Section IV-B). We include a video of a spinning magnet altering the transmission as a supplementary video.

Second, we measured a DC magnetic field, using a laser beam with oscillating polarization (experimental setup in SI Section IV-C in [287]). To change the frequency rapidly, we use two acoustic optical modulators, which are driven with different radio frequencies offset by Δfp. By recombining the two beams, we create a beam that has oscillating polarizations at frequency Δfp. With the presence of a static magnetic field, the transmitted light intensity will also be modulated at Δfp, corresponding to the sample's MCD response. At Δfp= 100 kHz, we can examine how the amplitude of the transmitted light changes with the static magnetic field (Fig. 6.5d). We observe the expected linear trend, confirming the capability of this sample to measure static magnetic fields down to a 0.025 T (250 G) difference.

Third, we directly measured an AC magnetic field. We applied a small AC magnetic field (0-5 G at fAC=1 kHz) by adding a Helmholtz coil (SI Section IV-D) to give rise to two more sidebands at frequency ΔfpfAC. This signal is measured by a spectrum analyzer, where the sideband peak heights increase with the amplitude of the applied AC magnetic field. The (thiolfan)YbCl(THF) solution shows a monotonically increasing linear trend with the AC magnetic field, whereas the THF solvent and air show no dependence on the magnetic field (Fig. 6.5e; signal over time shown in Fig. S46 in [287]). With this method, we can measure AC magnetic fields down to 0.5 G, which is at the scale of the Earth's magnetic field. Even though these measurements are performed with a solution at room temperature, we can achieve a sensitivity of 3.33 μT Hz$^{-1/2}$.

6.3.4 Comparison to Other Technologies

There are several important figures of merit in comparing ALMS to other electromagnetic sensing technologies- sensitivity, frequency range and distance from sample. The most important figure of merit is magnetic field sensitivity, which describes the smallest magnetic

field that can be detected within a given measurement time. For (thiolfan)YbCl(THF), the sensitivity is governed by the absorption change upon applying a magnetic field, where the most drastic response comes with the steep slopes in the absorption feature. We estimate that our limit in sensitivity is set by the signal-to-noise difference in transmission, where our best resolution comes from the measurement of a small AC magnetic field with 3.33 μT $Hz^{-1/2}$ sensitivity. We note that quantum sensing technologies operate through modulation of ground-state quantum coherences, prepared through optical and microwave pumping and readout through changes in absorption, polarization, or fluorescence intensity. Besides AVCs, other spin-based magnetometers include nitrogen vacancies in diamond and color centers in crystal environments, both of which are also enabled by optical state preparation of pure quantum states that enable extraordinary sensitivity [309, 310]. Compact designs of AVCs that are widely used in miniature circuits demonstrate an optimal sensitivity of 50 $pTHz^{-1/2}$ with the most sensitive atomic optical magnetometer exceeding a 10^{-15} $THz^{-1/2}$ sensitivity [253, 256, 313]. The typical sensitivities of magnetic sensing based on single nitrogen vacancy in diamond range from tens of μT $Hz^{-1/2}$ for DC fields to tens of nT $Hz^{-1/2}$ for AC fields [314]. To be competitive with the sensitivities of these devices a state preparation and readout of spin superpositions in the electronic ground state are required that have yet to be shown in a liquid or glass environment. Nevertheless, a simple MCD-based magnetometry method with (thiolfan)YbCl(THF) puts us at a comparable sensitivity to other known spin-based magnetometers, such as Hall-effect sensors, as shown in Fig. 6.5f [312, 315].

The second figure of merit is the frequency at which these signals can be measured. We measured both DC and higher frequency field modulation up to 1 kHz but have not fully characterized the highest frequency possible to measure. We hypothesize it is likely limited by the excited state lifetime of the system (Fig. S34 in [287]), in which case the modulation period must be longer than the lifetime. AVCs tend to have relevant coherence times at the scale of 10^{-3} to 10^{1} seconds, depending on whether they are limited by the spin relaxation time T1 or coherence time T2 [316, 317]. In comparison, our Yb(III)-based ALMS shows

much shorter spin relaxation times of T1 = 518 μs and T2 = 0.82 μs at 3.6 K and 320 mT field (Fig. S41 in [287]). However, it should be noted that spin relaxation is not the major contributor that sets our absorption linewidth at room temperature. The SHB linewidth of 99 kHz corresponds to a lifetime of 1.6 μs, which is nearing the measured T2 time. We hypothesize that if we achieve narrower linewidths that can be used for MCD magnetometry, then spin dephasing may set the ultimate sensitivity.

The third figure of merit is the distance at which a magnetic field can be measured, namely the sensor-sample distance. Broadly speaking, the sensor-sample distance represents the effective geometry of a given magnetic sensor. In the context of nanoscale imaging, where magnetometers are used to detect single spin fields, it is crucial that the magnetic field sensor can capture the dipole field, which decreases with the cubed distance. Here, systems with high number densities of magnetically sensitive molecules may provide an advantage. For example, (thiolfan)YbCl(THF) can range two magnitudes in concentration while retaining its spectral linewidth (Fig. S48 in [287]) and is able to achieve an optical density of 1 in a thin 0.2 mm path length cuvette. With this advantage of high number density, we estimate a theoretical sensor-sample distance of 1-100 μm can be achieved with further device engineering (Fig. S49 in [287]), effectively providing a sensor to sample distance that is considerably shorter than that of current AVC technologies.

This study aims toward a rare-earth alternative to AVC quantum sensors used in biology. A recent publication demonstrates that AVCs are used for magnetoencephalography to detect magnetic fields produced from the flow of electric currents in neurons [318]. The operating principle for AVCs is similar to the one employed for (thiolfan)YbCl(THF) magnetometry, though AVCs utilize state preparation to greatly enhance the change observed due to external fields. While the sensitivity needs to be much improved, the advantage of solubilizing the sensor to overcome the particle density limit is real. Using MCD as a magnetic contrast approach, we determined that the mathematical limit to the sensitivity of an MCD-based

method can be approximated as:

$$\Delta OD \approx \frac{g_{eff}}{\Gamma^2} \tag{6.2}$$

where the sensitivity of the absorption measurement is proportional to the geff factor of the driven transition and is inversely proportional to the square of the linewidth (see derivation in SI Section IV-F in [287]). This indicates that for transitions with the same oscillator strength, narrowing the linewidth by half will increase the sensitivity by a factor of four, motivating the need for further chemical insight into synthesis and post-synthesis methods that narrow optical transitions. Considering that the linewidth remains the same across two orders of magnitude, (thiolfan)YbCl(THF) poses as a promising candidate for an ALMS prototype that may improve upon existing AVC technology in biomedical applications. If we can achieve a narrower linewidth at room temperature through molecular ligand design in future studies, ALMS can achieve standards of AVCs in their magnetometry applications with the advantage of more than six orders or more increase in particle density. Therefore, future investigations born out of this manuscript may pave the way towards rare earth complex quantum sensors in biology.

6.4 Conclusions

(thiolfan)YbCl(THF) shows an extraordinarily narrow $^2F_{7/2}$ to $^2F_{5/2}$ lanthanide centered optical transition in solution at room temperature. While the design principles for such a narrow transition will require further investigation, crucial orbital mixing between the d and f orbitals of Yb and further mixing with the ligand orbitals lead to a non-zero oscillator strength for the observed transition. In parallel, the rigidity and low symmetry afforded by the supporting ligand assist in concentrating the minimal oscillator strength to an ultra-narrow transition. This suggests that fine tuning the low symmetry structural components may become a primary design consideration in developing new ALMS systems. Further theoretical, synthetic and spectroscopic work will help elucidate the tradeoffs between ligand

rigidity, orbital mixing, covalency and solvation. In summary, we demonstrate an immediate application of Yb complexes for an MCD-based measurement and imaging of relatively weak magnetic fields. We achieve sufficient sensitivity by leveraging the large number density afforded by direct solvation of the complex. For further work, we hypothesize that investigation of quantum state preparation and readout of (thiolfan)YbCl(THF) will lead to higher sensitivities in analogy to AVCs, paving the way towards lanthanide complexes in precision quantum sensing.

Bibliography

[1] L. D. Carr, D. DeMille, R. V. Krems, and J. Ye, New J. Phys. **11**, 055049 (2009).

[2] J. I. Cirac and P. Zoller, Phys. Rev. Lett. **74**, 4091–4094 (1995).

[3] H. Häffner, W. Hänsel, C. Roos, J. Benhelm, D. Chek-al Kar, M. Chwalla, T. Körber, U. Rapol, M. Riebe, P. Schmidt, *et al.*, Nature **438**, 643–646 (2005).

[4] S. A. Diddams, J. C. Bergquist, S. R. Jefferts, and C. W. Oates, Science **306**, 1318–1324 (2004).

[5] D. DeMille, J. M. Doyle, and A. O. Sushkov, Science **357**, 990–994 (2017).

[6] V. V. Albert, J. P. Covey, and J. Preskill, Phys. Rev. X **10**, 031050 (2020).

[7] J. F. Barry, D. J. McCarron, E. B. Norrgard, M. H. Steinecker, and D. DeMille, Nature **512**, 286–289 (2014).

[8] L. Anderegg, L. W. Cheuk, Y. Bao, S. Burchesky, W. Ketterle, K.-K. Ni, and J. M. Doyle, Science **365**, 1156–1158 (2019).

[9] I. Kozyryev and N. R. Hutzler, Phys. Rev. Lett. **119**, 133002 (2017).

[10] P. Yu, L. W. Cheuk, I. Kozyryev, and J. M. Doyle, New J. Phys. **21**, 093049 (2019).

[11] M. L. Wall, K. Maeda, and L. D. Carr, Ann. Phys. **525**, 845–865 (2013).

[12] I. Kozyryev, Z. Lasner, and J. M. Doyle, Phys. Rev. A **103**, 043313 (2021).

[13] R. Bause, A. Christianen, A. Schindewolf, I. Bloch, and X.-Y. Luo, J. Phys. Chem. A **127**, 729–741 (2023).

[14] W. D. Phillips, Rev. Mod. Phys. **70**, 721–741 (1998).

[15] B. L. Augenbraun, L. Anderegg, C. Hallas, Z. D. Lasner, N. B. Vilas, and J. M. Doyle, Adv. At. Mol. Opt. Phys. **72**, 89–182 (2023).

[16] I. Kozyryev, L. Baum, K. Matsuda, B. L. Augenbraun, L. Anderegg, A. P. Sedlack, and J. M. Doyle, Phys. Rev. Lett. **118**, 173201 (2017).

[17] N. B. Vilas, C. Hallas, L. Anderegg, P. Robichaud, A. Winnicki, D. Mitra, and J. M. Doyle, Nature **606**, 70–74 (2022).

[18] H. J. Metcalf and P. van der Straten, *Laser Cooling and Trapping* (Springer Press, 1999).

[19] A. H. Myerson, D. J. Szwer, S. C. Webster, D. T. C. Allcock, M. J. Curtis, G. Imreh, J. A. Sherman, D. N. Stacey, A. M. Steane, and D. M. Lucas, Phys. Rev. Lett. **100**, 200502 (2008).

[20] R. Blatt and C. F. Roos, Nat. Phys. **8**, 277–284 (2012).

[21] S. Shuman, J. Barry, and D. DeMille, Nature **467**, 820–823 (2010).

[22] S. Truppe, H. J. Williams, M. Hambach, L. Caldwell, N. J. Fitch, E. A. Hinds, B. E. Sauer, and M. R. Tarbutt, Nat. Phys. **13**, 1173–1176 (2017).

[23] L. Anderegg, B. L. Augenbraun, Y. Bao, S. Burchesky, L. W. Cheuk, W. Ketterle, and J. M. Doyle, Nat. Phys. **14**, 890–893 (2018).

[24] Y. Wu, J. J. Burau, K. Mehling, J. Ye, and S. Ding, Phys. Rev. Lett. **127**, 263201 (2021).

[25] D. Mitra, N. B. Vilas, C. Hallas, L. Anderegg, B. L. Augenbraun, L. Baum, C. Miller, S. Raval, and J. M. Doyle, Science **369**, 1366–1369 (2020).

[26] B. Hemmerling, E. Chae, A. Ravi, L. Anderegg, G. K. Drayna, N. R. Hutzler, A. L. Collopy, J. Ye, W. Ketterle, and J. M. Doyle, J. Phys. B **49**, 174001 (2016).

[27] H. J. Williams, S. Truppe, M. Hambach, L. Caldwell, N. J. Fitch, E. A. Hinds, B. E. Sauer, and M. R. Tarbutt, New J. Phys. **19**, 113035 (2017).

[28] N. R. Hutzler, H.-I. Lu, and J. M. Doyle, Chem. Rev. **112**, 4803–4827 (2012).

[29] P. Aggarwal, Y. Yin, K. Esajas, H. L. Bethlem, A. Boeschoten, A. Borschevsky, S. Hoekstra, K. Jungmann, V. R. Marshall, T. B. Meijknecht, M. C. Mooij, R. G. E. Timmermans,

A. Touwen, W. Ubachs, and L. Willmann (NL−eEDM Collaboration), Phys. Rev. Lett. **127**, 173201 (2021).

[30] M. Zeppenfeld, B. G. U. Englert, R. Glöckner, A. Prehn, M. Mielenz, C. Sommer, L. D. van Buuren, M. Motsch, and G. Rempe, Nature **491**, 570–573 (2012).

[31] X. Wu, T. Gantner, M. Koller, M. Zeppenfeld, S. Chervenkov, and G. Rempe, Science **358**, 645–648 (2017).

[32] B. L. Augenbraun, A. Frenett, H. Sawaoka, C. Hallas, N. B. Vilas, A. Nasir, Z. D. Lasner, and J. M. Doyle, Phys. Rev. Lett. **127**, 263002 (2021).

[33] M. D. DiRosa, Eur. Phys. J. D **31**, 395–402 (2004).

[34] S. F. Vázquez-Carson, Q. Sun, J. Dai, D. Mitra, and T. Zelevinsky, New J. Phys. **24**, 083006 (2022).

[35] Y. Gao and T. Gao, Phys. Rev. A **90**, 052506 (2014).

[36] G. Herzberg, *Molecular Spectra and Molecular Structure, I. Spectra of Diatomic Molecules* (Springer Press, 1950).

[37] W. Demtröder, *Molecular Physics* (John Wiley & Sons, Ltd, 2005).

[38] J. von Neumann and E. Wigner, Phys. Z. **30**, 467 (1929).

[39] E. Teller, J. Phys. Chem. **41**, 109–116 (1937).

[40] C. A. Mead, J. Chem. Phys. **70**, 2276–2283 (1979).

[41] I. C. Lane, Phys. Rev. A **92**, 022511 (2015).

[42] P. K. H-J. Werner *et al.*, MOLPRO, version 2022.3, a package of *ab initio* programs, see https://www.molpro.net (2022).

[43] H.-J. Werner, P. J. Knowles, G. Knizia, F. R. Manby, and M. Schütz, Wiley Interdiscip. Rev. Comput. Mol. Sci. **2**, 242–253 (2012).

[44] H.-J. Werner, P. J. Knowles, F. R. Manby, J. A. Black, K. Doll, A. Heßelmann, D. Kats, A. Köhn, T. Korona, D. A. Kreplin, *et al.*, J. Chem. Phys. **152**, 144107 (2020).

[45] A. Shayesteh, S. F. Alavi, M. Rahman, and E. Gharib-Nezhad, Chem. Phys. Lett. **667**, 345–350 (2017).

[46] J. Koput and K. A. Peterson, J. Phys. Chem. A **106**, 9595–9599 (2002).

[47] T. H. Dunning Jr, J. Chem. Phys. **90**, 1007–1023 (1989).

[48] P. J. Knowles and H.-J. Werner, Chem. Phys. Lett. **115**, 259–267 (1985).

[49] H.-J. Werner and P. J. Knowles, J. Chem. Phys. **89**, 5803–5814 (1988).

[50] P. J. Knowles and H.-J. Werner, Theor. Chim. Acta **84**, 95–103 (1992).

[51] K. Shamasundar, G. Knizia, and H.-J. Werner, J. Chem. Phys. **135**, 054101 (2011).

[52] A. Berning, M. Schweizer, H.-J. Werner, P. J. Knowles, and P. Palmieri, Mol. Phys. **98**, 1823–1833 (2000).

[53] D. T. Colbert and W. H. Miller, J. Chem. Phys. **96**, 1982–1991 (1992).

[54] R. Baer, *Electron density functional theory* (Fritz Haber Center for Molecular Dynamics, 2016).

[55] T. Busch, A. D. Esposti, and H.-J. Werner, J. Chem. Phys. **94**, 6708–6715 (1991).

[56] D. Neuhauser and M. Baer, J. Chem. Phys. **91**, 4651–4657 (1989).

[57] D. Neuhauser, J. Chem. Phys. **93**, 7836–7842 (1990).

[58] D. Neuhauser, J. Chem. Phys. **103**, 8513–8527 (1995).

[59] D. Neuhasuer and M. Baer, J. Chem. Phys. **90**, 4351–4355 (1989).

[60] Q. Sun, C. E. Dickerson, J. Dai, I. M. Pope, L. Cheng, D. Neuhauser, A. N. Alexandrova, D. Mitra, and T. Zelevinsky, Phys. Rev. Res. **5**, 043070 (2023).

[61] B. Efron, Ann. Stat. **7**, 1–26 (1979).

[62] B. Efron and R. J. Tibshirani, *An Introduction to the Bootstrap*, Monographs on Statistics and Applied Probability No. 57 (Chapman & Hall/CRC, Boca Raton, Florida, USA, 1993).

[63] A. C. Davison and D. V. Hinkley, *Bootstrap Methods and their Application*, Cambridge Series in Statistical and Probabilistic Mathematics (Cambridge University Press, 1997).

[64] M. Ramanaiah and S. Lakshman, Physica C **113**, 263–270 (1982).

[65] A. Kawasaki, Phys. Rev. A **92**, 042507 (2015).

[66] B. H. McGuyer, M. McDonald, G. Z. Iwata, M. G. Tarallo, A. T. Grier, F. Apfelbeck, and T. Zelevinsky, New J. Phys. **17**, 055004 (2015).

[67] M. McDonald, B. H. McGuyer, F. Apfelbeck, C.-H. Lee, I. Majewska, R. Moszynski, and T. Zelevinsky, Nature **535**, 122–126 (2016).

[68] N. V. Vitanov, A. A. Rangelov, B. W. Shore, and K. Bergmann, Rev. Mod. Phys. **89**, 015006 (2017).

[69] S. A. Moses, J. P. Covey, M. T. Miecnikowski, D. S. Jin, and J. Ye, Nat. Phys. **13**, 13–20 (2017).

[70] A. Vardi, M. Shapiro, and K. Bergmann, Opt. Express **4**, 91–106 (1999).

[71] A. A. Rangelov, N. V. Vitanov, and E. Arimondo, Phys. Rev. A **76**, 043414 (2007).

[72] V. Barbé, A. Ciamei, B. Pasquiou, L. Reichsöllner, F. Schreck, P. S. Żuchowski, and J. M. Hutson, Nat. Phys. **14**, 881–884 (2018).

[73] A. Shayesteh, R. S. Ram, and P. F. Bernath, J. Mol. Spectrosc. **288**, 46–51 (2013).

[74] D. P. DiVincenzo, Fortschr. Phys. **48**, 771–783 (2000).

[75] D. J. Wineland, R. E. Drullinger, and F. L. Walls, Phys. Rev. Lett. **40**, 1639–1642 (1978).

[76] E. L. Raab, M. Prentiss, A. Cable, S. Chu, and D. E. Pritchard, Phys. Rev. Lett. **59**, 2631–2634 (1987).

[77] W. Happer, Rev. Mod. Phys. **44**, 169–249 (1972).

[78] D. J. Wineland, C. Monroe, W. M. Itano, D. Leibfried, B. E. King, and D. M. Meekhof, J. Res. Nat. Inst. Stand. Tech. **103**, 259–328 (1998).

[79] D. DeMille, Phys. Rev. Lett. **88**, 067901 (2002).

[80] S. F. Yelin, K. Kirby, and R. Côté, Phys. Rev. A **74**, 050301 (2006).

[81] F. Herrera, Y. Cao, S. Kais, and K. B. Whaley, New J. Phys. **16**, 075001 (2014).

[82] M. Karra, K. Sharma, B. Friedrich, S. Kais, and D. Herschbach, J. Chem. Phys. **144**, 094301 (2016).

[83] J. A. Blackmore, L. Caldwell, P. D. Gregory, E. M. Bridge, R. Sawant, J. Aldegunde, J. Mur-Petit, D. Jaksch, J. M. Hutson, B. E. Sauer, M. R. Tarbutt, and S. L. Cornish, Quantum Sci. Technol. **4**, 014010 (2019).

[84] K.-K. Ni, T. Rosenband, and D. D. Grimes, Chem. Sci. **9**, 6830–6838 (2018).

[85] E. R. Hudson and W. C. Campbell, Phys. Rev. A **98**, 040302 (2018).

[86] W. C. Campbell and E. R. Hudson, Phys. Rev. Lett. **125**, 120501 (2020).

[87] The ACME Collaboration: V. Andreev, D. G. Ang, D. DeMille, J. M. Doyle, G. Gabrielse, J. Haefner, N. R. Hutzler, Z. Lasner, C. Meisenhelder, B. R. O'Leary, C. D. Panda, A. D. West, E. P. West, and X. Wu, Nature **562**, 355 (2018).

[88] C. D. Panda1, C. Meisenhelder, M. Verma, D. G. Ang, J. Chow, Z. Lasner, X. Wu, D. DeMille, J. M. Doyle, and G. Gabrielse, J. Phys. B: At. Mol. Opt. Phys. **52**, 23500 (2019).

[89] E. S. Shuman, J. F. Barry, D. R. Glenn, and D. DeMille, Phys. Rev. Lett. **103**, 223001 (2009).

[90] M. T. Hummon, M. Yeo, B. K. Stuhl, A. L. Collopy, Y. Xia, and J. Ye, Phys. Rev. Lett. **110**, 143001 (2013).

[91] B. Augenbraun, Z. Lasner, A. Frenett, H. Sawaoka, C. Miller, T. Steimle, and J. Doyle, New J. Phys. **22**, 022003 (2020).

[92] I. Kozyryev, L. Baum, K. Matsuda, and J. M. Doyle, ChemPhysChem **17**, 3641–3648 (2016).

[93] J. Kłos and S. Kotochigova, Phys. Rev. Research **2**, 013384 (2020).

[94] M. V. Ivanov, F. H. Bangerter, P. Wójcik, and A. I. Krylov, J. Phys. Chem. Lett. **11**, 6670–6676 (2020).

[95] B. L. Augenbraun, J. M. Doyle, T. Zelevinsky, and I. Kozyryev, Phys. Rev. X **10** (2020).

[96] Y. Hao, L. F. Pašteka, L. Visscher, P. Aggarwal, *et al.*, J. Chem. Phys. **151**, 034302 (2019).

[97] S. Kang, F. Kuang, G. Jiang, and J. Du, Mol. Phys. **114**, 810–818 (2016).

[98] S. N. Tohme and M. Korek, J. Quant. Spectrosc. Radiat. Transf. **167**, 82 – 96 (2015).

[99] M. K. Nayak and R. K. Chaudhuri, J. Phys. B. **39**, 1231–1235 (2006).

[100] M. G. Kozlov, A. V. Titov, N. S. Mosyagin, and P. V. Souchko, Phys. Rev. A **56**, R3326–R3329 (1997).

[101] M. J. Frisch *et al.*, Gaussian16 Revision C.01 (2016), Gaussian Inc. Wallingford CT.

[102] F. Furche and R. Ahlrichs, J. Chem. Phys. **117**, 7433–7447 (2002).

[103] J. Liu and W. Liang, J. Chem. Phys. **135**, 014113 (2011).

[104] J. Liu and W. Liang, J. Chem. Phys. **135**, 184111 (2011).

[105] R. Bauernschmitt and R. Ahlrichs, Chem. Phys. Lett. **256**, 454–464 (1996).

[106] J. P. Perdew, M. Ernzerhof, and K. Burke, J. Chem. Phys. **105**, 9982–9985 (1996).

[107] S. Grimme, J. Anthony, S. Ehrlich, and H. Krieg, J. Chem. Phys. **132**, 154104 (2010).

[108] D. Rappoport and F. Furche, J. Chem. Phys. **133**, 134105–1–134105–11 (2010).

[109] S. Gozem and A. I. Krylov, WIREs Comput. Mol. Sci. **12**, e1546 (2022).

[110] C. E. Dickerson, H. Guo, A. J. Shin, B. L. Augenbraun, J. R. Caram, W. C. Campbell, and A. N. Alexandrova, Phys. Rev. Lett. **126**, 123002 (2021).

[111] E. T. Mengesha, A. T. Le, T. C. Steimle, L. Cheng, C. Zhang, B. L. Augenbraun, Z. Lasner, and J. Doyle, J. Phys. Chem. A. **124**, 3135–3148 (2020).

[112] L. Baum, N. B. Vilas, C. Hallas, B. L. Augenbraun, S. Raval, D. Mitra, and J. M. Doyle, Phys. Rev. A **103**, 043111 (2021).

[113] M. V. Ivanov, F. H. Bangerter, and A. I. Krylov, Phys. Chem. Chem. Phys. **21**, 19447 (2019).

[114] P. Hammett, Louis, J. Am. Chem. Soc. **59**, 96–103 (1937).

[115] C. Hansch, A. Leo, and R. W. Taft, Chem. Rev. **91**, 165–195 (1991).

[116] V. Campisciano, M. Gruttadauria, and F. Giacalone, ChemCatChem **11**, 90–133 (2019).

[117] Q. Wang and D. Astruc, Chem. Rev. **120**, 1438–1511 (2020).

[118] Y. Liu, X. Dong, and P. Chen, Chem. Soc. Rev. **41**, 2283–2307 (2012).

[119] K. Saha, S. S. Agasti, C. Kim, X. Li, and V. M. Rotello, Chem. Rev. **112**, 2739–2779 (2012).

[120] L. Guillemard, N. Kaplaneris, L. Ackermann, and M. J. Johansson, Nat. Rev. Chem. , 1–24 (2021).

[121] T. Cernak, K. D. Dykstra, S. Tyagarajan, P. Vachal, and S. W. Krska, Chem. Soc. Rev. **45**, 546–576 (2016).

[122] L. Anderegg, B. L. Augenbraun, E. Chae, B. Hemmerling, N. R. Hutzler, A. Ravi, A. Collopy, J. Ye, W. Ketterle, and J. M. Doyle, Phys. Rev. Lett. **119**, 103201 (2017).

[123] T. A. Isaev and R. Berger, Phys. Rev. Lett. **116**, 063006 (2016).

[124] C. E. Dickerson, H. Guo, G.-Z. Zhu, E. R. Hudson, J. R. Caram, W. C. Campbell, and A. N. Alexandrova, J. Phys. Chem. Lett. **12**, 3989–3995 (2021).

[125] G. Zhu, D. Mitra, B. Augenbraun, C. Dickerson, M. Frim, G. Lao, Z. Lasner, A. Alexandrova, W. Campbell, J. Caram, J. Doyle, and E. Hudson, Nat. Chem. **14**, 995–999 (2022).

[126] W. Domcke, L. Cederbaum, H. Köppel, and W. Von Niessen, Mol. Phys. **34**, 1759–1770 (1977).

[127] G. Fischer, *Vibronic Coupling: The Interaction between the Electronic and Nuclear Motions* (Academic Press, 1984).

[128] A. C. Paul, K. Sharma, M. A. Reza, H. Telfah, T. A. Miller, and J. Liu, J. Chem. Phys. **151**, 134303 (2019).

[129] P. J. Dagdigian, Annu. Rev. Phys. Chem. **48**, 95–123 (1997).

[130] Y. Mao, M. Head-Gordon, and Y. Shao, Chem. Sci. **9**, 8598–8607 (2018).

[131] J. Liu, J. Chem. Phys. **148**, 124112 (2018).

[132] N. R. Hutzler, Quantum Sci. Technol. **5**, 044011 (2020).

[133] I. C. Lane, Phys. Chem. Chem. Phys. **14**, 15078–15087 (2012).

[134] N. Balakrishnan, J. Chem. Phys. **145**, 150901 (2016).

[135] H. Guo, C. E. Dickerson, A. J. Shin, C. Zhao, T. L. Atallah, J. R. Caram, W. C. Campbell, and A. N. Alexandrova, Phys. Chem. Chem. Phys. **23**, 211–218 (2021).

[136] M. V. Ivanov, S. Gulania, and A. I. Krylov, J. Phys. Chem. Lett. **11**, 1297–1304 (2020).

[137] A. C. Paul, K. Sharma, H. Telfah, T. A. Miller, and J. Liu, J. Chem. Phys. **155**, 024301 (2021).

[138] H. Telfah, K. Sharma, A. C. Paul, S. S. Riyadh, T. A. Miller, and J. Liu, Phys. Chem. Chem. Phys. **24**, 8749–8762 (2022).

[139] C. E. Dickerson, C. Chang, H. Guo, and A. N. Alexandrova, J. Phys. Chem. A **126**, 9644–9650 (2022).

[140] P. Yu, A. Lopez, W. A. Goddard, and N. R. Hutzler, Phys. Chem. Chem. Phys. **25**, 154–170 (2023).

[141] H. Sinenka, Y. Bruyakin, A. Zaitsevskii, T. Isaev, and A. V. Bochenkova, J. Phys. Chem. Lett. **14**, 5784–5790 (2023).

[142] D. Mitra, Z. D. Lasner, G.-Z. Zhu, C. E. Dickerson, B. L. Augenbraun, A. D. Bailey, A. N. Alexandrova, W. C. Campbell, J. R. Caram, E. R. Hudson, and J. M. Doyle, J. Phys. Chem. Lett. **13**, 7029–7035 (2022).

[143] G. Lao, G.-Z. Zhu, C. E. Dickerson, B. L. Augenbraun, A. N. Alexandrova, J. R. Caram, E. R. Hudson, and W. C. Campbell, J. Phys. Chem. Lett. **13**, 11029–11035 (2022).

[144] P. B. Changala, N. Genossar-Dan, E. Brudner, T. Gur, J. H. Baraban, and M. C. McCarthy, Proc. Natl. Acad. Sci. U.S.A. **120**, e2303586120 (2023).

[145] T. Uzer and W. Miller, Phys. Rep. **199**, 73–146 (1991).

[146] D. J. Nesbitt and R. W. Field, J. Phys. Chem. **100**, 12735–12756 (1996).

[147] J. C. Keske and B. H. Pate, Annu. Rev. Phys. Chem. **51**, 323–353 (2000).

[148] D. McCarron, J. Phys. B: At. Mol. Opt. Phys. **51**, 212001 (2018).

[149] N. Fitch and M. Tarbutt, *Chapter Three - Laser-Cooled Molecules*, Vol. 70 (Academic Press, 2021) pp. 157–262.

[150] B. L. Augenbraun, S. Burchesky, A. Winnicki, and J. M. Doyle, J. Phys. Chem. Lett. **13**, 10771–10777 (2022).

[151] E. Fermi, Z. Phys. **71**, 250–259 (1931).

[152] H.-R. Dübal and M. Quack, J. Chem. Phys. **81**, 3779–3791 (1984).

[153] F. Weigend and R. Ahlrichs, Phys. Chem. Chem. Phys. **7**, 3297–3305 (2005).

[154] H. H. Nielsen, Rev. Mod. Phys. **23**, 90 (1951).

[155] V. Barone, J. Chem. Phys. **122**, 014108 (2005).

[156] M. A. Boyer and A. B. McCoy, Zenodo **5563091** (2021).

[157] M. A. Boyer and A. B. McCoy, J. Chem. Phys. **156**, 054107 (2022).

[158] M. A. Boyer and A. B. McCoy, J. Chem. Phys. **157**, 164113 (2022).

[159] S. J. Stropoli, T. Khuu, M. A. Boyer, N. V. Karimova, C. F. Gavin-Hanner, S. Mitra, A. L. Lachowicz, N. Yang, R. B. Gerber, A. B. McCoy, *et al.*, J. Chem. Phys. **156** (2022).

[160] J. A. Lau, M. DeWitt, M. A. Boyer, M. C. Babin, T. Solomis, M. Grellmann, K. R. Asmis, A. B. McCoy, and D. M. Neumark, J. Phys. Chem. A **127**, 3133–3147 (2023).

[161] G.-Z. Zhu, G. Lao, C. E. Dickerson, J. R. Caram, W. C. Campbell, A. N. Alexandrova, and E. R. Hudson, J. Phys. Chem. Lett. **15**, 590–597 (2024).

[162] C. Zhang, B. L. Augenbraun, Z. D. Lasner, N. B. Vilas, J. M. Doyle, and L. Cheng, J. Chem. Phys. **155**, 091101 (2021).

[163] C. Zhang, N. R. Hutzler, and L. Cheng, J. Chem. Theory Comput. **19**, 4136–4148 (2023).

[164] P. W. Atkins and R. S. Friedman, *Molecular Quantum Mechanics* (Oxford University Press, 2011).

[165] H. Lefebvre-Brion and R. W. Field, *The Spectra and Dynamics of Diatomic Molecules* (Elsevier, 2004).

[166] C. Brazier and P. Bernath, J. Mol. Spec. **114**, 163–173 (1985).

[167] C. Brazier, L. Ellingboe, S. Kinsey-Nielsen, and P. Bernath, J. Am. Chem. Soc. **108**, 2126–2132 (1986).

[168] J. Ortiz, J. Chem. Phys. **92**, 6728–6731 (1990).

[169] J. Ortiz, Chem. Phys. Lett. **169**, 116–120 (1990).

[170] R. Wormsbecher and R. Suenram, J. Mol. Spectrosc. **95**, 391–404 (1982).

[171] L. O'Brien, C. Brazier, and P. Bernath, J. Mol. Spectrosc. **130**, 33–45 (1988).

[172] P. Crozet, F. Martin, A. Ross, C. Linton, M. Dick, and A. Adam, J. Mol. Spectrosc. **213**, 28–34 (2002).

[173] D. Forthomme, C. Linton, A. Read, D. Tokaryk, A. Adam, L. Downie, A. Granger, and W. Hopkins, J. Mol. Spectrosc. **270**, 108–115 (2011).

[174] I. Kozyryev, T. C. Steimle, P. Yu, D.-T. Nguyen, and J. M. Doyle, New J. Phys. **21**, 052002 (2019).

[175] B. L. Augenbraun, Z. D. Lasner, A. Frenett, H. Sawaoka, A. T. Le, J. M. Doyle, and T. C. Steimle, Phys. Rev. A **103**, 022814 (2021).

[176] T. P. Snow and A. N. Witt, Science **270**, 1455–1460 (1995).

[177] A. Tielens, Annu. Rev. Astron. Astrophys. **46**, 289–337 (2008).

[178] E. Hardegree-Ullman, M. Gudipati, A. Boogert, H. Lignell, L. J. Allamandola, K. R. Stapelfeldt, and M. Werner, Astrophys. J. **784**, 172 (2014).

[179] M. Hanine, Z. Meng, S. Lu, P. Xie, S. Picaud, M. Devel, and Z. Wang, Astrophys. J. **900**, 188 (2020).

[180] E. T. Young, E. E. Becklin, and P. M. M. *et. al.*, Astrophys. J. Lett. **749**, L17 (2012).

[181] C. W. Bauschlicher, C. Boersma, A. Ricca, A. L. Mattioda, J. Cami, E. Peeters, F. S. de Armas, G. P. Saborido, D. M. Hudgins, and L. J. Allamandola, Astrophys. J. Suppl. **189**, 341–351 (2010).

[182] G. Malloci, C. Joblin, and G. Mulas, Chem. Phys. **332**, 353 – 359 (2007).

[183] E. Cané, A. Miani, and A. Trombetti, J. Phys. Chem. A **111**, 8218–8222 (2007).

[184] C. J. Mackie, A. Candian, X. Huang, E. Maltseva, A. Petrignani, J. Oomens, W. J. Buma, T. J. Lee, and A. G. G. M. Tielens, J. Chem. Phys. **143**, 224314 (2015).

[185] G. Kresse and J. Furthmüller, Phys. Rev. B **54**, 11169–11186 (1996).

[186] G. Kresse and J. Furthmüller, Comput. Mater. Sci. **6**, 15 – 50 (1996).

[187] G. Kresse and J. Hafner, Phys. Rev. B **49**, 14251–14269 (1994).

[188] G. Kresse and J. Hafner, Phys. Rev. B **47**, 558–561 (1993).

[189] J. P. Perdew, K. Burke, and M. Ernzerhof, Phys. Rev. Lett. **78**, 1396–1396 (1997).

[190] A. V. Krukau, O. A. Vydrov, A. F. Izmaylov, and G. E. Scuseria, J. Chem. Phys. **125**, 224106 (2006).

[191] W. Tang, E. Sanville, and G. Henkelman, J. Phys. Condens. Matter **21**, 084204 (2009).

[192] G. Henkelman, A. Arnaldsson, and H. Jónsson, Comput. Mater. Sci. **36**, 354 – 360 (2006).

[193] P. Borlido, T. Aull, A. Huran, F. Tran, M. A. L. Marques, and S. Botti, J. Chem. Theory Comput. **15**, 5069–5079 (2019).

[194] G. Kresse and D. Joubert, Phys. Rev. B **59**, 1758–1775 (1999).

[195] P. E. Blöchl, Phys. Rev. B **50**, 17953–17979 (1994).

[196] I. Berlman, *Handbook of Fluorescence Spectra of Aromatic Molecules* (Academic Press, 1971).

[197] K. C. Smyth, J. A. Schiavone, and R. S. Freund, J. Chem. Phys. **62**, 136–144 (1975).

[198] J. Novak and M. Windsor, J. Chem. Phys. **47**, 3075–3076 (1967).

[199] A. M. Ellis, Int. Rev. Phys. Chem. **20**, 551–590 (2001).

[200] J. Piskorski, D. Patterson, S. Eibenberger, and J. M. Doyle, ChemPhysChem **15**, 3800–3804 (2014).

[201] D. Patterson, E. Tsikata, and J. M. Doyle, Phys. Chem. Chem. Phys. **12**, 9736–9741 (2010).

[202] H. Bernien, S. Schwartz, A. Keesling, H. Levine, A. Omran, H. Pichler, S. Choi, A. S. Zibrov, M. Endres, M. Greiner, *et al.*, Nature **551**, 579–584 (2017).

[203] C. Monroe, W. C. Campbell, L.-M. Duan, Z.-X. Gong, A. V. Gorshkov, P. Hess, R. Islam, K. Kim, N. M. Linke, G. Pagano, *et al.*, Rev. Mod. Phys. **93**, 025001 (2021).

[204] M. Morgado and S. Whitlock, AVS Quantum Sci. **3**, 023501 (2021).

[205] C. S. Chiu, G. Ji, A. Bohrdt, M. Xu, M. Knap, E. Demler, F. Grusdt, M. Greiner, and D. Greif, Science **365**, 251–256 (2019).

[206] G. Semeghini, H. Levine, A. Keesling, S. Ebadi, T. T. Wang, D. Bluvstein, R. Verresen, H. Pichler, M. Kalinowski, R. Samajdar, *et al.*, Science **374**, 1242–1247 (2021).

[207] N. Grzesiak, R. Blümel, K. Wright, K. M. Beck, N. C. Pisenti, M. Li, V. Chaplin, J. M. Amini, S. Debnath, J.-S. Chen, *et al.*, Nat. Commun. **11**, 1–6 (2020).

[208] Y. Liu, M.-G. Hu, M. A. Nichols, D. Yang, D. Xie, H. Guo, and K.-K. Ni, Nature **593**, 379–384 (2021).

[209] B. R. Heazlewood and T. P. Softley, Nat. Rev. Chem. **5**, 125–140 (2021).

[210] F. Pianalto, A. Bopegedera, W. Fernando, R. Hailey, L. O'Brien, C. Brazier, P. Keller, and P. Bernath, J. Am. Chem. Soc. **112**, 7900–7903 (1990).

[211] J. Ortiz, J. Am. Chem. Soc. **113**, 1102–1108 (1991).

[212] J. Ortiz, J. Am. Chem. Soc. **113**, 3593–3595 (1991).

[213] P. Yu, A. Lopez, W. A. Goddard, and N. R. Hutzler, Phys. Chem. Chem. Phys. **25**, 154–170 (2023).

[214] D. Mitra and Z. L. et. al., J. Phys. Chem. Lett. **13**, 7029–7035 (2022).

[215] A. C. Paul, M. A. Reza, and J. Liu, J. Mol. Spec. **330**, 142–146 (2016).

[216] P. Krantz, M. Kjaergaard, F. Yan, T. P. Orlando, S. Gustavsson, and W. D. Oliver, Appl. Phys. Rev. **6** (2019).

[217] C. D. Bruzewicz, J. Chiaverini, R. McConnell, and J. M. Sage, Appl. Phys. Rev. **6** (2019).

[218] Y. Shao, Y. Mei, D. Sundholm, and V. R. I. Kaila, J. Chem. Theory Comput. **16**, 587–600 (2020).

[219] P. J. Robinson, X. Zhang, T. McQueen, K. H. Bowen, and A. N. Alexandrova, J. Chem. Phys. A **121**, 1849–1854 (2017).

[220] C. Adamo and V. Barone, J. Chem. Phys. **110**, 6158–6170 (1999).

[221] P. Borlido, J. Schmidt, A. W. Huran, F. Tran, M. A. Marques, and S. Botti, npj Comput. Mater. **6**, 96 (2020).

[222] P. Borlido, T. Aull, A. W. Huran, F. Tran, M. A. L. Marques, and S. Botti, J. Chem. Theory Comput. **15**, 5069–5079 (2019).

[223] R. Naaman and Z. Vager, *The structure of small molecules and ions* (Springer Science & Business Media, 1988).

[224] H. Notsu, I. Yagi, T. Tatsuma, D. A. Tryk, and A. Fujishima, Electrochem. Solid-State Lett. **2**, 522 (1999).

[225] H. Kawarada, Surf. Sci. Rep. **26**, 205–259 (1996).

[226] A. Bopegedera, C. Brazier, and P. Bernath, J. Phys. Chem. **91**, 2779–2781 (1987).

[227] A. C. Aragones, N. L. Haworth, N. Darwish, S. Ciampi, N. J. Bloomfield, G. G. Wallace, I. Diez-Perez, and M. L. Coote, Nature **531**, 88–91 (2016).

[228] D. Jaksch, J. I. Cirac, P. Zoller, S. L. Rolston, R. Côté, and M. D. Lukin, Phys. Rev. Lett. **85**, 2208–2211 (2000).

[229] L. D. Augustovičová and J. L. Bohn, New J. Phys. **21**, 103022 (2019).

[230] K.-K. Ni, S. Ospelkaus, M. De Miranda, A. Pe'Er, B. Neyenhuis, J. Zirbel, S. Kotochigova, P. Julienne, D. Jin, and J. Ye, Science **322**, 231–235 (2008).

[231] S. Ding, Y. Wu, I. A. Finneran, J. J. Burau, and J. Ye, Phys. Rev. X **10**, 021049 (2020).

[232] S. Hofsäss, M. Doppelbauer, S. Wright, S. Kray, B. Sartakov, J. Pérez-Ríos, G. Meijer, and S. Truppe, New J. Phys. **23**, 075001 (2021).

[233] Y. Zhang, Z. Zeng, Q. Liang, W. Bu, and B. Yan, Phys. Rev. A **105**, 033307 (2022).

[234] R. H. Dicke, Phys. Rev. **93**, 99–110 (1954).

[235] M. Gross and S. Haroche, Phys. Rep. **93**, 301–396 (1982).

[236] A. A. Svidzinsky, J. T. Chang, and M. O. Scully, Phys. Rev. Lett. **100**, 160504 (2008).

[237] B. M. Garraway, Phil. Trans. R. Soc. A. **369**, 1137—-1155 (2011).

[238] J. P. Philbin and P. Narang, PRX Quantum **2**, 030102 (2021).

[239] J. P. Philbin, J. Kelly, L. Peng, I. Coropceanu, A. Hazarika, D. V. Talapin, E. Rabani, X. Ma, and P. Narang, arxiv:2104.06452 (2021).

[240] N. J. Hestand and F. C. Spano, Chem. Rev. **118**, 7069–7163 (2018).

[241] M. Marques and E. Gross, Annu. Rev. Phys. Chem. **55**, 427–455 (2004).

[242] J. F. Stanton and R. J. Bartlett, J. Chem. Phys. **98**, 7029–7039 (1993).

[243] K. Andersson, P. Malmqvist, and B. O. Roos, J. Chem. Phys. **96**, 1218–1226 (1992).

[244] C. E. Dickerson, A. N. Alexandrova, P. Narang, and J. P. Philbin, arXiv:2310.01534 (2023).

[245] R. Prevedel, G. Cronenberg, M. S. Tame, M. Paternostro, P. Walther, M.-S. Kim, and A. Zeilinger, Phys. Rev. Lett. **103**, 020503 (2009).

[246] W. Wieczorek, R. Krischek, N. Kiesel, P. Michelberger, G. Tóth, and H. Weinfurter, Phys. Rev. Lett. **103**, 020504 (2009).

[247] S. Hadfield, Z. Wang, B. O'gorman, E. G. Rieffel, D. Venturelli, and R. Biswas, Algorithms **12**, 34 (2019).

[248] T.-X. Zheng, A. Li, J. Rosen, S. Zhou, M. Koppenhöfer, Z. Ma, F. T. Chong, A. A. Clerk, L. Jiang, and P. C. Maurer, npj Quantum Inf. **8**, 150 (2022).

[249] W. Tremel and R. Hoffmann, J. Am. Chem. Soc. **109**, 124–140 (1987).

[250] J. Park, G. Lee, F. Wolff-Fabris, Y. Koh, M. Eom, Y. K. Kim, M. Farhan, Y. Jo, C. Kim, J. Shim, *et al.*, Phys. Rev. Lett. **107**, 126402 (2011).

[251] S. M. Young and C. L. Kane, Phys. Rev. Lett. **115**, 126803 (2015).

[252] S. M. Teicher, J. F. Linnartz, R. Singha, D. Pizzirani, S. Klemenz, S. Wiedmann, J. Cano, and L. M. Schoop, Chem. Mater. **34**, 4446–4455 (2022).

[253] D. Budker and M. Romalis, Nat. Phys. **3**, 227–234 (2007).

[254] V. Shah, S. Knappe, P. D. Schwindt, and J. Kitching, Nat. Photonics **1**, 649–652 (2007).

[255] C. L. Degen, F. Reinhard, and P. Cappellaro, Rev. Mod. Phys. **89**, 035002 (2017).

[256] I. Kominis, T. Kornack, J. Allred, and M. V. Romalis, Nature **422**, 596–599 (2003).

[257] J. Kitching, S. Knappe, and E. A. Donley, IEEE Sens. J. **11**, 1749–1758 (2011).

[258] I. M. Savukov and M. V. Romalis, Phys. Rev. Lett. **94**, 123001 (2005).

[259] J. C. Allred, R. N. Lyman, T. W. Kornack, and M. V. Romalis, Phys. Rev. Lett. **89**, 130801 (2002).

[260] D. Budker, D. F. Kimball, S. M. Rochester, V. V. Yashchuk, and M. Zolotorev, Phys. Rev. A **62**, 043403 (2000).

[261] S. J. Seltzer and M. V. Romalis, App. Phys. Lett. **85**, 4804–4806 (2004).

[262] J. Kitching, Appl. Phys. Rev. **5** (2018).

[263] D. Parker, E. A. Suturina, I. Kuprov, and N. F. Chilton, Acc. Chem. Res. **53**, 1520–1534 (2020).

[264] G. Buono-Core, H. Li, and B. Marciniak, Coord. Chem. Rev. **99**, 55–87 (1990).

[265] B. M. Walsh, in *Advances in Spectroscopy for Lasers and Sensing* (Springer Netherlands, 2006) pp. 403–433.

[266] J. An, C. M. Shade, D. A. Chengelis-Czegan, S. Petoud, and N. L. Rosi, J. Am. Chem. Soc. **133**, 1220–1223 (2011).

[267] L. Di Bari, G. Pintacuda, and P. Salvadori, J. Am. Chem. Soc. **122**, 5557–5562 (2000).

[268] H. Wang, P. L. Gould, and W. C. Stwalley, Phys. Rev. A **53**, R1216–R1219 (1996).

[269] A. O. Sushkov and D. Budker, Phys. Rev. A **77**, 042707 (2008).

[270] H. Schempp, G. Günter, M. Robert-de Saint-Vincent, C. S. Hofmann, D. Breyel, A. Komnik, D. W. Schönleber, M. Gärttner, J. Evers, S. Whitlock, and M. Weidemüller, Phys. Rev. Lett. **112**, 013002 (2014).

[271] N. Malossi, M. M. Valado, S. Scotto, P. Huillery, P. Pillet, D. Ciampini, E. Arimondo, and O. Morsch, Phys. Rev. Lett. **113**, 023006 (2014).

[272] TURBOMOLE V7.2 2017, a development of University of Karlsruhe and Forschungszentrum Karlsruhe GmbH, 1989-2007, TURBOMOLE GmbH, since 2007; available from http://www.turbomole.com.

[273] V. N. Staroverov, G. E. Scuseria, J. Tao, and J. P. Perdew, J. Chem. Phys. **119**, 12129–12137 (2003).

[274] J. Tao, J. P. Perdew, V. N. Staroverov, and G. E. Scuseria, Phys. Rev. Lett. **91**, 146401 (2003).

[275] P.-O. Widmark, P.-Å. Malmqvist, and B. O. Roos, Theor. Chim. Acta **77**, 291–306 (1990).

[276] B. O. Roos, R. Lindh, P.- Malmqvist, V. Veryazov, P.-O. Widmark, and A. C. Borin, J. Phys. Chem. A **112**, 11431–11435 (2008).

[277] A. Schäfer, A. Klamt, D. Sattel, J. C. W. Lohrenz, and F. Eckert, Phys. Chem. Chem. Phys. **2**, 2187–2193 (2000).

[278] I. F. Galván and R. L. et. al., J. Chem. Theory Comput. **15**, 5925–5964 (2019).

[279] B. O. Roos, P. R. Taylor, and P. E. Sigbahn, Chem. Phys. **48**, 157–173 (1980).

[280] P. E. M. Siegbahn, J. Almlöf, A. Heiberg, and B. O. Roos, J. Chem. Phys. **74**, 2384–2396 (1981).

[281] K. Andersson, Theor. Chim. Acta **91**, 31–46 (1995).

[282] K. Andersson, P. A. Malmqvist, B. O. Roos, A. J. Sadlej, and K. Wolinski, J. Phys. Chem. **94**, 5483–5488 (1990).

[283] J. Finley, P. Åke Malmqvist, B. O. Roos, and L. Serrano-Andrés, Chem. Phys. Lett. **288**, 299–306 (1998).

[284] M. Douglas and N. M. Kroll, Ann. Phys. **82**, 89–155 (1974).

[285] B. A. Hess, Phys. Rev. A **33**, 3742–3748 (1986).

[286] G. Jansen and B. A. Hess, Phys. Rev. A **39**, 6016–6017 (1989).

[287] A. J. Shin, C. Zhao, Y. Shen, C. E. Dickerson, B. Li, D. Bím, T. L. Atallah, P. H. Oyala, L. K. Alson, A. N. Alexandrova, *et al.*, chemrxiv-2022-vg4jr (2022).

[288] P. Åke Malmqvist, B. O. Roos, and B. Schimmelpfennig, Chem. Phys. Lett. **357**, 230–240 (2002).

[289] P. Åke Malmqvist and B. O. Roos, Chem. Phys. Lett. **155**, 189–194 (1989).

[290] S. Vancoillie, P.- Malmqvist, and K. Pierloot, ChemPhysChem **8**, 1803–1815 (2007).

[291] W. Chmaisani, N. El-Kork, S. Elmoussaoui, and M. Korek, ACS Omega **4**, 14987–14995 (2019).

[292] H. Hu, A. J. Jenkins, H. Liu, J. M. Kasper, M. J. Frisch, and X. Li, J. Chem. Theory Comput. **16**, 2975–2984 (2020).

[293] D. F. Evans, J. Chem. Soc. , 2003–2005 (1959).

[294] A. Dey, P. Kalita, and V. Chandrasekhar, ACS Omega **3**, 9462–9475 (2018).

[295] B. M. Flanagan, P. V. Bernhardt, E. R. Krausz, S. R. Lüthi, and M. J. Riley, Inorg. Chem. **41**, 5024–5033 (2002).

[296] W. C. Martin, R. Zalubas, and L. Hagan, National Bureau of Standards (1978).

[297] T. L. Atallah, A. V. Sica, A. J. Shin, H. C. Friedman, Y. K. Kahrobai, and J. R. Caram, J. Phys. Chem. A **123**, 6792–6798 (2019).

[298] R.-R. Tan, X. Shen, L. Hu, and F.-S. Zhang, Chin. Phys. B **21**, 086402 (2012).

[299] Y. Ning, J. Tang, Y.-W. Liu, J. Jing, Y. Sun, and J.-L. Zhang, Chem. Sci. **9**, 3742–3753 (2018).

[300] N. M. Shavaleev, R. Scopelliti, F. Gumy, and J.-C. G. Bünzli, Inorg. Chem. **48**, 7937–7946 (2009).

[301] O. E. Mor, T. Ohana, A. Borne, Y. Diskin-Posner, M. Asher, O. Yaffe, A. Shanzer, and B. Dayan, ACS Photonics **9**, 2676–2682 (2022).

[302] M. Atzori, K. Dhbaibi, H. Douib, M. Grasser, V. Dorcet, I. Breslavetz, K. Paillot, O. Cador, G. L. J. A. Rikken, B. Le Guennic, J. Crassous, F. Pointillart, and C. Train, J. Am. Chem. Soc. **143**, 2671–2675 (2021).

[303] K. S. Pedersen, J. Dreiser, H. Weihe, R. Sibille, H. V. Johannesen, M. A. Sørensen, B. E. Nielsen, M. Sigrist, H. Mutka, S. Rols, J. Bendix, and S. Piligkos, Inorg. Chem. **54**, 7600–7606 (2015).

[304] A. Kirmiz, D. Saiki, and M. Augustine, Spectrochim. Acta A **75**, 1211–1217 (2010).

[305] A. Gorczyński, D. Marcinkowski, M. Kubicki, M. Löffler, M. Korabik, M. Karbowiak, P. Wiśniewski, C. Rudowicz, and V. Patroniak, Inorg. Chem. Front. **5**, 605–618 (2018).

[306] P. Petit, J. Petit, P. Goldner, and B. Viana, Opt. Mater. **30**, 1093–1097 (2008).

[307] J. Wen, M. F. Reid, L. Ning, J. Zhang, Y. Zhang, C.-K. Duan, and M. Yin, J. Lumin. **152**, 54–57 (2014), 18th International Conference on Dynamical Processes in Excited States of Solids.

[308] J. Wen, L. Ning, Y. Huang, S. Zhan, J. Zhang, C.-K. Duan, and M. Yin, Mater. Res. Express **2**, 086202 (2015).

[309] Z. Barandiarán and L. Seijo, Theor. Chem. Acc. **116**, 505–508 (2006).

[310] P. J. Stephens, J. Chem. Phys. **52**, 3489–3516 (1970).

[311] T. D. Dunbar, W. L. Warren, B. A. Tuttle, C. A. Randall, and Y. Tsur, J. Phys. Chem. B **108**, 908–917 (2004).

[312] P. Appel, *Scanning nanomagnetometry: Probing magnetism with single spins in diamond*, Ph.D. thesis, University of Basel (2017).

[313] P. D. D. Schwindt, S. Knappe, V. Shah, L. Hollberg, J. Kitching, L.-A. Liew, and J. Moreland, Appl. Phys. Lett. **85**, 6409–6411 (2004).

[314] F. Casola, T. Van Der Sar, and A. Yacoby, Nat. Rev. Mat. **3**, 1–13 (2018).

[315] C. Degen, Nat. Nannotechnol. **3**, 643–644 (2008).

[316] S. J. Seltzer, P. J. Meares, and M. V. Romalis, Phys. Rev. A **75**, 051407 (2007).

[317] S. Li, P. Dai, J. Liu, Z. Xu, and K. Chida, Opt. Mater. Express **12**, 4384–4398 (2022).

[318] N. Aslam, H. Zhou, E. K. Urbach, M. J. Turner, R. L. Walsworth, M. D. Lukin, and H. Park, Nat. Rev. Phys. **5**, 157–169 (2023).